8-2021

Durability and Damage Analysis of Hybrid Multiscale Composites

Suma Ayyagari

DURABILITY AND DAMAGE ANALYSIS OF HYBRID MULTISCALE COMPOSITES

By

Suma Ayyagari

A Dissertation Submitted to the Faculty of Embry-Riddle Aeronautical University in Partial Fulfillment of the Requirements for the Degree of Doctor of Philosophy in Aerospace Engineering

August 2021
Embry-Riddle Aeronautical University
Daytona Beach, Florida

DURABILITY AND DAMAGE ANALYSIS OF HYBRID MULTISCALE COMPOSITES

By

Suma Ayyagari

This Dissertation was prepared under the direction of the candidate's Dissertation Committee Chair, Dr. Marwan Al-Haik, Department of Aerospace Engineering, and has been approved by the members of the Dissertation Committee. It was submitted to the Office of the Senior Vice President for Academic Affairs and Provost, and was accepted in the partial fulfillment of the requirements for the Degree of Philosophy in Aerospace Engineering.

DISSERTATION COMMITTEE

Marwan Al-Haik
Digitally signed by Marwan Al-Haik
DN: cn=Marwan Al-Haik, o=Embry-Riddle Aeronautical University, ou=Aerospace Engineering, email=alhaikm@erau.edu, c=US
Date: 2021.08.04 22:35:01 -04'00'

Chairman, Dr. Marwan Al-Haik

Sirish Namilae
Digitally signed by Sirish Namilae
Date: 2021.08.06 06:32:54 -04'00'

Member, Dr. Sirish Namilae

Anastasios Lyrintzis
Digitally signed by Anastasios Lyrintzis
Date: 2021.08.06 08:02:25 -04'00'

Member, Dr. Ali Yeilaghi Tamijani

Daewon Kim
Digitally signed by Daewon Kim
Date: 2021.08.05 10:58:09 -04'00'

Member, Dr. Daewon Kim

Fady Barsoum
Digitally signed by Fady Barsoum
Date: 2021.08.05 19:01:20 -04'00'

Member, Dr. Fady F. Barsoum

Sirish Namilae
Digitally signed by Sirish Namilae
Date: 2021.08.06 06:33:11 -04'00'

Graduate Program Coordinator,
Dr. Sirish Namilae

08/06/2021

Date

Maj Mirmirani
Digitally signed by Maj Mirmirani
Date: 2021.08.06 11:19:12 -04'00'

Dean of the College of Engineering, Dr. Maj Mirmirani

Date

Lon Moeller
Digitally signed by Lon Moeller
Date: 2021.08.06 13:01:38 -04'00'

Senior Vice President for
Academic Affairs and Provost
Lon Moeller, J.D.

Date

ACKNOWLEDGEMENTS

I would like to express my deepest appreciation to my committee chair, Dr. Marwan Al-Haik, who guided me along in this adventurous journey. The long discussions and arguments on varied topics of science forced me to ask the right questions and look deeper into finding a feasible solution to any issue at hand. He gave me the freedom to fail. And when I did fail, he guided me to find the right path. Hence, it was through him that I could expand the horizons of my knowledge. For this reason, his immense patience levels, and his resolute composure, I am forever indebted to him. As a counselor, and a partner in research, he has been my true North for the last several years and for that I am profoundly grateful.

I thank my committee members, Dr. Dae Won Kim, Dr. Sirish Namilae, Dr. Ali Yeilaghi Tamijani, and Dr. Fady F. Barsoum for their support and patience in reviewing my work.

I would like to express my gratitude to my family for their enduring love towards me. I cannot thank my parents; sisters, Devi, Maanasi, and Yashika; and my fiancé, Raghu; enough for their patience during testing times.

Although I cannot name all my friends here, I would specially like to thank Rossana Fernandes, Dr. Audrey Gbaguidi, Dr. Boutros Azizi, Yogesh Pai, Samprada Shrestha, and Tasneem Rashid for their continuous support through my doctorate program. Finally, I would like to thank Dr. Pamela L. Daniels for her help in formatting this dissertation.

ABSTRACT

In this dissertation, an effort was carried out to enhance the mechanical performance of fiber reinforced composites (FRPs) by modification of the fibers' surface morphologies. The effects of various surface alterations of a plain-woven carbon fiber fabric surface, on the fiber/epoxy interface were investigated. The alterations were mostly achieved by growing different nanofillers like zinc oxide nanorods (ZnO NR), carbon nanotubes (CNTs), and metal organic frameworks (MOFs) on the fiber surface. While the growth techniques for ZnO NR and CNTs place restrictions on the size of the fabricated composites, MOFs route is uniform, affordable, and can be readily scaled up to any required size. This makes this method more feasible and versatile than any other nanofillers. This dissertation comprises three major investigations: Study of hybrid composites with zinc oxide nanorods based surface modifications; Study of hybrid composites with carbon nanotubes-based surface modifications; and Study of hybrid composites with metal organic framework-based surface modifications.

The growth of zinc oxide nanorods on carbon fiber surface was performed with a combination of physical vapor deposition (PVD) and hydrothermal growth techniques. Various configurations of composites were fabricated to study the effects of altering the topology of the nanorods and functionalizing the fiber surface with polydopamine. Mechanical analysis showed a significant improvement in strength and stiffness in samples with patterning, when compared to samples with uniform nanofiller growth. Damping results show that polydopamine improved the adhesion between the carbon fiber and zinc oxide nanofillers, thus increasing the glass

transition temperature of the composites. A molecular dynamics (MD) model was built to study this phenomenon in an atomic scale. The results showed a significant improvement in Young's, bulk, and shear moduli as a consequence of the addition of zinc oxide nanorods.

Various topologies of CNTs were synthesized using physical vapor deposition and graphitic structures by design (GSD) techniques on the carbon fiber surface. Mechanical characterization of these hybrid composites was performed via tensile testing, dynamic mechanical analysis (DMA), and fracture analysis. A study of viscoplastic behavior of these composites using stress relaxation and creep tests was also performed for these different composites' configurations. A phenomenological viscoplastic model was utilized for creep prediction over long periods of time utilizing shorter stress relaxation tests. The results showed that with proper geometrical patterning of CNTs, significant improvements in strength, stiffness, creep and relaxation resistance, and glass transition temperatures can be realized.

A comprehensive study on fracture analysis depicting delamination was performed using crack propagation experiments and ANSYS simulations for composites based on CNTs/carbon fibers hybrid reinforcements. ANSYS simulations employed both cohesive zone modeling (CZM) and virtual crack closure (VCCT) technique to model interlaminar delamination. The results in all the three setups showed that coarser patterns of carbon nanotubes on the carbon fiber surface perform better in resisting crack propagation due to more efficient energy dissipation mechanisms at the fiber/matrix interface.

Finally, an investigation on multiscale hybrid composites with nickel-based MOFs as

an interface was conducted. Growing MOFs require both de-sizing and acid etching of the fibers. Acid activation made the carbon fiber surface chemically active, furnishing better adherence between the MOFs and the carbon fibers. These MOFs were also utilized as a catalyst to grow carbon nanotubes on the carbon fiber surface; hence, replacing the unscalable PVD. The hybrid composites based on MOFs as reinforcements at the fiber/matrix interface exhibited improvements in tensile and shear strength and enhanced the damping parameters for the composite.

In summary, all the investigations in this dissertation conclude that tailoring carbon fiber surface using various nanofillers, and functionalization play a crucial role in shaping the interlaminar strength of carbon fiber polymer composites among other mechanical enhancements.

TABLE OF CONTENTS

LIST OF FIGURES

Figure Page

Figure Page

Figure Page

Figure Page

Figure Page

Figure Page

Figure Page

Figure Page

Figure Page

Figure Page

LIST OF TABLES

NOMENCLATURE

FRPs	Fiber reinforced composites
CF	Carbon Fiber
CFRPs	Carbon fiber reinforced composites
ZnO NR	Zinc oxide nanorods
CNTs	Carbon nanotubes
MWCNTs	Multiwalled carbon nanotubes
SWCNTs	Single-walled carbon nanotubes
MOFs	Metal organic frameworks
GNPs	Graphite nanoplatelets
NDs	Nanodiamonds
CNFs	Carbon nanofibers
PDA	Polydopamine
PVD	Physical vapor deposition
CVD	Chemical vapor deposition
GSD	Graphitic structures by design
MD	Molecular dynamics
LAMMPS	Large-scale Atomic/Molecular Parallel Simulator

DMA	Dynamic mechanical analysis
CZM	Cohesive zone modeling
VCCT	Virtual crack closure technique
CO_2	Carbon dioxide
HMTA	Hexamethylenetetramine
TETA	Triethylenetetramine
DETA	Diethylenetriamine
NaOH	Sodium hydroxide
HCl	Hydrochloric acid
CHP	1-Cyclohexyl-2-pyrrolidone
RF	Radio frequency
NMR	Nuclear magnetic resonance
PP	Polypropylene
DCB	Double cantilever beam
ERR	Energy release rate
LEFM	Linear elastic fracture mechanics
PDA_B	Functionalized with polydopamine before
PDA_A	Functionalized with polydopamine after

PDA_BA	Functionalized with polydopamine before and after
PAN	Polyacrylonitrile
DI	De-ionized
cPs	Centipoise
psi	Pounds per square inch
ASTM	American Society for Testing and Materials
SEM	Scanning Electron Microscopy
MTS	Material Testing System
DHR	Discovery hybrid rheometer
DMA	Dynamic mechanical analysis
T_g	Glass transition temperature
N	Total number of atoms in the system
NVT	Constant number of atoms, volume, and temperature
G_{IC}	Critical strain energy release rate
PTFE	Polytetrafluoroethylene
DIC	Digital image correlation
DM	Design modeler
DAQ	Data acquisition

COOH	Carboxylic acid
EDS	Energy dispersive X-ray spectroscopy

1. Introduction

Since the 1950s, the usage of composite materials in the aerospace industry steadily increased, progressing from glass fiber to carbon fiber as reinforcements in a polymer matrix (Rajak et al., 2019). There are multiple reasons for this trend. The significant one among them is the high specific strength and stiffness of these materials. Currently, composites contribute to around 35-50% of the entire airplane structure including B787 and AB380 (Giurgiutiu, 2016). This trend carries over to other structural applications, including civil infrastructure, automotive industry, ships, sporting goods, and the healthcare.

The ever-growing usage and research of carbon fiber reinforced polymer composites (CFRPs) have revealed several of their shortcomings. These include interlaminar delamination due to insufficient out of plane mechanical properties, complex manufacturing, and rigorous repair techniques, to name a few. From the research point of view, all future space endeavors require better materials, which are strong, light, delamination resistant, and multifunctional. This quest led to the emergence of the field of composites with multiscale reinforcements; hybrid composite materials.

1.1. Hybrid Composites

Traditionally, composites constitute two or more macroscopically visible materials, which are combined to create a new material with a set of properties that are different from those of the individual constituents. If these constituents are multiscale, these materials are called hybrid composite materials. Hybrid composites can be attained by modifying the fiber or modifying the matrix. As a

simple illustration of this concept, carbon nanotubes (CNTs) can be grown on carbon fiber directly, as can be seen in Figure 1.1. Alternatively, CNTs can be blended with the resin matrix before the fabrication process, as shown in Figure 1.2. The properties of the resulting composite are highly dependent on the homogeneity of all the micro and macro constituents involved.

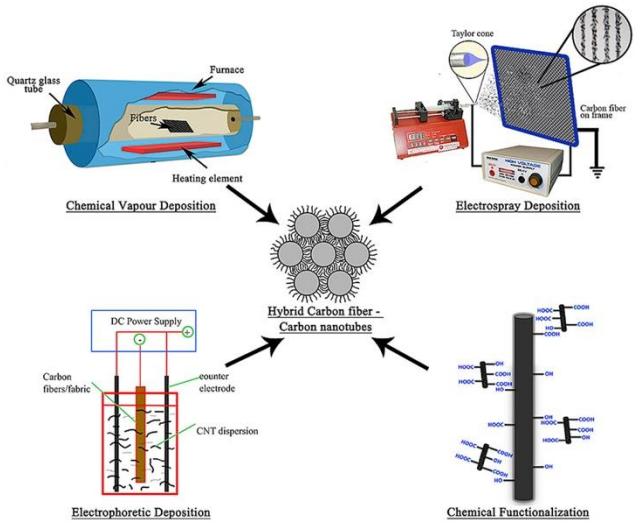

Figure 1.1 Illustration of various deposition and functionalization techniques to grow CNTs on a carbon fiber surface (Zakaria et al., 2019).

A vast variety of nano-fillers were introduced to CFRPs by multiple researchers. These include graphite nanoplatelets (GNPs); nanodiamonds (NDs); carbon nanofibers (CNFs); nano-gold; iron oxide; nano-silver; nano-clays, nano-silicas (De Cicco et al., 2017). In the following sections, three such nano-fillers addressed in this dissertation will be discussed.

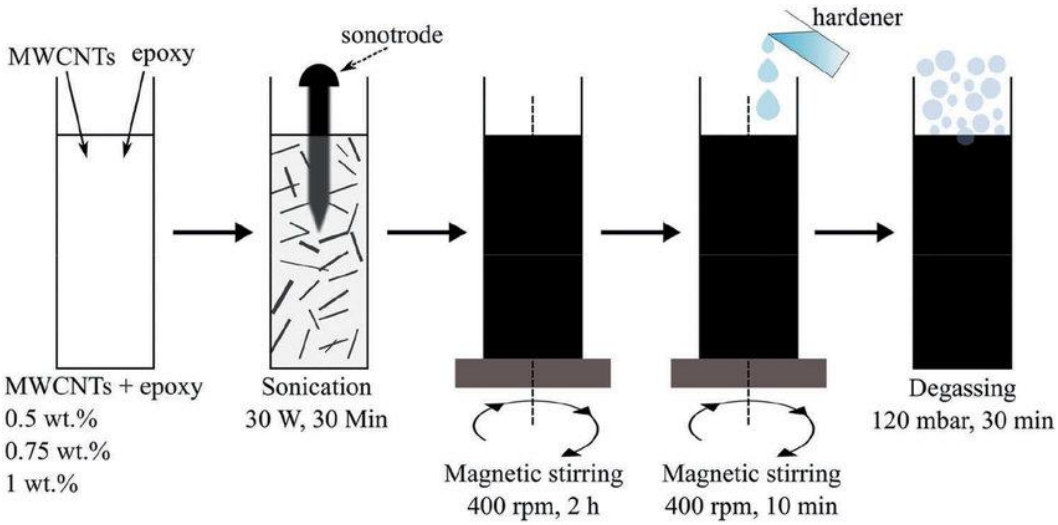

Figure 1.2 Illustration of adding CNTs to a polymer matrix (Sanli, 2020).

1.2. Zinc Oxide (ZnO) Nanorods

Zinc Oxide is an inorganic compound belonging to the II-VI semiconductor group. This material has a hexagonal wurtzite structure, with anions of zinc (Zn^{2+}) surrounded by four cations of oxygen (O^{2-}) in tetrahedral coordination, as seen in Figure 1.3. This combination would generally result in a covalent nature of iconicity. However, this material exhibits a substantial amount of ionic bonding too. This results in a higher bandgap, allowing ZnO to exhibit good piezoelectric and pyroelectric properties (Morkoç & Özgür, 2009). Another property pertinent to this material is its morphological versatility. It can be grown on most substrates in a variety of nanostructures including: nano-rods; nano-wires; nono-belts; nano-rings; and nano-spirals (Z. L. Wang, 2004). Among these morphologies it is speculated that ZnO nanorods possess the potential to be a good nano-filler in hybrid CFRPs.

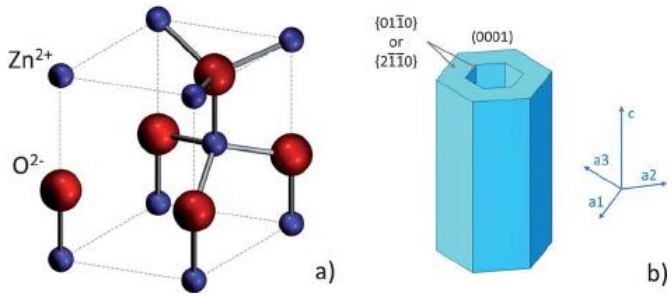

Figure 1.3 a) Oxygen and Zinc atoms in a tetrahedral arrangement. b)Single ZnO nanorod of wurtzite structure with three growth directions (Taghavi et al., 2013).

Considering the poor interaction between ceramics and carbon, to adhere ZnO nanorods to carbon fiber, some surface functionalization should be carried out. For example, polymerized links of polydopamine (PDA) were employed in this dissertation for this purpose. This method was inspired by the study of mussel adhesive proteins (Ryu et al., 2018). In that study, it was theorized that a blend of catechol and amine can assist in enhancing interfacial adhesion between surfaces. This resulted in the discovery of dopamine with an identical combination, along with a unique ability to auto-polymerize in the presence of aerated basic solutions like tris buffer, as shown in Figure 1.4. This makes it the most versatile single-step functionalizing method, requiring no surface preparation, or cleaning; especially suitable for large, low-energy surface areas.

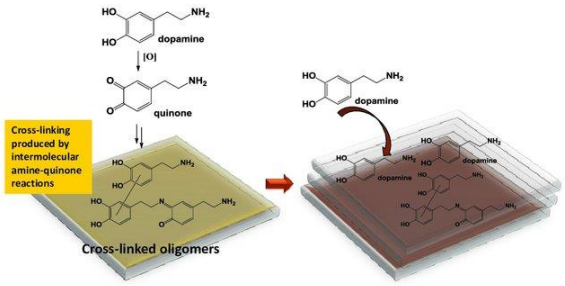

Figure 1.4 Illustration of auto-polymerization in dopamine (Alfieri et al., 2018).

1.3. Carbon Nanotubes (CNTs)

Carbon nanotubes can be envisioned as rolled graphene sheets of very small diameters, typically in nanoscale. Multiwalled carbon nanotubes (MWCNTs) were recognized as a different structural material by Iijima in 1991. These are composed of multiple diameters of rolled graphene sheets nested in each other. Until this discovery, this residual material was just assumed to be a smaller version of the commonly known vapor-grown carbon fibers (Sinnott & Andrews, 2001). Single-walled carbon nanotubes (SWCNTs) were synthesized later in 1993. These are made of single tubes of one graphene sheet at a certain chirality, closely packed as a crystalline rope. Regardless of the type, CNTs form a unique network of pure carbon atoms due to the robust sp^2 chemical bond between them. This geometry framework of CNTs is responsible for all the outstanding properties which attract new applications. These properties include extreme mechanical strength, stiffness, and thermal conductivity, next only to diamond, and electrical properties better than copper. Due to these exceptional straits, CNTs have the potential to enhance the properties of a hybrid composite and transform it to become multifunctional (Peng et al., 2016).

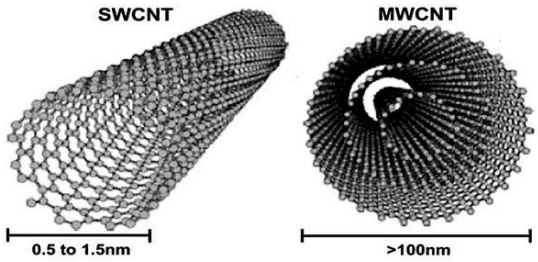

Figure 1.5 Schematics of SWCNT and MWCNT (Ribeiro et al., 2017).

1.4. Importance of Topology

This section highlights the importance of tailoring the nanofiller density by defining a desired topology on each carbon fabric. Topology can be defined as the spatial relationship of different constituents composing a network; the arrangement of the network of nanofillers.

There are several techniques available in the literature to grow CNTs or ZnO nanorods on a carbon fiber surface. These will be described in more details in the next chapters. The topology of the grown CNTs and ZnO NRs can be uniform, patterned, or randomly scattered, based on the density required for the application. Highly dense and uniform nanofillers are desirable in electric conductivity and magnetic applications. In the case for structural performance improvements, the objective for hybrid CFRPs, which are multifunctional, is to achieve better mechanical properties.

In structural applications, extremely dense intermediate layers of nanofillers could prevent the epoxy from seeping in between individual fiber strands or even between the laminate plies. This in return reduces the strength of the final hybrid composite. Hence, controlling the density of nanofillers could help in retaining good mechanical properties. In addition, patterned nanofillers act as hurdles for interlaminar crack, which propagates through the sample in between layers. This might result in hybrid CFRPs with a gradual failure model, rather than a catastrophic failure. Controlled topology can also assist in developing sensory equipment, whose behavior can be easily controlled and predicted. This dissertation employs different patterns of each nanofiller and characterizes their effect on mechanical properties.

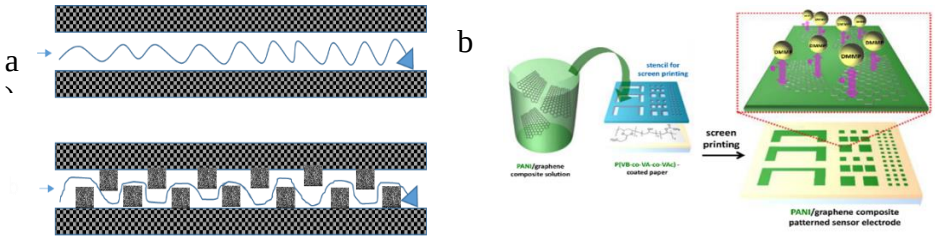

Figure 1.6 a) Patterned nanofillers acting as hurdles in crack propagation, the arrow indicating crack growth direction. b) Illustration of nanofiller patterns used in sensing (Yáñez-Sedeño et al., 2020).

1.5. Metal-Organic Frameworks (MOFs)

While fabricating hybrid composites in lab scale is attainable with ease, one of the major concerns for real-world application is scalability. The synthesis process of most nanofillers (e.g., patterned CNTs and ZnO NRs) requires controlled environment (vacuum, high temperature, inert, etc.) such as those furnished by physical vapor deposition (PVD) and/or chemical vapor deposition (CVD). However, these techniques, as will be discussed in detail in further chapters, lack scalability. In this section, one novel technique used to tackle the issue of scalability in hybrid CFRPs is discussed.

Metal organic frameworks (MOFs) are materials mainly composed of positively charged metal ions surrounded by organic linker molecules, as shown in Figure 1.7. This combination of organic-inorganic linkage is repeated in a large number of arrays to form crystalline, porous materials, with huge surface areas (Furukawa et al., 2013). This immense flexibility in choosing the metal ions resulted in a large variety of MOFs. For example, one of the MOFs resembled the enzyme in plants, which is responsible for capturing CO_2 from the atmosphere (Singh et al., 2021). Similarly, researchers discovered multiple MOFs, unique to many different applications. Some of the applications include

gas detection and storage, biomedical microrobots, drug delivery, among many others (Sule & Mishra, 2020).

In this dissertation, a specific MOF based on a nickel-metal ion is employed for increasing the surface area on the carbon fibers fabric. Available surface area for epoxy seepage on a carbon fiber surface largely determines the interlaminar properties of the hybrid CFRP. This additional MOFs at the fiber/matrix interface can improve the shear and longitudinal strength of the composite. In addition to improving the mechanical properties, this MOF can be used as a catalyst to grow CNTs, thus, eliminating the need for PVD in that regard. The method of synthesis used for the growth of this MOF is very scalable to any size of carbon fabric. This will be described in detail in further chapters.

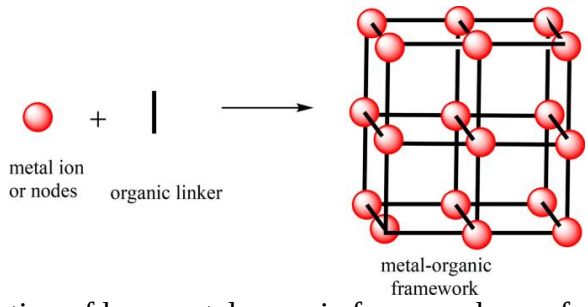

Figure 1.7 Illustration of how metal-organic frameworks are formed (Singh et al., 2021).

1.6. Modeling Techniques

Modeling in composites has been a challenge due to the complex nature of interlaminar bonding between fiber and matrix. Some softwares like ABAQUS, ANSYS, and MSC NASTRAN offer certain modules built specifically for the mechanical analysis of composites. If intrinsic detailing at a molecular level is desired, molecular dynamic (MD) simulations using Large-scale

Atomic/Molecular Massively Parallel Simulator (LAMMPS) or Material Studio software packages are performed. In this dissertation, both MD and ANSYS were utilized for two different applications that are briefly discussed in the next section.

1.6.1. Fracture Analysis Using ANSYS Model

One of the major concerns with composite structures is their catastrophic failure specially for angle ply layups. To mitigate this, nanofillers could be used to provide resistance during crack propagation. This theory was investigated using both experiments and simulations. The experimental setup will be explained in detail in Chapter 7. Some of the results from these experiments were used to build a model in ANSYS to predict the failure behavior of the fabricated hybrid CFRPs. ANSYS Composite PrepPost (ACP) module is useful for designing and analyzing multilayered composites. This module was utilized to study the propagation of a pre-induced crack in a fabricated hybrid composite, under a Mode I loading. Mode I is also called the opening mode, stipulating that the load is applied perpendicular to the plane of the crack. The different modes of fracture are shown in Figure 1.8.

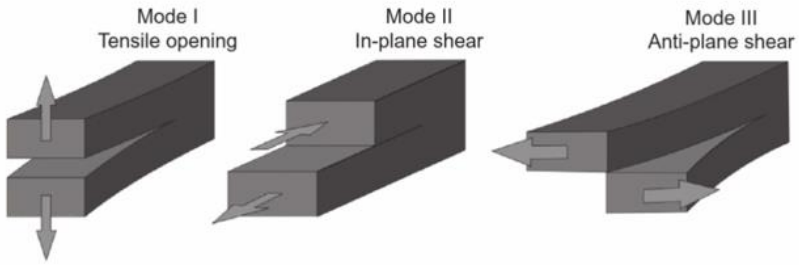

Figure 1.8 Illustration of various modes of fracture (Oterkus et al., 2016).

1.6.2. Molecular Dynamics (MD) Simulations

This simulation technique is used to study the time evolution of an initial system of particles at a nano scale. At the initial stage, the forces and moments acting on each atom are calculated using empirical force fields. These are used to calculate the potential energy of the entire system of atoms. At every time step, this process is repeated to dynamically track various energy parameters. This process can eventually assist in detecting all the thermodynamic properties of the system. Investigators used MD for diverse applications: in medicine to study protein-protein interactions (Perricone et al., 2018); in chemistry to study solute-solvent interactions (X. Li, 2011), simulation of polymer flows; design of nanomaterials (Case, 2011), among many others. In this dissertation, MD is utilized to simulate the flow of epoxy in between ZnO nanorods, when assembled on a graphitic surface mimicking the carbon fiber surface. This system was built using Materials Studio software (BIOVIA-Dassault Systèmes). An attempt to compare the mechanical properties of the system with, and without ZnO nanorods was made.

1.7. Dissertation Proposal and Outline

The overarching goal of this dissertation is to investigate the effect of different surface modifications on carbon fibers by nanofillers on the mechanical performance of their derived polymeric composites. These nanofillers include zinc oxide nanorods, carbon nanotubes, and metal organic frame works. The effects of different geometrical patterns of growth of these different materials on the composites mechanical performance is investigated in depth both

experimentally and computationally.

This dissertation comprises nine chapters to provide the reader a better understanding of the purpose, procedure, and results of the various hybrid composites investigated. Chapter 1 introduces various hybrid composite materials, advantages of topological surface modification, and some modeling techniques used to study the hybrid composites. Chapter 2 presents a detailed literature review on the materials and modeling techniques introduced briefly in Chapter 1. Chapter 2 also introduces the description of a few experimental procedures used in this dissertation to grow various nanomaterials like CNTs and ZnO nanorods. Chapter 3 details all the experiments performed for the mechanical characterization of hybrid composites with ZnO nanorods as nanofillers. Chapter 4 outlines the procedure for a molecular dynamics study of the effect of ZnO nanorods on the mechanical performance of hybrid composites and presents results from these simulations.

The mechanical characterization of hybrid composites with CNTs as nanofillers is detailed in three different chapters. Chapter 5 details tensile test results, DMA results, and fracture analysis. Chapter 6 presents a detailed discussion on viscoplasticity in CNTs hybrid composites. Apart from the experimental results of stress relaxation and creep, an analytical creep model is also discussed at length in this chapter. Chapter 7 presents a study of crack propagation in CNTs hybrid composites. Both experimental and modeling techniques using ANSYS models are compared.

Chapter 8 details all the experiments performed for the mechanical

characterization of hybrid composites based on MOFs surface modifications of carbon fibers fabrics. Chapter 9 summarizes all the experimental and computational model findings while offering a few suggestions for future work.

2. Review of the Relevant Literature

This chapter showcases the evolution of hybrid composites including the nanofillers growth techniques for ZnO nanorods, CNTs and MOFs. The applicability of molecular dynamics simulations for the study of adhesion at the nanofillers/fiber/matrix interface is discussed. A study of experimental and modeling techniques to predict crack propagation in hybrid composites is also presented.

2.1. Growing ZnO Nanorods on Carbon Fibers

There are several methods utilized by researchers to grow ZnO nanorods on various substrates. Some of the methods include electrodeposition (J. Yang et al., 2015), sol-gel synthesis (Khan et al., 2016), electrospinning of zinc salts to fabricate a template (J. Liu et al., 2016), photolithography techniques (Tak & Yong, 2005), metal-vapor deposition technique (Lyu et al., 2002), nanosphere lithography (Byrne et al., 2011), among others.

In the case of woven carbon fiber, the surface is uneven and curved due to interlaces between the warp and woof yarns. Also, their properties are highly sensitive to the hygrothermal nature of ZnO growth process. Hydrothermal growth causes minimal degradation in fiber mechanical properties, hence, affecting the hybrid composite performance.

Hydrothermal methods principal theory is to subject a substance that is insoluble under normal conditions to a high temperature and pressure to make it soluble. The pressure can be external or self-vapor pressure. The ions and molecules of the originally insoluble substance are now available in the aqueous

solution. In the presence of a temperature gradient, these ions get deposited and crystallize on the substrate located in the low-temperature region. This process was originally carried out in highly expensive autoclaves. With time, the kinetics of this process was understood to reciprocate this technique in ovens and microwaves (G. Yang & Park, 2019).

Currently, this technique has become the most common method to synthesize nanomaterials. This is because of few crucial advantages: The ability of this technique to crystallize nanomaterials that are highly unstable at elevated temperatures; The possibility to use the inherent vapor pressure of the reactants results in minimal material losses; Ease of control of the aqueous solution; The process can be split into multiple chemical reactions if required. Hence, several nanomaterials like silver nanoparticles, carbon quantum dots, titanium dioxide hollow nanospheres, titanate nanotubes, ZnO nanorods, and so on were synthesized using this technique (Gan et al., 2020).

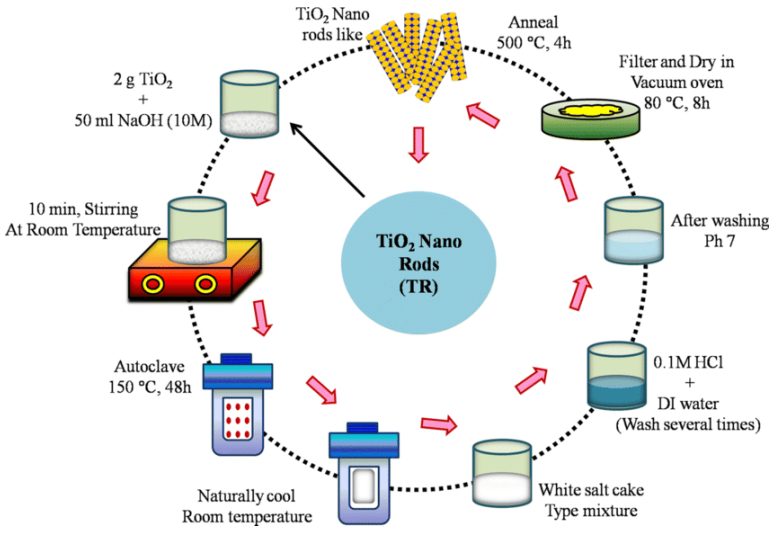

Figure 2.1 Hydrothermal method used for the growth of titanium oxide nanorods (Pawar et al., 2019).

Using this hydrothermal technique, various methods to grow ZnO nanorod crystals on carbon fiber surfaces have been developed. Reactants in the aqueous solution and the growth conditions to crystallize ZnO nanorods are the major variants in each method. Various zinc salts like zinc acetate, zinc chloride, and zinc nitrate hexahydrate were used as precursors to grow ZnO nanowires. For precise control of the size and shape of these nanorods, a two-step procedure was usually adopted by most groups (Akgun et al., 2012). Several investigators (Galan et al., 2011; Lin et al., 2009) used zinc acetate dihydrate and sodium hydroxide dissolved in ethanol to prepare a seeding solution for depositing ZnO quantum seeds on a carbon fiber strand.

For the growth process, zinc nitrate hexahydrate, and hexamethylenetetramine were dissolved in water. A low temperature of 90 ºC was maintained during the crystallization process. Al-Haik research group (Ayyagari et al., 2018; Ayyagari & Al-Haik, 2019) also utilized a two-step process involving seeding and growth to grow ZnO nanorods. The seeding solution was relatively simpler: zinc acetate dihydrate dissolved in deionized water and ethanol. The growth solution was a homogenized mixture of zinc acetate dehydrate and hexamethylenetetramine (HMTA). HMTA was proven to be crucial for two purposes: pH regulator; induces the anisotropic growth of ZnO nanorods only in the vertical c-axis direction. This prevents any lateral growth of nanorods on the carbon fiber surface, hence, providing a directional interface (Strano et al., 2014). The growth temperature was the same as the group previously mentioned, at 90 ºC. A different seeding procedure was adopted by

this group in a separate investigation (Skandani et al., 2012). A thin film of ZnO was deposited on carbon fabric using the physical vapor deposition technique (PVD). This technique resulted in a more uniform distribution of nanorods on the curved carbon fiber surface after the growth process.

To facilitate a better adhesion between ZnO nanorods and the surface of a substrate, various functionalizing methods were developed. Increasing the surface area and creating a texture accommodates stronger van der Waals bonding between polymer and fiber. One such method was to introduce a carboxylic acid group on the fiber surface. This was experimented by Ehlert and Sodano (2009) on aramid fibers. After an initial fiber treatment in an aqueous sodium hydroxide (NaOH) solution, the fibers were washed in hydrochloric acid (HCl). The growth of ZnO nanorods using the hydrothermal method was followed after this functionalization procedure. This led to a 51% increase in interfacial strength between the fiber and polymer.

A relatively simpler method of functionalization is to introduce polymerized links of polydopamine (PDA) on the carbon fiber surface. This is a single-step method that requires no prior surface preparation. Dopamine was inspired by the study of mussel adhesive proteins (Ryu et al., 2018). This research speculated that the blend of catechol and amine can assist in enhancing interfacial adhesion between surfaces. This has led to the discovery of polydopamine with the exact combination of catechols and amines, along with its' unique ability to auto-polymerize in the presence of aerated basic solutions like Tris buffer. This method was previously adopted to enhance the adherence of ZnO nanorods on

various substrates like cotton fabric (Ran et al., 2018) and carbon fiber (CF) fabric (F. Xie et al., 2018).

2.2. Growing Carbon Nanotubes (CNTs) on Carbon Fibers

There are several methods to introduce CNTs into CFRPs. The most intuitive two methods are: Blend CNTs with the polymer matrix, then use this enriched matrix to impregnate the fiber fabric; or modify the fiber surface to host CNTs. Various research groups used the former technique to improve the interfacial adhesion between carbon fibers and polymer matrix (Abdelal et al., 2018). However, the agglomeration of CNTs to form segregated islands created an opposite effect. To address this problem, various studies to understand the suspension of CNTs in various solvents like water and 1-Cyclohexyl-2-pyrrolidone (CHP) were also conducted (Deriabina et al., 2013).

Parallel to these efforts, other research groups worked on the modification of carbon fibers with CNTs. One surface effort was the deposition of CNTs onto carbon fiber's surface through the combination of ultrasonics and electrophoretic deposition technique (Jiang et al., 2016). Other groups used chemical vapor deposition (CVD), with catalysts like ferrocene, and high-temperature conditions ranging from 700 to 1300 ºC to grow CNTs on carbon fiber surface (An et al., 2012; Pan et al., 2017; Rahmanian et al., 2013). Due to fiber degradation at such high temperatures, the graphitic structures by design (GSD) technique was developed (M. Tehrani et al., 2013; Mehran Tehrani et al., 2013). This method uses a relatively lower temperature of 550 ºC and uses nickel as a catalyst.

In this dissertation, physical vapor deposition (PVD) was utilized to deposit

nickel as a catalyst. This is followed by GSD procedures for the growth of CNTs. Since GSD is an extension of CVD, PVD and CVD are discussed in detail here. Physical vapor deposition is a process used to deposit thin films of organic and inorganic materials on a substrate. In general, there is a solid or source (target), from which atoms or ions are bombarded in a vacuum chamber, to be transported onto the substrate surface, while flowing inert gas, forming a plasma. Although there are various types of PVD, magnetron sputtering was employed in this work. This technique uses strong permanent magnets to generate a magnetic field at the surface of the target (source). This confines the electrons at the surface too, accommodating sputtering at low pressures and higher rates. This method works well on flat or near flat substrates like carbon fiber cloth. However, arcing due to contamination of the chamber with relatively conductive loose carbon fibers can result in target damage or radio frequency (RF) power supply failure which was encountered many times during the course of this dissertation. Therefore, extreme caution is needed while mounting the substrates (Mattox, 2002).

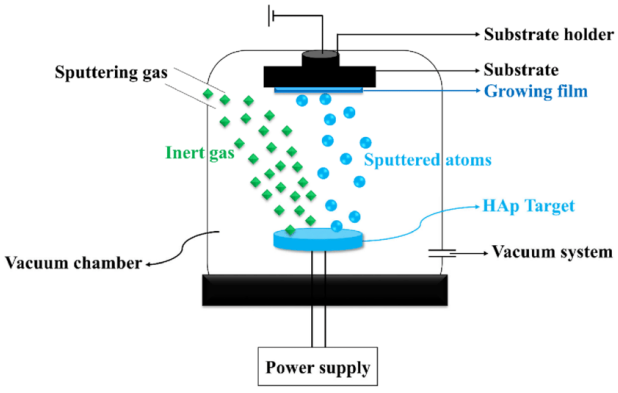

Figure 2.2 Schematic illustration of the physical vapor deposition (PVD) process (Safavi et al., 2021).

Moving the emphasis to CVD, it is a widely used synthesis technology in the materials processing industry and research. In this process, the films are deposited on the substrate through chemical reactions in a gaseous phase. The substrate is usually placed in a reactor (e.g., quartz tube furnace) and heated to high temperatures ranging from 500 to 1300 ºC. Gases and catalysts involved in the desired chemical reaction are flown into this chamber. Through the surface diffusion process, the reactants are adsorbed on the substrate. This is followed by their nucleation on the substrate surface to form thin films. Most reactions do not require a vacuum enclosure, making this process very versatile (L. Sun et al., 2021).

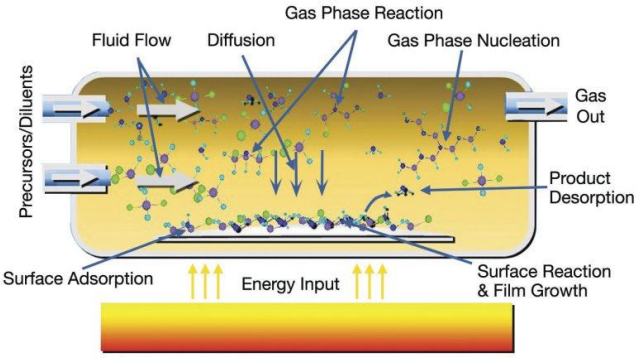

Figure 2.3 Schematic illustration of the chemical vapor deposition (CVD) process (Anon, 1989).

2.3. Synthesis of Metal-Organic Frameworks (MOFs)

As introduced earlier, this is a technique that has the potential to address the issue of scalability while creating a stiff and strong interphase between the carbon fiber and the polymer matrix. Both PVD and CVD are restricted by the sample size that fits in the vacuum chamber or the quartz tube, respectively. This hinders fabricating composites large enough for industrial applications like

airplane structures. In previous research, MOFs were used with carbon materials for non-structural applications such as catalysis, gas adsorption, or enhanced transport properties. For instance, Lei Du et al., (2020) reviewed the usage of MOF-derived carbon materials to replace expensive platinum-group metal-based materials as catalysts during electrocatalytic oxygen reactions. In a similar context, Tian et al., (2020) reported a technique to synthesize non-precious metal nitrogen-doped carbonaceous materials, using cobalt as the metal, to help in oxygen reduction reactions, required in electrolysis.

Metal organic frameworks were also used to prepare porous carbon materials, which exhibited properties viable as precursors in supercapacitors (Hu et al., 2010). These porous materials have further exhibited promising results as catalysts for hydrogenation reactions in chemistry (Shen et al., 2020). In some cases, a conductive matrix of activated carbon was used to make MOFs more electrically conductive (Fleker et al., 2016). Other works used these materials in ridding the environment of pollutants using adsorption techniques (Sule & Mishra, 2020; J. Wang et al., 2020). In another review, the applications of nanocomposites based on graphene, CNTs, ZnO nanorods in combination with MOFs were discussed (X. W. Liu et al., 2016). In this dissertation, MOFs were incorporated in CFRPs and their mechanical properties were characterized.

2.4. Molecular Dynamics (MD) Simulations and Hybrid Composites

Molecular dynamics (MD) simulation was used by researchers to understand the solubility, stability, compatibility, and/or resulting properties of two or three different materials, when put together, to form a nanocomposite or a

homogenous/ inhomogeneous solution. Xin et al., (2011) summarized few papers that employed MD to describe the chemistry of different solvent ions in water.

Some of them were to find the nuclear magnetic resonance (NMR) of transition metals like zinc, mimicking them with cadmium ions, essential because of their abundance in enzymes and living organisms; Absorption study of titanium oxide in proteins to develop better biosensors or biomedical devices; Solvation energy calculations resulting from dissolving metal ions in water; Understanding the effect of aerosol particles on a cloud by modeling the solubility of various cloud condensation nuclei like cis-Pinonic acid, humic-like substances, glycine and amino acid in atmospheric droplets.

In the field of composite materials, MD was used by multiple researchers to study the cross-linking of thermoset polymers. One such study offers the prediction of mechanical properties like, glass transition temperature, Young's modulus, and linear thermal expansion coefficient of a fully cross-linked epoxy network, which included EPON 862 as resin, and triethylenetetramine (TETA) as the hardener (Fan & Yuen, 2007). The predictions, when compared to experimental values were within 10% error range.

A similar study with EPON 828 and diethylenetriamine (DETA) as resin and hardener was performed with various force field options, which included Condensed-phase Optimized Molecular Potentials for Atomistic Simulation Studies (COMPASS), Polymer Consistent Force Field (PCFF), Universal Force Field (UFF), and Dreiding, available in Materials Studio MD simulation software (Arab et al., 2012). The study concluded that COMPASS and PCFF

force fields are more reliable to characterize cross-linked polymers. A review paper published by Chunyu Li and Strachan (2015) on various studies based on thermoset polymers used in industries like aerospace and electronics, provide a detailed summary of their thermomechanical response exhibited during MD simulations.

These cross-linked polymers were further combined with carbon nanotubes (CNTs), graphene, and carbon nanofibers (CNFs) to mimic real-life composites using a representative nanoscale molecular structure. One such study modeled carbon nanofibers (CNFs) in a polypropylene (PP) matrix. The purpose was to study the effect of the volume fraction and aspect ratio of CNFs on the mechanical properties of the resulting nanocomposite. An increase of 748% in elastic modulus (E_{11}) was reported with a 2% volume fraction of CNFs (S. Sharma et al., 2016).

Graphene was modeled with a polyethylene matrix and diglycidyl ether (DGEBA) / TETA matrix in two separate works. The former work concluded that the usage of polycrystalline graphene over pristine graphene results in better interfacial adhesion due to their higher tensile, interfacial shear, and normal cohesive strength values in comparison (Verma et al., 2019). The latter aimed at documenting the effects of defects like single-vacancy (SV), double-vacancy (DV), and Stone-walls (SW) generally seen in graphene, on the interfacial mechanical properties of the resulting composites. SV and DV defects degraded the cohesive and shear strength values, while SW defects improved them (M. Li et al., 2017). Hadden et al., (2013) performed a larger scale simulation with

graphite/epoxy combination. In this case, the graphite structure was designed as a ply to be layered in the simulation box with cross-linked epoxy. They studied the effects of density fluctuations of the cross-linked polymer on the interfacial properties of the composite.

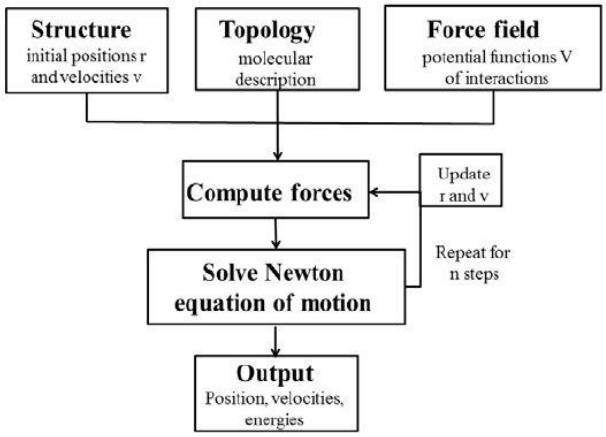

Figure 2.4 Simple illustration of the workflow of Molecular Dynamics Simulations (Sonavane et al., 2014).

The investigation of adhesion at the interface of fiber and matrix was also attempted using carbon fibers (T300 and CCF300) and various epoxy systems for comparison (Sadiq & Wang, 2012). Some works attempted to study the effect of functionalization using a representative model composed of a single carbon fiber strand with -COOH functional groups sandwiched in an epoxy system (H. Wang et al., 2019). Finally, some hybrid three-phase composite models with the addition of nanofillers like CNTs in a graphene/epoxy system (S. Sun et al., 2019) and CNTs in amine functionalized Carbon/epoxy system (K. Sharma & Shukla, 2014) were also modeled by separate groups. An attempt to build a similar three-phase hybrid model with ZnO nanorods as nanofillers in a Carbon/epoxy system was made in this dissertation.

2.5. Crack Propagation in Composites

Unlike largely homogenous metals, composite structures are anisotropic in nature. This is due to the directional variation in stiffness of the lamina and the disparity of properties among the involved constituents like the nanofillers, fiber, and matrix. Hence, the fracture analysis is significantly different from metals. Catastrophic failures and delamination due to stress concentrations at machined regions like bolt heads or notches are majorly seen and recorded phenomena in composites.

Among various setups to understand and predict delamination, Mode I double cantilever beam (DCB) is the most widely used (Nasuha et al., 2017). A thin Teflon film is usually inserted into the mid-plane of a laminate during the manufacturing process to introduce a starter crack. A tensile load is applied over the piano hinges in the loading direction at a rate of 1-5 mm/min. The crack growth due to this load is monitored using digital image correlation (DIC) techniques (Saadati et al., 2020) or microscopic techniques (Boroujeni & Al-Haik, 2019). This method was used by multiple researchers to study interlaminar fracture in glass/epoxy (Samborski et al., 2019) and carbon fiber/epoxy (Borowski et al., 2015; Murray et al., 2018) laminates.

Due to the complexity in the experimentation procedure to understand delamination in composites, various finite element softwares like ABAQUS (Zhao et al., 2016) and ANSYS have exclusive modules developed for this purpose. There are two computational techniques to model delamination in ANSYS: Cohesive damage models and; fracture mechanics models. In the

former method, there are interface elements or contact elements defined with a cohesive material behavior in between the two delaminating surfaces. Hence, it is called the cohesive zone method (CZM). This model calculates progressive stiffness reduction in this cohesive zone during delamination to estimate the final fracture parameters. In the latter method, the propagation of delamination is proceeded by comparing the energy release rate (ERR) with the fracture toughness of the interface material.

The crack growth approaches developed by Griffith and Irwin form the basis for Virtual Crack Closure Technique (VCCT) used in ANSYS. This method does not consider the plastic effects at the crack tip into consideration, as it implements linear elastic fracture mechanics (LEFM) (Bahei-El-din, 1996). A proposed algorithm to implement this method in detail was published by De Xie and Biggers (2006). A comparison between CZM and LEFM techniques was drawn using some DCB test specimens by Turon et al., (2010). In this work, an attempt was made to model the delamination in various configurations of the fabricated composites, using some experimental data, as input.

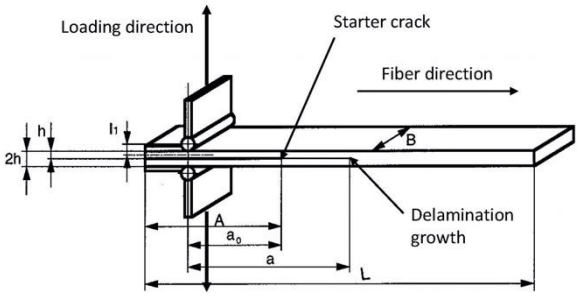

Figure 2.5 Illustration showing a standardized DCB composite specimen (May, 2016).

3. Experiment with ZnO Based Surface Modifications

In this chapter, all the experiments and results of hybrid composites fabricated by modifying carbon fiber surfaces using ZnO nanorods were discussed. Various composite configurations, fabrication techniques and testing procedures involved were discussed in detail.

3.1. Composite Configurations and Fabrication

In this experiment, two sets of three-plies composites were prepared: Functionalized with polydopamine before (PDA_B); after (PDA_A); before and after (PDA_BA) nanorod growth; Patterning with 105μm; 53μm mesh; ZnO coated only fibers (Coated), to be compared with: no nanorods (As Is); uniform growth of ZnO nanorods on fibers with no PDA or patterning (Full Growth). The tensile and damping properties of these composites were compared to study the effect of topology and functionalization due to dopamine.

The laminae used in this experiment were made of plain woven polyacrylonitrile (PAN) based carbon fibers (ThornelT650, Solvay, Inc), with 3000 carbon fiber strand. These fibers were de-sized by exposing them to a temperature of 550 °C, for 30 min, in an inert atmosphere created by running nitrogen gas in a tube furnace. This was followed by the growth of ZnO nanorods, utilizing a hydrothermal method described in the literature (Gan et al., 2020; Lin et al., 2009; Skandani et al., 2012), on both sides of each individual laminae, as reinforcements between layers. This method involves the deposition of ZnO nanoparticles as catalyst on the woven fibers to facilitate growth on the surface. Physical vapor deposition (PVD) technique, using an ATC Orion high-

vacuum magnetron sputtering system, was utilized for this purpose, to achieve more uniform and targeted growth. A 75 nm thick layer of ZnO nanoparticles was sputtered on both faces of the carbon fibers fabric, under a pressure of 5 millitorr argon gas, and a 75 W power supply to the zinc oxide sputtering target.

The physical topology was altered by sputtering nanoparticles through two perforated polyester mesh templates: with a mesh size of 105 and 53 μm, thread diameters of 70 and 31 μm, and open area of 33 and 40 %, respectively. The templates are shown in Figure 3.1, captured by a light microscope. Identical to the nickel patterning seen in Figure 3.1, sputtering through the mesh yields scattered checkerboard patterns of ZnO nanoparticles on the carbon fabric. In an effort to enhance the surface adhesion between the ZnO nanorods and the fibers and epoxy interfaces, the chemistry of the carbon fabric surface was altered by functionalizing it with polymerized links of polydopamine (PDA). Auto-polymerization was induced by adding dopamine hydrochloride, 99 % purity, and Tris, 0.5 buffer solution with a pH of 8.5 (Alfa Aesar, Co.) in a ratio of 1:0.6 to 500 ml of de-ionized (DI) water. The carbon fabric was immersed in this solution for 24 h and dried later for 2 h at 80 °C.

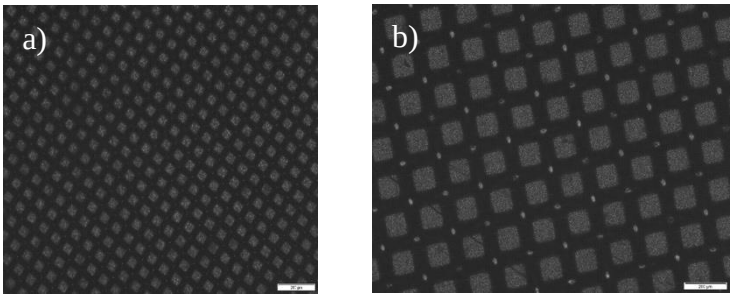

Figure 3.1 Patterned nickel on a silicon wafer using a) 53 μm and b) 105 μm masks.

The seeding and/ functionalizing procedures were followed by the growth of

ZnO nanorods. A chemical solution of predesignated amounts of zinc acetate dehydrate and hexamethylenetetramine (HMTA) (Alfa Aesar, Co.), in DI water was prepared, for each configuration. For a single composite configuration with three layers, 7.902 g of zinc acetate dehydrate and 5.046 g of HMTA in 1800 ml of DI water were homogenized by sonication using a Vibra-Cell VCX 500 tip ultrasonic processor. Each lamina was immersed in 600 ml of this solution, at 90 °C, for 7 h. The fabrics were dried afterward at the same temperature for 24 h.

Scanning electron microscopy was used to inspect the effect of the different chemicals and morphologies on the ZnO nanorods growth. Figure 3.2 reveals the proof of concept for the growth of islands of ZnO nanorods on a silicon wafer. The mesh used in this case was much bigger, as it was a pool-screen mesh. This was easier to image with than the smaller patterns like 53 µm and 105 µm. Figure 3.3 shows the islands of ZnO nanorods when PVD sputtering was through a 53 µm mesh. Figure 3.4 and Figure 3.5 show ZnO nanorods that grew uniformly on silicon at different magnifications.

Each composite in this experiment comprised three laminae, with epoxy impregnated in between them. This epoxy (Aeropoxy^{TM}, PTM&W Industries, Inc) is a blend of PR2032, a Bisphenol-based resin, and PH3660, a hardener, in the ratio 100:27 by weight. The former is highly viscous, with a viscosity of 1650 cPs, compared to the low viscosity of 190-200 cPs of the latter, at room temperature. This blend of resin and hardener is reported to result in viscosity of 800-875 cPs, and a glass transition temperature of 91 °C, by the manufacturer. This resin is unique to structural applications, due to its ability to aid the

composite lamination process and efficiently wet out various kinds of fibers. The lamination was performed using the hand-layup procedure. This was followed by curing in an autoclave. A constant pressure of 70 psi, and a vacuum of 25 torr was maintained during this process, adhering to the ASTM standards of D5687 (D5687 ASTM, 2007). This curing cycle involved multiple stages: Maintain an isothermal temperature of 30 °C for 1 h; Ramp up the temperature to 93 °C; Repeat isothermal conditions at 93 °C for 2 h; Ramp down to room temperature.

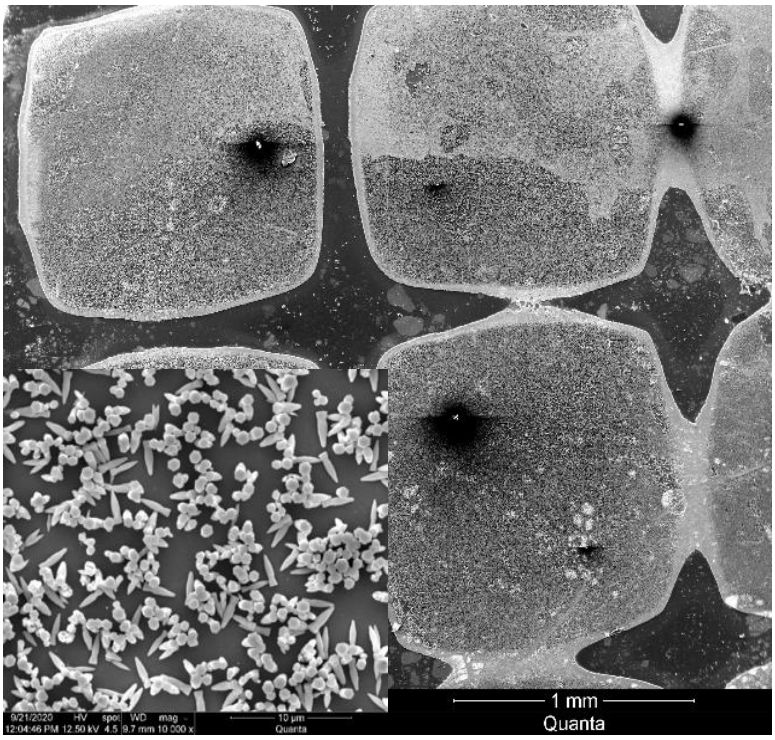

Figure 3.2 SEM micrograph of large islands of ZnO nanorods grown followed by sputtering with pool mesh. The inset figure shows a closer look at these islands.

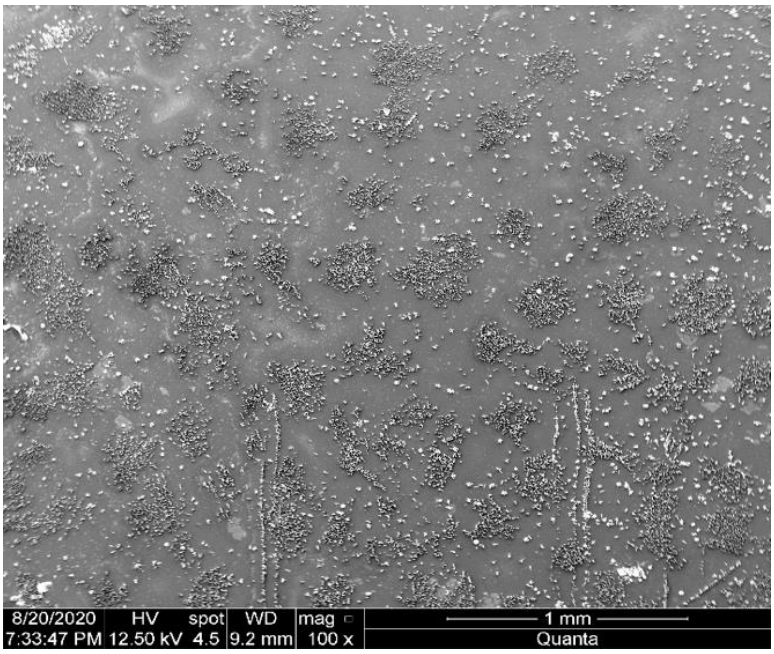

Figure 3.3 SEM micrograph of silicon wafer with islands of 53 µm patterned ZnO nanorods.

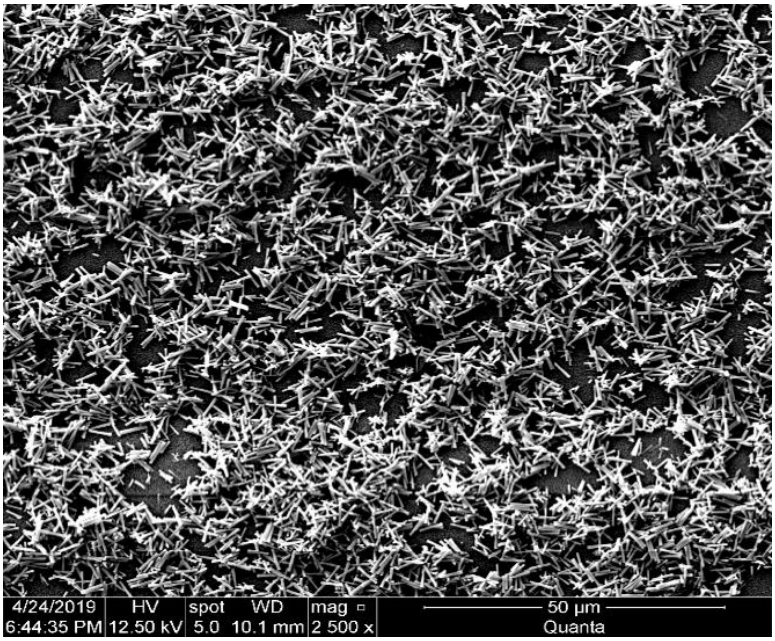

Figure 3.4 SEM micrograph of ZnO nanorods grown after PVD and hydrothermal growth.

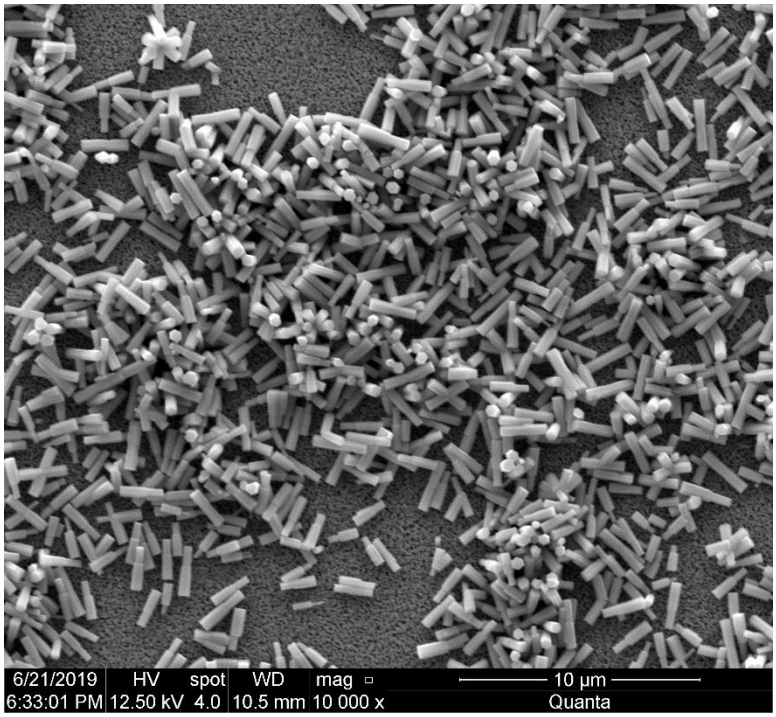

Figure 3.5 SEM micrograph of uniform crystalline ZnO nanorods at higher magnification.

3.2. Mechanical Testing

3.2.1. Strength and Stiffness

These properties can be measured using a simple tensile test. The test setup for this usually comprises of two clamps to grip the samples on both ends, a load cell to apply load in controlled and measurable increments, an extensometer to measure strain while the sample is loaded, and a data acquisition software to collect data in real-time.

In the current work, tensile tests were carried out following the ASTM D3039 standard. This standard is specific to the determination of in-plane tensile properties of FRP materials reinforced by continuous or dis-continuous fibers with high moduli (D3039 ASTM, 1995). The tensile coupons were cut to a dimension of 12.7 x 1.27 cm and, adhered to G-10 glass fiber-based composite

tabs using the same epoxy blend. Tensile tests were performed using MTS Criterion™ Model 43 machine. The strain was measured using a 25.4 mm gauge length MTS extensometer, connected to the MTS controller for real-time data acquisition. These coupons were then mounted in-between the crosshead grips to be pulled until failure, at the rate of 1.0 mm/min. Each configuration had a minimum of eight tensile coupons. The test data was then averaged for final results.

3.2.2. Damping Properties

Response of material under cyclic loads is essential to predict their behavior under possible vibrational environments during their applications. Damping embodies the capacity of a material to absorb or dissipate kinetic energy and is affected by various factors like temperature, stress, frequency, etc. This behavior can be investigated using dynamic mechanical analysis (DMA). The variation in stiffness and damping ability of a material under various conditions can be quantified by different metrics such as loss modulus, storage modulus, and tan delta (δ). These parameters represent energy dissipated, energy stored, and the ratio of energy dissipated to energy stored respectively.

For composites fabricated using ZnO surface treatments, DMA tests were carried out using a DMA8000 analyzer (Perkin Elmer, Inc.) following the ASTM D4065 standard (2011). The samples were cut into 50.00 mm x 6.25 mm coupons and were mounted on a three-point bending fixture of 40 mm span. A constant force of 1.0 N was applied during frequency sweep. A constant strain of 0.01 mm was maintained for both temperature and frequency sweeps. The

frequency sweep was performed through 1 to 100 Hz at a constant temperature of 30 °C. The temperature sweep was performed from 30 to 160 °C, at a constant frequency of 1.0 Hz. Each composite configuration was subjected to both the sweeps.

3.3. Results and Discussion

Various parameters from tensile, and DMA analysis for all configurations were plotted and compared against each other. The following sections show detailed records of all these properties.

3.3.1. Tensile Test Results

Figure 3.6 and Figure 3.7 illustrate the stress vs. strain plots of these three-ply composites. The intermittent kinks within the plausibly linear curves indicate individual ply failures. This debonding pattern is more noticeable in the configurations with nanorod interface. This supports the fact that the tailoring of an additional interface between the plies play a major role in determining the behavior of the composite.

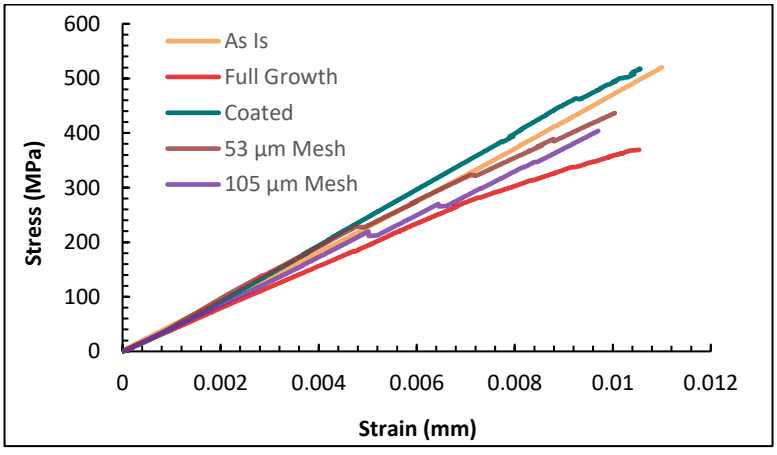

Figure 3.6 Stress vs. strain curves of various composite configurations tailored using both physical and chemical treatment methods.

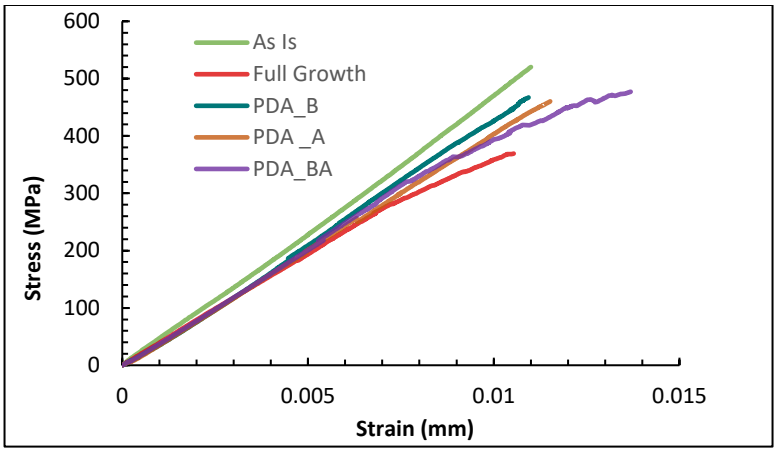

Figure 3.7 Stress vs. strain curves of various composite configurations tailored using both physical and chemical treatment methods.

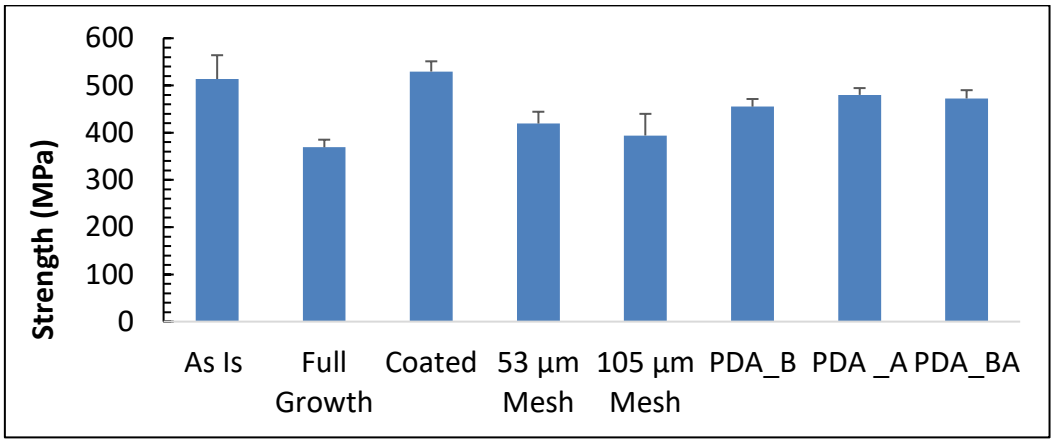

Figure 3.8 Comparison of strength values in MPa for various composite configurations.

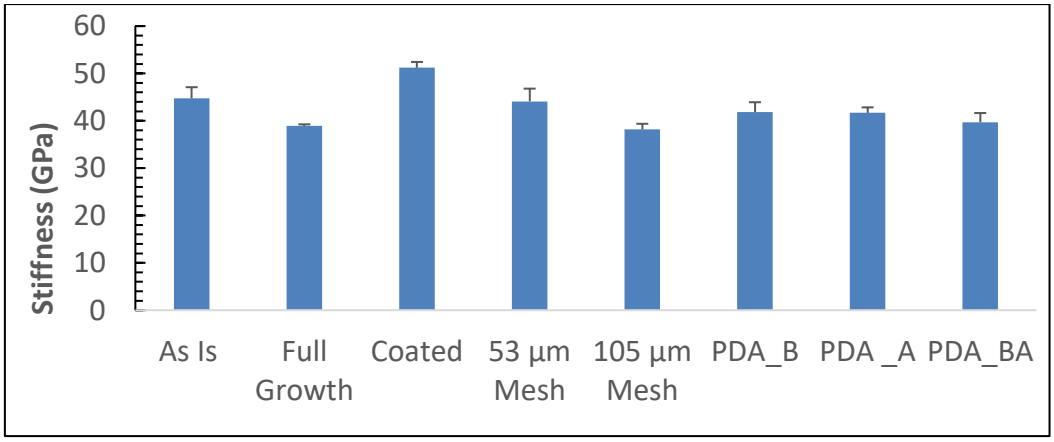

Figure 3.9 Comparison of stiffness in GPa for various composite configurations.

In general, the addition of ZnO nanorods on the carbon fiber provide a possibility for better interphase adhesion by increasing the surface area available between the fiber and the polymer matrix. They protrude into the polymer matrix, introducing a z-pinning effect, and thereby providing a better interlocking between different phases. However, the topology of the nanorod growth, the size of the nanorods (G. Wang & Li, 2007) and fiber functionalization play a major factor in dictating the global composite mechanical properties.

The effect of topology can be clearly seen in Figure 3.6, which displays an increasing trend in load bearing capacity from full growth- 53 µm mesh- 105 µm mesh-based samples. This can be better put into perspective by comparing the values of strength and stiffness as seen in Figure 3.8 and Figure 3.9. Among the three different topologies, the 53 µm mesh-based samples attained a 14 % and 13.3 % increase in strength and stiffness respectively, when compared to the Full Growth based samples. Though the stiffness values of 105 µm mesh-based samples and the Full Growth based samples remained almost the same, the strength of 105 µm mesh-based samples significantly increased by almost 7 %. This data solidifies our theory that, providing optimal spacing between islands of nanorods provide better path flow for epoxy to seep into the fiber, and hence, enhancing the mechanical properties.

In Figure 3.6, it is seen that the Coated sample performed the best, when compared to all other configurations. A similar trend is noticed in terms of both strength and stiffness as seen in Figure 3.8 and Figure 3.9. This can be attributed

to two different factors: lack of exposure to any chemical bath, which can result in degradation of mechanical properties due to residual moisture; enhanced interlocking effect between the fiber and polymer matrix, produced by the sputtered nano ZnO particles on the fiber surface. It can also be seen that the As Is sample performed better than all the composite configurations where ZnO nanoparticles were grown on the interface using hydrothermal method. This can be due to multiple reasons. The size of our nanorods after growth vary from 3 to 6 µm, which can be protruding long enough to hinder good epoxy wetting. Unlike CNTs which are mostly in the scale on nanometers, the ZnO nanorods are significantly longer, as seen in the SEM images (Ayyagari et al., 2020; Godara et al., 2009). This makes optimizing ZnO nanorods on the carbon fiber surface for better mechanical properties more challenging than usual. Also, all composite configurations with nanorods were subjected to a bath solution, which might have led to some moisture absorption in between nanorods during the growth process. This can partly contribute to the degradation in strength as well (Chalykh et al., 2020; Pérez-Pacheco et al., 2013).

Figure 3.7 shows the advantage of functionalizing carbon fiber in enhancing mechanical properties. The self-polymerized Dopamine on the carbon fiber surface would have multiple functional groups including catechol, amino, carboxyl, and quinone (F. Xie et al., 2018). Some of these groups with -OH links readily react with the physically deposited ZnO layer to form a chemically active layer of ZnO layer on the carbon fiber. All the configurations with this surface modification performed better than Full Growth sample, as seen in Figure 3.7.

Figure 3.8 and Figure 3.9 summarize these results in terms of strength and stiffness, respectively. There is a significant improvement in strength, the highest being 30%, for the PDA_A sample. There is a slight improvement in stiffness, around 7% for two of the PDA configurations. These values are in comparison to the strength and stiffness of the Full Growth sample.

These results suggest that the functional groups resulted from polydopamine polymerization were instrumental in adhering ZnO nanorods to the carbon fiber at all times: before nanorod growth, after nanorod growth, and when functionalized before and after nanorod growth. This provides a room for flexibility during the hydrothermal growth process when required. Also, this additional step contributes more towards strength improvement, rather than the stiffness. Finally, the tensile results summarize that, composite configuration with both functionalization and ideally patterned ZnO nanorods could perform better that the As Is composite configuration, in terms of both strength and stiffness.

3.3.2. Damping Results

3.3.2.1. Temperature Scan Results

Figures 3.10 and 3.11 show the variation of storage modulus with temperatures varying from 30 °C to 170 °C for all the mesh-based and dopamine-based configurations. Both figures show a steady drop in the storage modulus with increase in temperature. This is attributed to the weakened cross-linking of the polymer matrix at higher temperatures. Figure 3.10 shows that, the Full Growth and 53 µm mesh samples have higher values of storage modulus

than the As Is sample. This indicates that the nanorods in these configurations provided a significant hindrance to avoid the flow of polymer, hence increasing the stiffness of the sample, reflected in the values of storage modulus.

Figure 3.10 also shows that Coated and 105 μm mesh samples have significantly lower values of storage modulus compared to the As Is sample. The Coated samples do not have nanorods grown on the carbon fiber surface. These fibers were just sputtered with ZnO film using PVD procedure. Their layer thickness was around 75 nm, seemingly insufficient to act as reinforcements. In the case of 105 μm islands, the spacing of the nanorods might not be optimal to provide sufficient amount of hindrance to prevent the epoxy flow.

Figure 3.11 shows that all the polydopamine-based configurations showed a significant drop in storage modulus values in comparison to the As Is configuration. All these sample had ZnO nanorods, fully grown on the surface. This indicates that the dopamine functionalization, through increased surface area spaced out the growth of the nanorods, preventing a collective hindrance effect to avoid the epoxy flow. This phenomenon could attribute for lower storage modulus values.

There is a noticeable sudden drop in storage modulus in all the graphs within a temperature ranging from 55-70 °C. The temperature where this sudden transition occurs is called the glass transition temperature; T_g. At this temperature, the polymer changes its phase from a brittle, solid state to a glassy viscous state. The higher these values of T_g allow for a wider range of operable temperatures for any given material. These values are tabulated in Table 3.1 for

all the mesh-based and dopamine-based configurations. The sample treated with dopamine before and after the growth of ZnO nanorods had the highest value of T_g among all the configurations, with an enhancement of 7.3 % compared to the As Is sample.

Among the mesh-based samples, the 105 µm showed no drop in T_g, while 53 µm, coated and full growth samples showed a significant drop. Among the dopamine-based samples, dopamine functionalization after growth, PDA_A sample, showed a drop of 7.3%, while dopamine functionalization before growth, PDA_B sample showed no drop in T_g. This shows that, regardless of lower values of storage modulus, dopamine was more effective in holding the nanorods in place, evident from the delayed shift from a solid to a glassy state of the polymer.

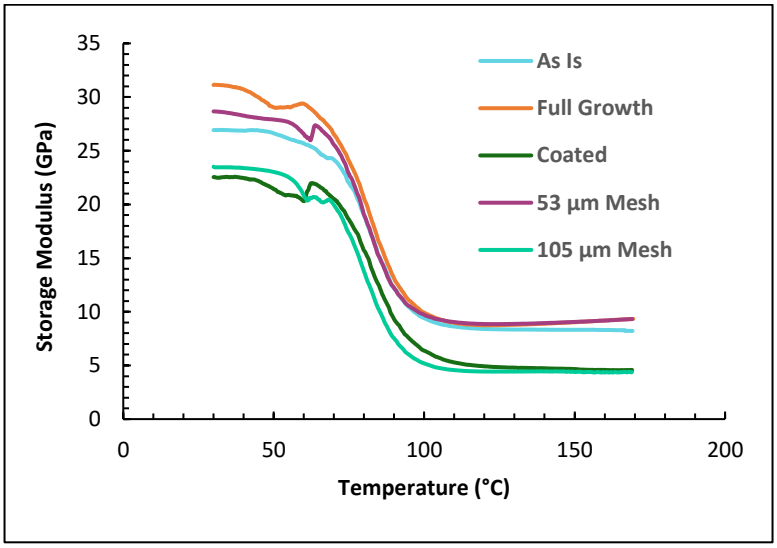

Figure 3.10 Variation of storage modulus with temperature for various mesh-based configurations.

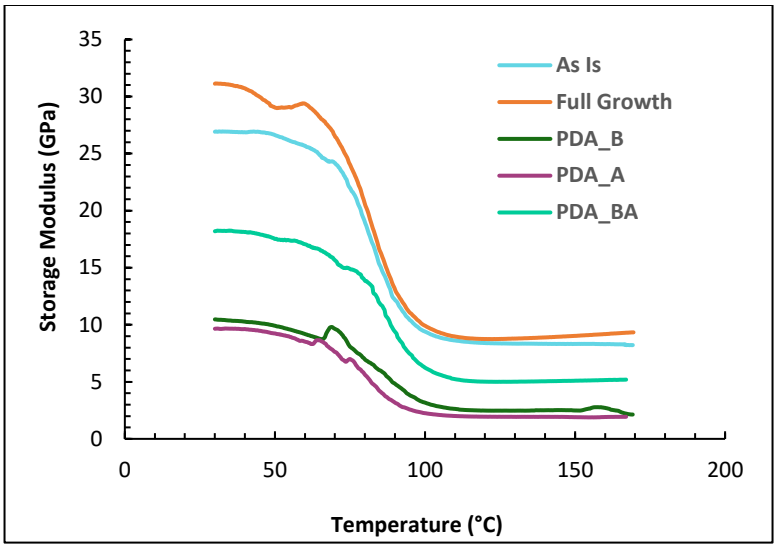

Figure 3.11 Variation of storage modulus with temperature for various dopamine-based configurations.

Table 3.1

Comparison of glass transition temperature for different composites' configurations.

Configuration	T_g from storage modulus (°C)	% Difference compared to reference	T_g from tan (δ) (°C)	% Difference compared to reference
As Is	69	0.00	87	0.00
Full Growth	60	-13.04	88	1.15
PDA_B	69	0.00	92	5.75
PDA_A	64	-7.25	86	-1.15
PDA_BA	74	7.25	91	4.60
Coated	63	-8.70	90	3.45
53 µm Mesh	64	-7.25	86	-1.15
105 µm Mesh	69	0.00	87	0.00

Figures 3.12 and 3.13 show the variation of tan delta (δ), with temperature for mesh-based configurations and dopamine-based configurations. Figure 3.12 shows higher peaks for all configurations, when compared to the As Is sample. However, the patterned 105 µm and 53 µm showed higher peaks, compared to the Full growth and Coated samples. This shows the patterned nanorods aided in

more efficient damping of these hybrid composites. This can be attributed to the interlocking between the epoxy and the carbon fiber provided by uniformly spaced nanorods acting as reinforcements. Figure 3.13 shows higher peaks for all configurations functionalized with PDA, when compared with Full Growth or As Is samples. This shows an evident increase in the adhesion of nanorods to the carbon fiber surface, to act as efficient reinforcements, and hence improving their damping efficiency.

The tan delta (δ) plots in all configurations were seen to rise to a peak and fall, imitating a sine plot. This shift is usually the result of a phase shift in materials. Hence, this peak can also be used to calculate the glass transition temperature, T_g of a given material. The peak values from the plots of various configurations are tabulated in Table 3.1. The PDA_B sample showed the highest increase of 5.8 % in T_g, reiterating the efficiency of dopamine in enhancing the interfacial adhesion between fiber and the matrix.

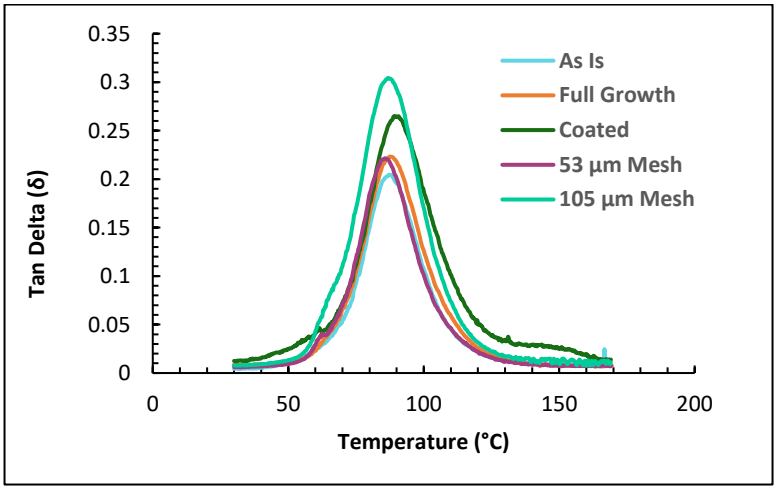

Figure 3.12 Variation of tan delta with temperature for various mesh-based configurations.

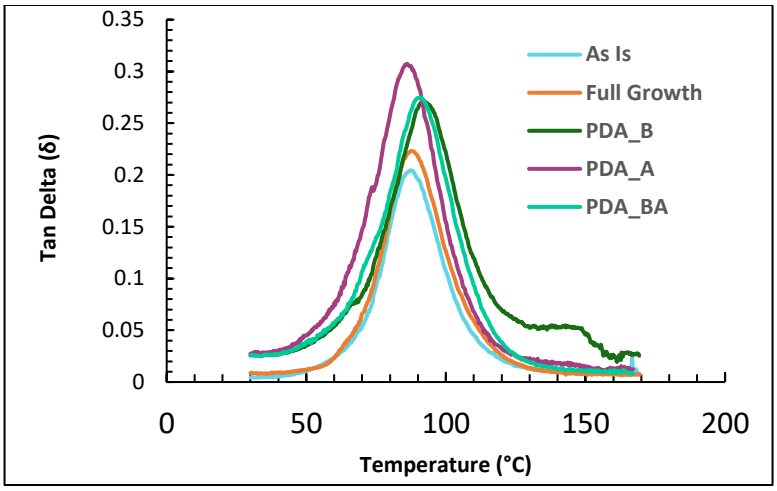

Figure 3.13 Variation of tan delta with temperature for various dopamine-based configurations.

3.3.2.2. Frequency Scan Results

Figures 3.14 to 3.17 show the variation in storage modulus or tan delta (δ) with various frequency values ranging from 1 to 100 Hz for mesh-based configurations and dopamine-based configurations, respectively. A common increasing trend in storage modulus with frequency is seen in all the samples. The slope is higher for the Coated sample, and lower for the PDA_B sample. Regardless of the trend, the variation in the value of storage modulus with the increase in frequency is very minimal. This indicates that frequency does not play a major role in the energy absorption capacity of these hybrid composites. It is worth noting that there are kinks (sudden drops) around 80-97 Hz, indicating a sudden drop in storage modulus. Avoidance of this frequency during operations can help prevent catastrophic failures due to a major phase shift in the material state.

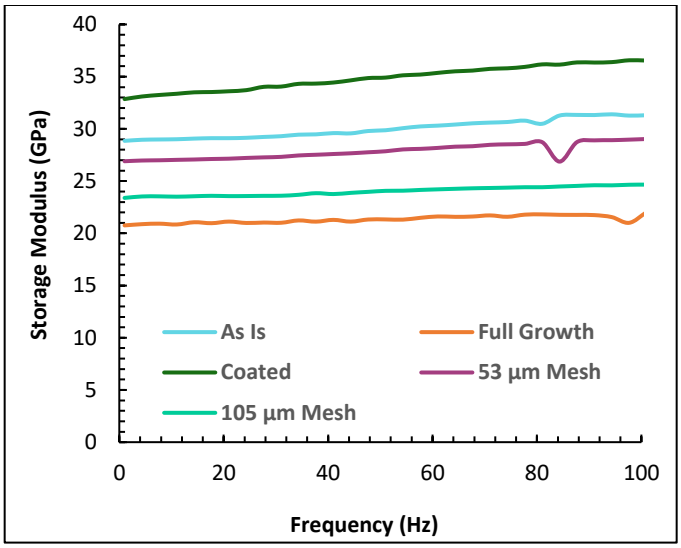

Figure 3.14 Variation of storage modulus with frequency for various mesh-based configurations.

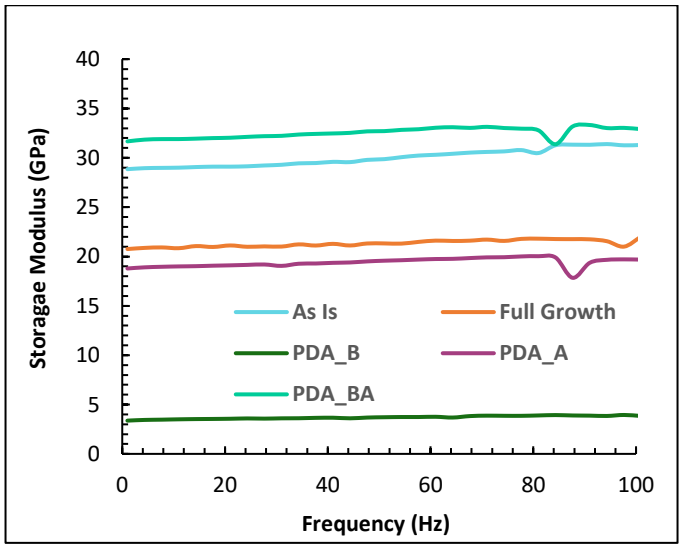

Figure 3.15 Variation of storage modulus with frequency for various dopamine-based configurations.

Figures 3.16 and 3.17 show the variation of tan delta (δ) with frequency for mesh-based configurations and dopamine-based configurations, respectively. These figures show that the value of tan delta (δ) is highly dependent on the frequency. Though a pattern for the occurrence of these peaks is unclear, almost all configurations have seen a peak around 34 Hz.

In Figure 3.16, it is seen that the Coated and Full Growth samples showed higher values of tan delta (δ) when compared to the other configurations. Tan delta is the ratio of energy dissipation to energy absorption. This shows that, the energy dissipation in these samples is better than the energy dissipation in the patterned samples, since the trend for energy absorption was opposite as seen in storage modulus values.

In Figure 3.17, PDA_B sample exhibited very high values of tan delta (δ) compared to all the other configurations. The As Is sample had the lowest values compared to the rest. This shows that the functionalization method using dopamine has increased the surface area for the nanorods adhere better with stronger Van Der Waals forces, and allowed better seepage of epoxy into the fiber, hence rendering these materials less susceptible to vibrations. According to these results, the functionalization of carbon fiber with polydopamine before the growth of ZnO nanorods would the ideal solution, if the purpose is the enhancement of damping properties over a wide range of frequencies.

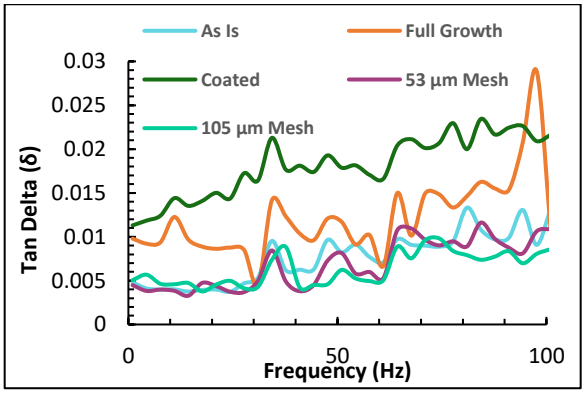

Figure 3.16 Variation of tan delta with frequency for various mesh-based configurations.

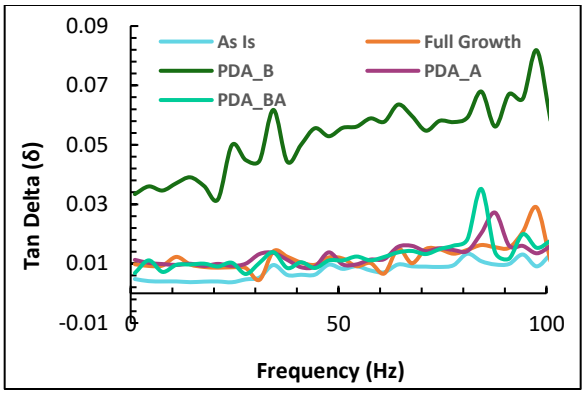

Figure 3.17 Variation of tan delta with frequency for various dopamine-based configurations.

4. Molecular Dynamics Simulation of ZnO Hybrid Composite

To probe the effects of ZnO nanofillers in fiber/epoxy system further, two molecular dynamics (MD) simulation models were built. One model did not have nanofillers in the fiber/epoxy system. The second model had multiple ZnO nanorods in-between the fiber/epoxy system. The procedure for building the simulation model in each case was detailed below.

4.1. Fiber/Epoxy Model

4.1.1. Materials

All MD simulations were carried out using the commercial software Materials Studio software (Biovia-Dassault Systems). There were three main constituents in the MD simulation cell: Bucky paper (mimicking the outer surface of the carbon fiber), resin and hardener. Bucky paper is a sheet of multi-walled carbon nanotubes, held together by Van Der Waals forces. Hexagonal rings of carbon atoms were stacked in the same plane to form a sheet of Bucky paper.

The resin used was diglycidyl ether of bisphenol-A (DGEBA), also known as EPON 828. The structure modeled for EPON 828 is shown in Figure 4.1. The carbon atoms and links are depicted in gray color, while the hydrogen atoms are in white, and the oxygen atoms are in red. The two epoxide groups in red are the reactive sites of DGEBA. Diethylenetriamine (DETA) was used as the hardener. The molecular structure is shown in Figure 4.2. The amine groups are depicted by blue ball and stick bonds. DETA has five amine reaction sites in total. Thus, EPON and DETA could result in various types of cross-linked polymers when

cured at high temperatures.

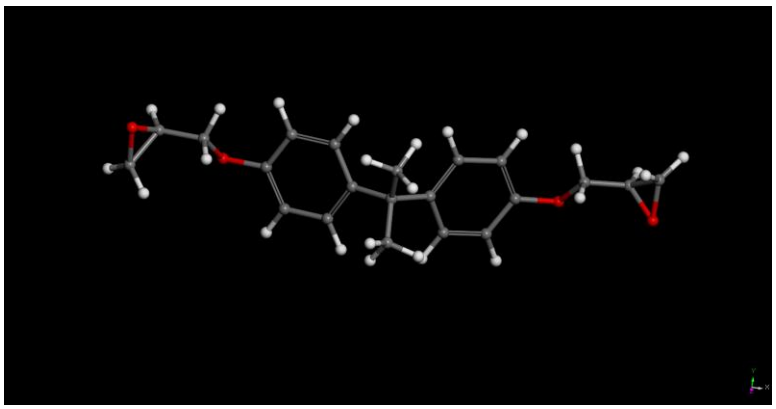

Figure 4.1 Molecular structure of the epoxy resin monomer, EPON 828.

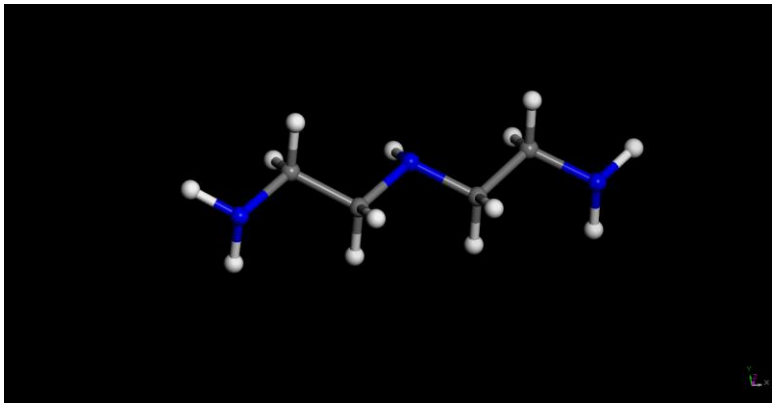

Figure 4.2 Molecular structure of the curing agent, DETA.

Each DETA molecule could ideally react with five EPON molecules to achieve 100 % cross-linking. But this is highly unlikely during an experiment. Some would achieve 20 %, some 60 %, others 80 %. Only few would actually achieve 100 % cross-linking. Hence, for the sake of simulation, uniform cross-linking of 80 % was assumed. This 80 % Cross-linked monomer was shown in Figure 4.3.

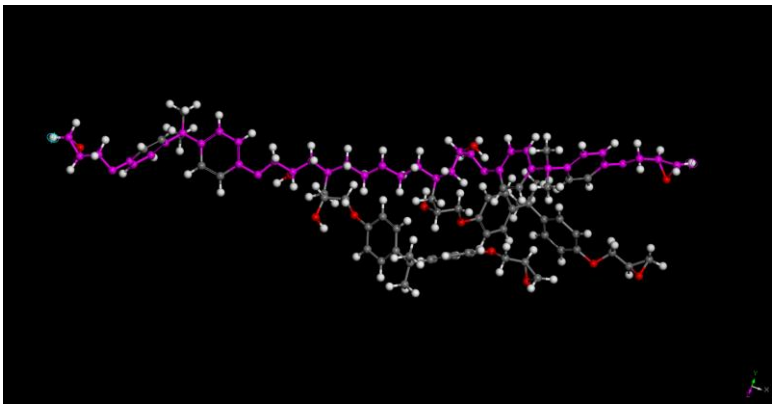

Figure 4.3 Molecular structure reflecting 80 % cross-linking between the EPON and DETA molecules.

4.1.2. Model Design

A homopolymer option was used to build polymers from the monomer molecule of the 80 % cross-linked EPON and DETA structure. With this structure as the repeat unit, two different polymers: one with chain length as 6, and number of chains as 20; second one with chain length 10, and number of chains as 20. The former is shown in Figure 4.4 and the latter is shown in Figure 4.5.

Three Bucky sheets were layered as a single crystal using a constant vacuum separation between each of them. The lattice type of the crystal was 3D triclinic, and the dimensions were $380 \times 250 \times 14$, measured in angstroms (A). This was shown in Figure 4.6. These three entities were then put together as shown in Figure 4.7. This represented the fiber/epoxy system in this current MD model.

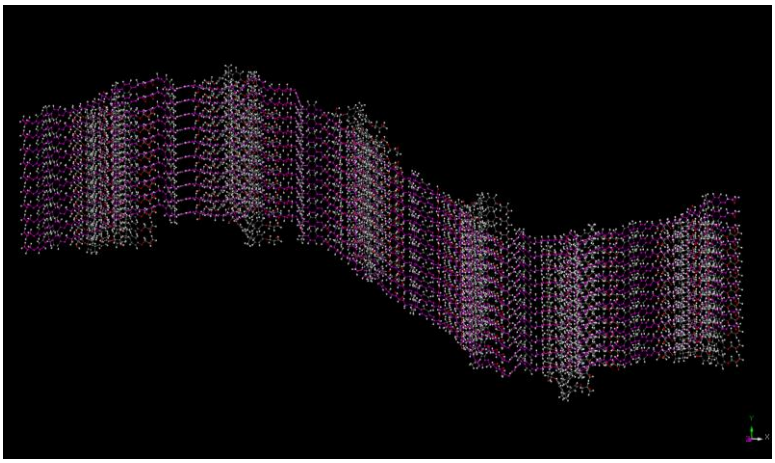

Figure 4.4 Homopolymer with chain length as 6

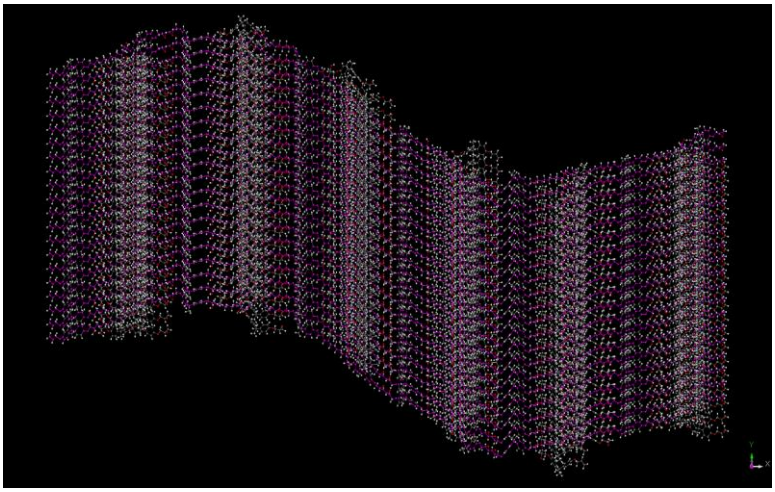

Figure 4.5 Homopolymer with chain length as 10

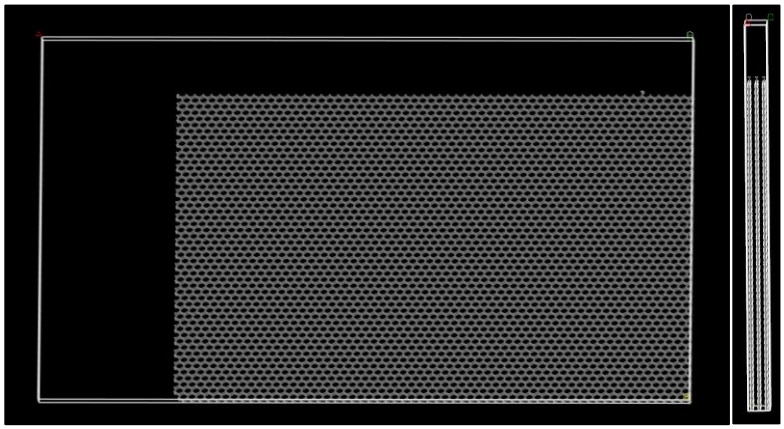

Figure 4.6 Bucky front view and side view

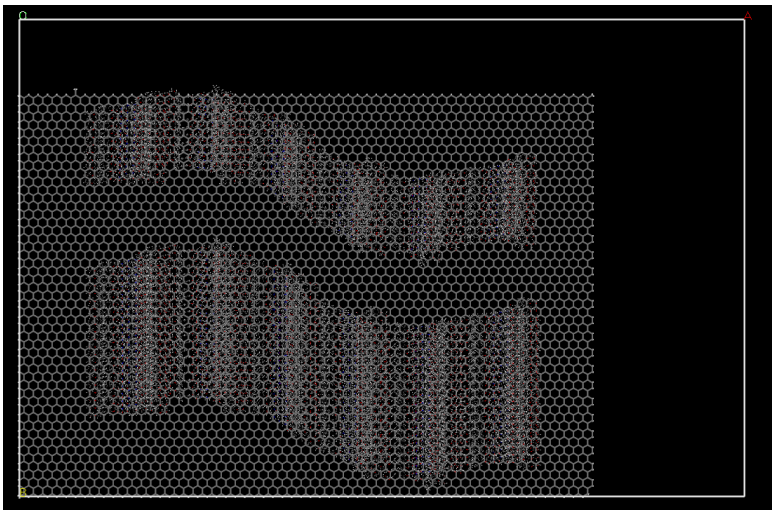

Figure 4.7 Fiber/Epoxy Model

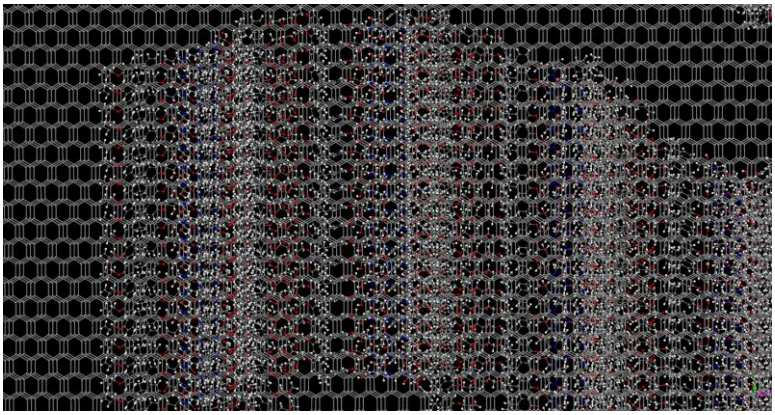

Figure 4.8 Magnified View of the Fiber/Epoxy model

4.1.3. Geometry Optimization

Forcite® molecular mechanics tool in the Material Studio software was used for the investigation of this fiber/epoxy system. After the design, the system of fiber/epoxy was equilibrated to achieve a minimum energy state. Optimization parameters were met using the conjugate gradient algorithm. This method uses the previous iteration to correct for a direction to find the minimum. Hence, it is more efficient than steepest descent methods. The movement of the atoms were defined and controlled by a force field.

Various forcefields like COMPASS, Dreiding, Universal, PCFF and so on differ from each other majorly in the type and accuracy of bonding parameters for a certain set of elements in the periodic table. Within each forcefield, forcefield types can be defined using properties like element type, bond type, number of active sites, charge, hybridization, allowed atomic interactions and so on. These are automatically calculated by the software based on the system under consideration. These can be manually edited if required. Bond terms like angle, torsion and other parameters are calculated based on these forcefield type assignments (Systemes, 2017). In this dissertation, Universal type forcefield was used. This is a purely diagonal and harmonic forcefield with a full coverage of the periodic table. Since this simulation had both organic and inorganic interactions, a general purpose forcefield like Universal was an apt fit.

The initial coordinates of a structure, together with forcefield parameters are used to calculate all the terms in the energy equation. The total potential energy of the system is calculated as follows:

$$E_{total} = E_{valence} + E_{crossterm} + E_{non-bond} \quad (4.1)$$

where $E_{valence}$ denotes the valence interactions in the diagonal terms, which include bond stretching energy, valence angle bending energy, dihedral angle torsional energy, out-of-plane interaction energy terms, and an Urey-Bradley (UB) term which accounts for energy interactions between atom pairs. $E_{crossterm}$ accounts for structural deformations caused by bond or angle distortions when the system is under vibration. $E_{non\text{-}bond}$ accounts for energies due to Van Der Waals forces, electrostatic forces, and hydrogen bonding.

Atom based summation methods, with a cutoff distance of 7 Å was used in

the current model for the calculation of Van Der Waals energy terms. This means that, all the Van Der Waals interactions beyond 7 Å of any atom are ignored. Ewald summation method, with an accuracy of 1×10^{-5} was used for the calculation of electrostatic terms. In general, this method is more accurate in the calculation of non-bond energies but increases the processing time by the factor of $N^{1.5}$, where N is the total number of atoms in the system. This is exclusively designed for periodic systems and crystalline solids.

The Forcite geometry optimization was run with no external pressure, and fine convergence tolerance values for energy, force, stress, and displacement. The maximum number of iterations was set to 40,000. The optimized structure generated after running using 35 cores in parallel was shown in Figure 4.9.

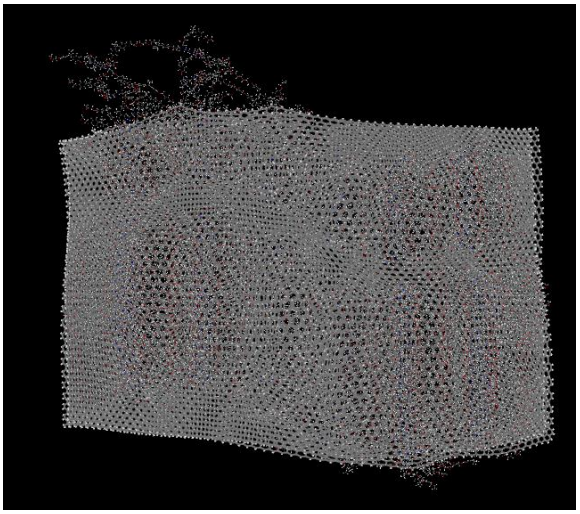

Figure 4.9 Geometrically optimized fiber/epoxy system

4.1.4. Study of Dynamics

This step is used to monitor the system over a period of time. Modified classical equations of motion are used in this step, taking into consideration the

effects of temperature and pressure. The output accounts for the change in atomic configurations and velocities with time, which can be subsequently used to calculate various mechanical properties of the system.

The simplest form for the Newton's equation of motion used of the force calculations is given by:

$$F_i(t) = m_i a_i(t) \quad (4.2)$$

Where F_i denotes the force, m_i denotes the mass, a_i denotes the acceleration of an atom i. These equations are deterministic in nature. This means that, if the initial positions and velocities of a system are given, the position and velocities after a time, t can be calculated.

To account for the changes in the system due to various external factors like temperature and pressure, various methods to calculate equations of motion for isothermal and adiabatic states exist. These include constant energy and volume (NVE) ensemble, constant temperature, and volume (NVT) ensemble, constant pressure and enthalpy (NPH) ensemble, and constant temperature and pressure (NPT) ensemble.

In the current simulation, NVT ensemble was chosen. The system was monitored for a time period of 20 ps at a constant temperature of 298 K. Microscopically, temperature is calculated from the kinetic energy values, which are used to calculate atomic velocities. Maxwell-Boltzmann equation gives a relation between the temperature and the distribution of atomic velocities as shown below:

$$f(v)dv = \left(\frac{m}{2\pi k_B T}\right)^{3/2} \left(e^{\left(-mv^2/2k_B T\right)}\right) 4\pi v^2 dv \quad (4.3)$$

Equation 4.3 gives the probability f(v)dv of molecule of mass m having a velocity between v and $v + dv$ when the system is placed at temperature T, with k_B as th Boltzmann constant. This can be used to derive an equation between average temperature, T and kinetic energy, K as follows:

$$T_{instan} = \frac{2}{k_B N_f} K_{instan} \quad (4.4)$$

Where K_{instan} is the total sum of kinetic energy of the system in x, y and z. To calculate the thermodynamic temperature, T, the time average of all the instantaneous temperatures, T_{instan} will be calculated. Though there are several methods to control the temperature of a system, Nosé-Hoover thermostat was used in the current simulation. The structure obtained after the dynamics run is shown in Figure 4.10.

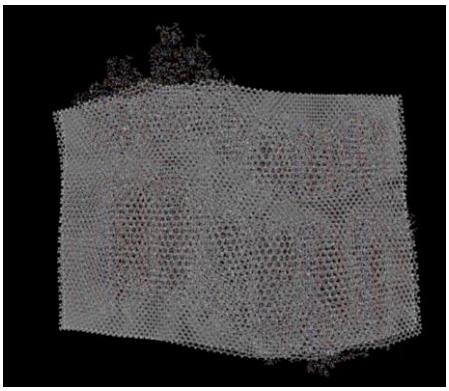

Figure 4.10 Fiber/epoxy system after Dynamics run

4.1.5. Calculation of Mechanical Properties

The output of the dynamics run helps in the calculation of the stiffness and hence, Young's modulus, Poisson ratios, bulk modulus and shear modulus. Molecular dynamics can be used to calculate mechanical properties under two conditions: the system is a canonical ensemble; the system is allowed all internal

degrees of freedom to allow the calculation of second order derivatives. When a system is under a constant temperature, contains fixed number of atoms, with a constant volume, it is called a canonical ensemble. The ensemble built in this work used NVT method while running the dynamics run and was not constrained in any degree of freedom in agreement these two conditions.

To define the strain, the change in the value of position vectors of the ensemble before and after deformation are used. The initial position matrix is given by h_0, and the deformed position matrix is given by h. The strain equation can be written as follows:

$$\varepsilon = \frac{1}{2}\left({h_0}^{-T} G {h_0}^{-1} - I\right) \quad (4.5)$$

Where G is $h^T h$, I is the unit matrix, -T is the transpose of the unit matrix. At any equilibrium state, $\varepsilon = 0$. Hence, $h=h_0$. Strain tensor is symmetric, with six non-zero elements by definition. The stress tensor, σ is associated with the strain tensor, given by the change in free energy A, with respect to strain, at constant number of atoms and temperature. Since strain is symmetric, stress tensor is symmetric too due to this association.

$$\sigma_{o\beta} = \frac{1}{V}\left[\frac{\partial A}{\partial \varepsilon_{o\beta}}\right]_{N,T} \quad (4.6)$$

Where, V is the volume and N is the number of particles. Substituting the free energy equation, the stress tensor for the entire canonical ensemble is given by:

$$\sigma = -\frac{1}{V}\sum_{i=1}^{1} \langle m_i v_i {v_i}^T + \frac{1}{2}\left(r_i {F_i}^T + F_i {r_i}^T\right)\rangle \quad (4.7)$$

Where m_i, v_i, r_i, F_i stands for mass, velocity, position, and force of a particle i. The <…> brackets indicate that this value of stress is summed for the entire

ensemble. These equations of stress and strain are further used to calculate the elastic stiffness tensor for both adiabatic and isothermal situations. This elastic stiffness tensor has 81 components. However, due to the symmetry constraints of stress and strain tensors, the equations are simplified and expressed using Voigt notation as follows:

$$\sigma_i = C_{ij}\varepsilon_j \quad (4.8)$$

Where C is the Voigt matrix representation of the elastic stiffness tensor. Other elasticity constants are calculated using this data, based on their degree of anisotropy: isotropic; orthotropic; or anisotropic.

There are static and dynamic methods available for the calculation of mechanical properties in the current software. The former does not consider the effects of temperature, while the latter does. Due to computational limitations, static methods were employed in this dissertation.

The constant strain method applies multiple finite strains, below a maximum strain value to the entire canonical ensemble in a series of steps (M. Al-Haik, 2014). In this work, the total number of strains were 4, and the maximum strain applied to the structure was 8.0×10^{-3}. The 6×6 strain pattern with all 1s in the diagonal, 0s in the other cells was automatically generated based on the structure of the ensemble. This means that there is non-zero strain in xx, yy, zz, yz, zx and xy directions. The energy parameters were similar to the ones used during geometry optimization. After running the mechanical calculations using this setup, the Figure 4.11 was generated, and various elasticity parameters were tabulated.

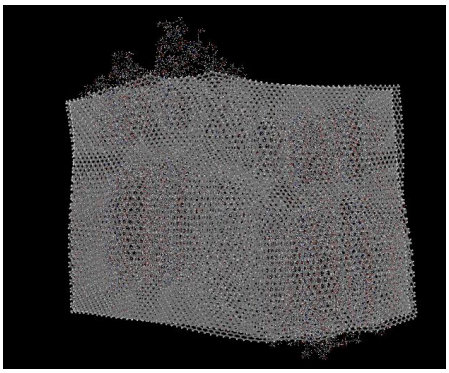

Figure 4.11 Fiber/Epoxy system after mechanical analysis

4.2. Fiber/Epoxy/ZnO Hybrid Model

There was a simple design addition to this model. A nanocluster shown in Figure 4.12 was built from a single ZnO molecule. Multiple nanoclusters were added to the fiber/epoxy system as shown in Figure 4.13. Similar steps for geometry optimization, dynamics and mechanical runs were implemented as outlined in Section 4.1. The output from each run is shown from Figure 4.15 to Figure 4.17.

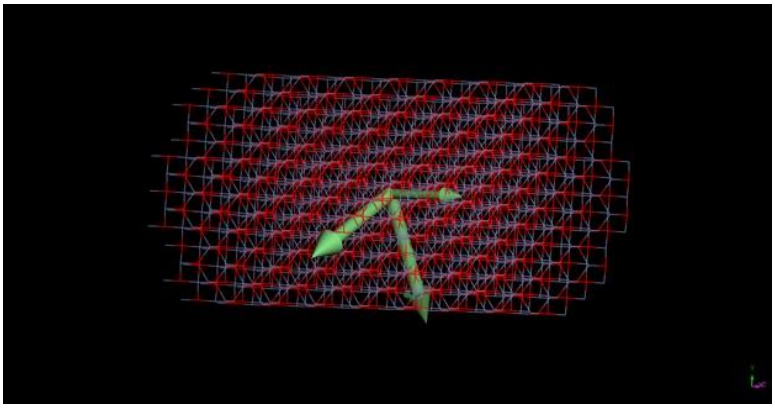

Figure 4.12 Nanocluster of ZnO

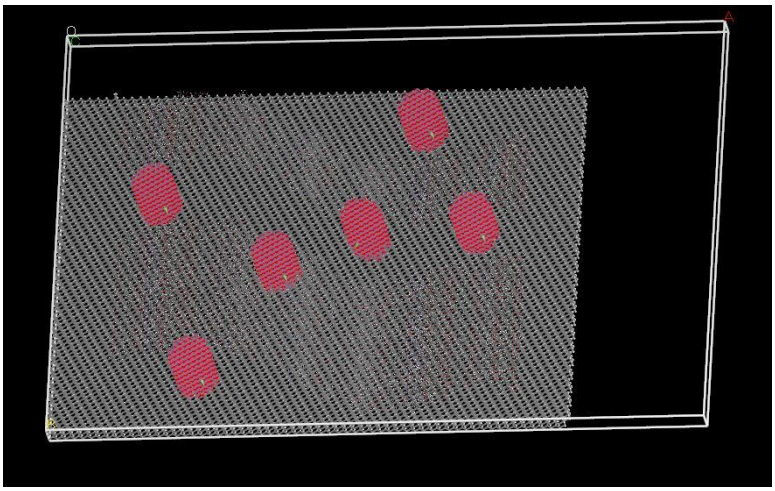

Figure 4.13 Fiber/epoxy/ZnO Hybrid model

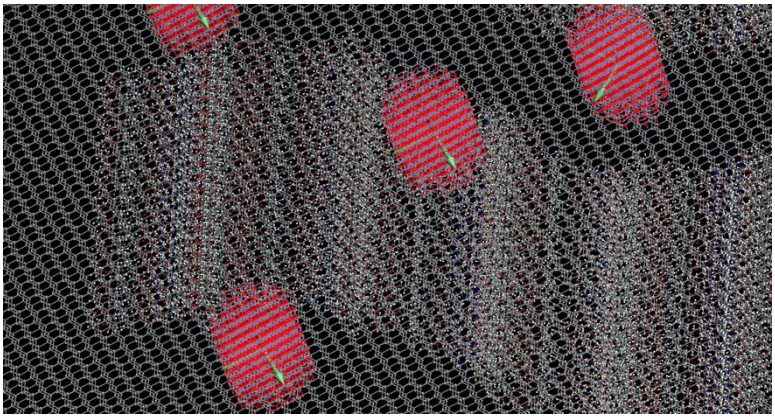

Figure 4.14 Magnified view of fiber, epoxy and ZnO interactions

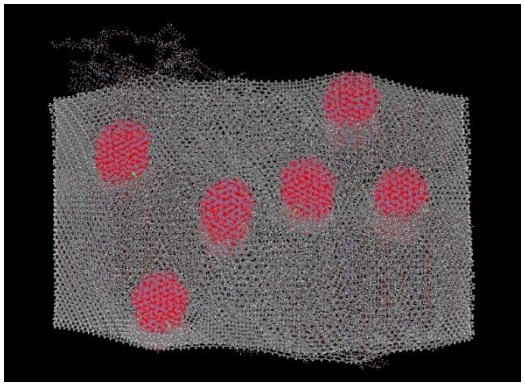

Figure 4.15 Hybrid model after geometry optimization

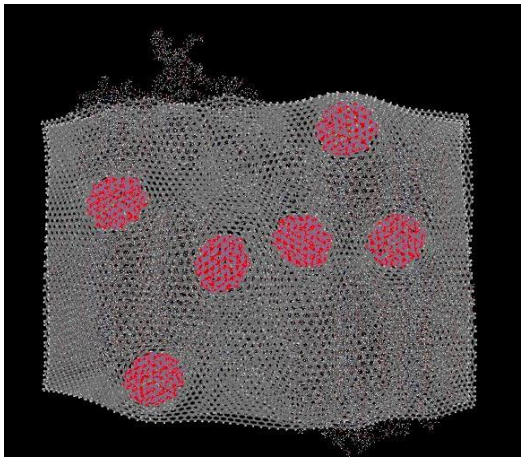

Figure 4.16 Hybrid model after dyamics run

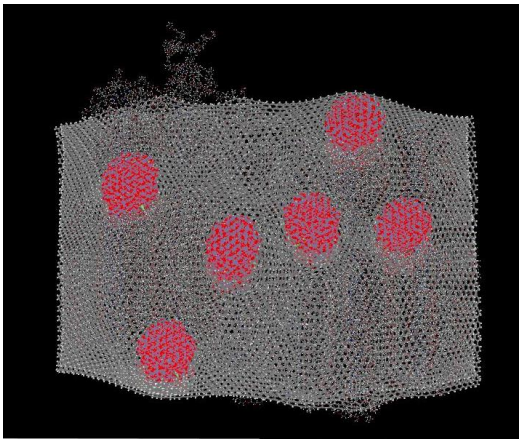

Figure 4.17 Hybrid model after mechanical analysis

4.3. Results and Discussion

4.3.1. Geometry Optimization and Dynamics Run

Geometry optimization described in Section 4.1.3 brings the canonical ensemble to a state of minimum energy. This is represented by the change in enthalpy with each optimization step. Enthalpy is defined as $H = E + PV$, where E is the internal energy of a given system, P is the pressure, and V is the volume. Figure 4.18 shows the evolution of enthalpy with the evolution of each optimization step. The sample with ZnO nanorods had higher initial enthalpy due

to larger number of atoms, leading to larger valence bond, angle, and torsional energies; non-bond energies; and Van Der Walls interactions, resulting in higher internal energies. Both No ZnO and With ZnO ensembles had a significant drop in the enthalpy values during geometry optimization, suggesting that the conjugate gradient method, and Universal force field were suitable for both these systems.

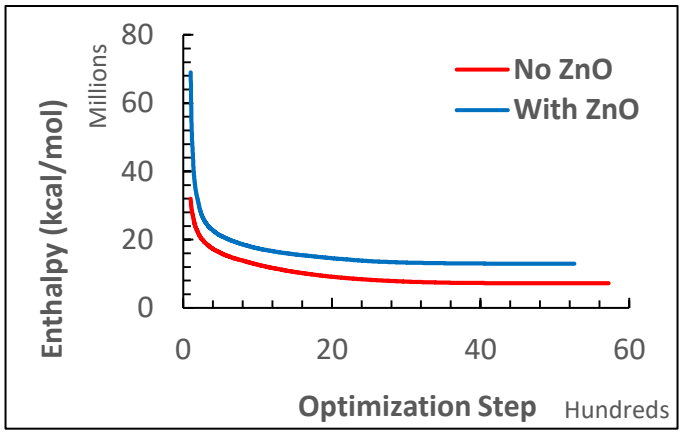

Figure 4.18 Enthalpy vs. Optimization step during Geometric Optimization.

Figures 4.19 to 4.22 show the evolution of energies like potential, kinetic, non-bond, and their total sum with time during the dynamic run. Before the dynamics run, all MD ensembles are at 0 K by default. To heat to the set temperature of 298 K, all the atoms are vibrated to higher velocities. This increases and fluctuates the kinetic energy values. As discussed in Section 4.1.4, the temperature values are directly correlated with kinetic energy calculations. This can be clearly seen from comparing Figure 4.20 and Figure 4.23. Once the set temperature is reached, the oscillations in kinetic energy damp down with time, as seen in Figure 4.20. Other energy parameters like potential energy, non-bond energy and total energy show a slow decay with time in both

configurations, as seen in Figure 4.19, Figure 4.21, and Figure 4.22 respectively. The energy values for With ZnO ensemble were always higher than No ZnO ensemble as evident in all the figures.

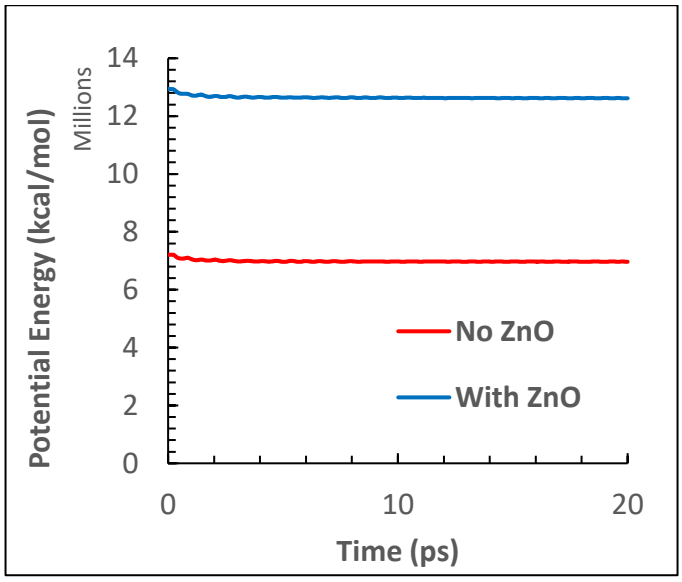

Figure 4.19 Potential energy vs. Time during MD dynamics step.

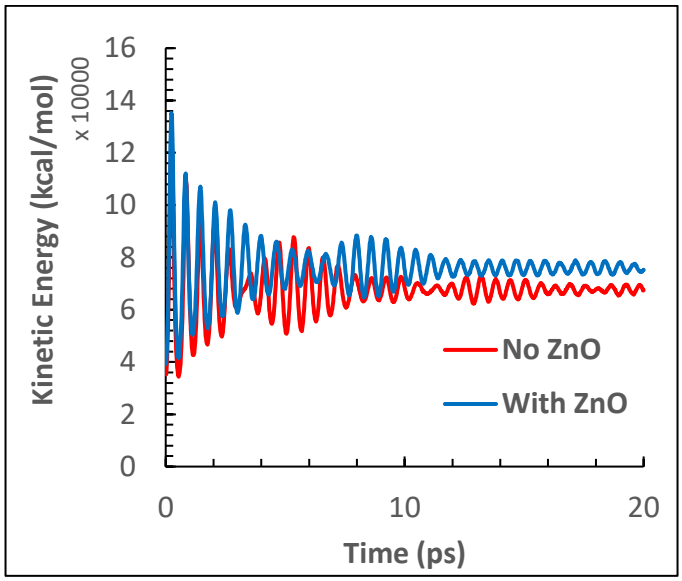

Figure 4.20 Kinetic energy vs. Time during MD dynamics step.

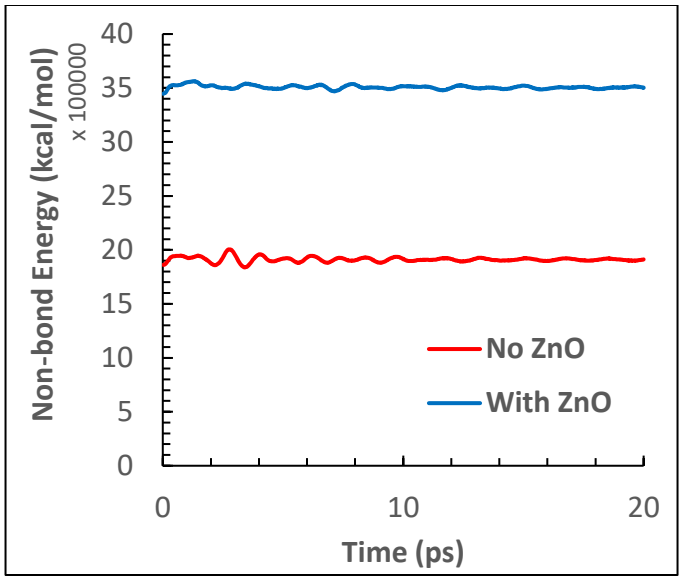

Figure 4.21 Non-bond energy vs. Time during MD dynamics step.

Figure 4.23 shows the temperature evolution of both ensembles with time. It is worth noting damping behavior of the With ZnO ensemble is slightly better than No ZnO ensemble. This behavior adds credit to the concept of ZnO nanorods acting as reinforcements in a hybrid polymer composite. Though the experiment in Chapter 3 proved this theory in macroscopic scale, this damping behavior shows proof of this concept even at an atomic scale.

Densities remained constant at 0.628 and 1.108 g/cm^3, for No ZnO and With ZnO ensembles respectively. This is because of NVT settings during the dynamics run. The mass and volume were unchanged due to the constant number of atoms, and constant volume periodic conditions.

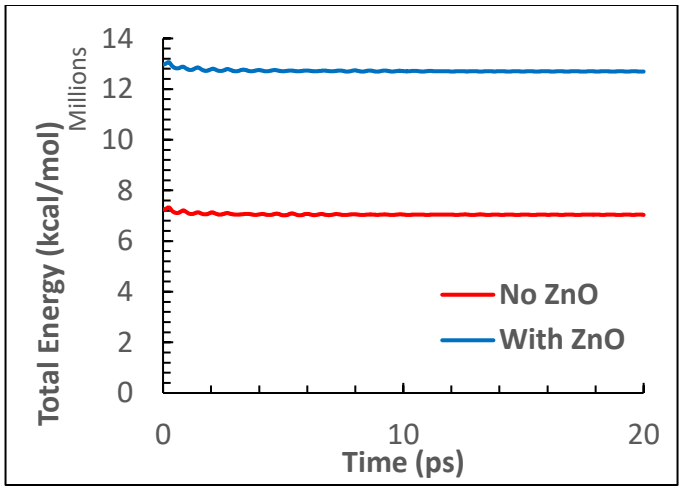

Figure 4.22 Total energy vs. Time during MD dynamics step.

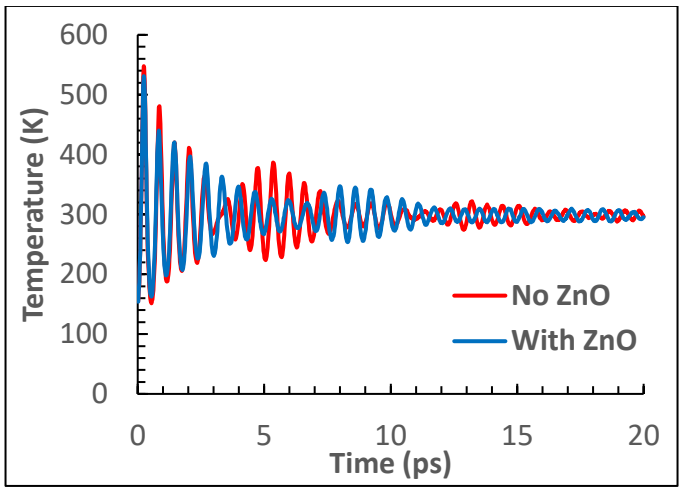

Figure 4.23 Temperature vs. Time during MD dynamics step.

4.3.2. Mechanical Properties

The values of various mechanical parameters for both ensembles are presented in Table 4.1 and Figure 4.24. The values of elastic constants are considerably higher in the ensemble with ZnO nanorods when compared to the one with no nanorods, as seen in Table 4.1. These results suggest that the nanorods improve the stiffness of the fiber/epoxy system, hence enhancing its overall strength.

Table 4.1

Elastic stiffness constant values after mechanical analysis.

Elastic Stiffness Constants	No ZnO	With ZnO	% Change
C_{xx}	292.13	394.25	34.96
C_{yy}	83.22	77.02	-7.45
C_{zz}	192.32	233.52	21.42
C_{yz}	91.20	114.06	25.07
C_{zx}	51.68	64.62	25.04
C_{xy}	53.96	62.22	15.31

The results in Figure 4.24 show that, the nanorods play a major role in enhancing the compressive and shear properties of composites. This is due to higher values of bulk modulus and shear modulus for the ensemble with ZnO nanorods. It is challenging to test a composite for compression and shear using experiments. All the experiments performed in Chapter 3 proved the significance of ZnO nanorods in tensile or bending fixtures. The calculation of all the elements in stiffness matrix using molecular dynamics makes it easier to theoretically predict the bulk modulus and shear modulus. These results in molecular dynamics strongly reinforce that the ZnO nanorods could cause significant improvement in tensile, compressive, and shear strength of a composite.

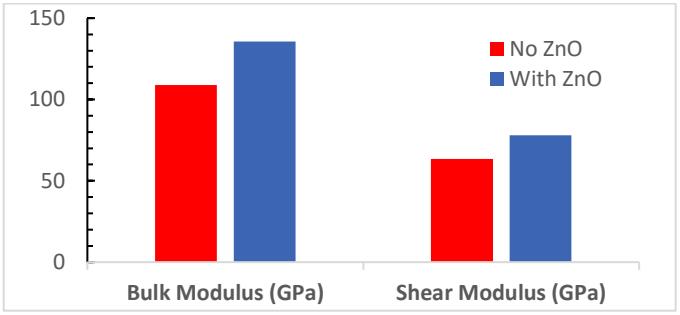

Figure 4.24 Comparison of Bulk and Shear modulus for both ensembles.

5. Experiment with CNTs Based Surface Modifications

In this chapter, all the experiments and results pertaining to hybrid composites fabricated by modifying carbon fiber surface using CNTs were discussed. Various composite configurations, fabrication techniques and testing procedures involved were discussed in detail.

5.1. Composite Configurations and Fabrication

Four composite configurations were fabricated: One with uniform growth of CNTs as a result of performing the GSD growth on a sample pre-sputtered with uniform catalyst film; second sample with catalyst patterned with a polyester mesh opening of 105 μm on carbon fabric; third with catalyst patterned with a polyester mesh opening of 53 μm on carbon fabric; fourth, a de-sized carbon fabric as a reference sample. Each composite comprised a two-plies adhered by an epoxy matrix. The goal of this investigation is to probe the effects of growing CNTs into different topological patterns on the composites' rheological properties including the glass transition temperature and damping. The investigation also characterizes the elastic (tensile) and viscoelastic (load relaxation) performances of composites with different CNTs topologies.

PAN-based carbon fibers with 3k bundles from Thornel® T650 (Solvey, Inc.) were utilized as the reinforcement throughout this investigation. The sizing on the fibers was removed by placing the as received sized fibers in a tube furnace at 550 °C for 30 mins under an inert environment (nitrogen).

The CNTs growth process was performed following the graphitic structures by design (GSD) protocol. The GSD synthesis technique requires the pre-

deposition of a catalyst metal (i.e., nickel in this study) on the surface of the carbon fibers. The CNTs growth initiates at the areas where the catalyst material is pre-deposited. For growing uniform CNT forests over the carbon fiber fabrics, a uniform layer of nickel was deposited. An ATC Orion (AJA international Inc.) high vacuum sputtering system was utilized to deposit a 2 nm thick layer of nickel on both sides of the square carbon fabric samples under 3 millitorr pressure of argon gas where 200 W of power was supplied to the sputtering target. To achieve a checkerboard patterned CNTs forests over the carbon fiber fabrics, two perforated polyester mesh templates (Components Supply Co.) with mesh openings of 105 and 53 μm, thread diameters of 70 and 31 μm, and open area percentages of 33 % and 40 %, respectively.

The GSD-CNTs growth process was carried out inside a quartz tube reactor equipped with a thermal controller and three-input gas mass flow controllers. The process starts with a reduction step, under an H_2/N_2 gas mixture atmosphere at 550 °C for 2 h. Then, the process is followed by the flushing step in which the tube reactor is flushed with N_2 gas to get rid of any residuals of the previous step. Subsequently, the CNTs growth step begins, maintaining the constant temperature at 550 °C for 1 h under a $C_2H_4/H_2/N_2$ environment.

The three different CNT based configurations were visually inspected using scanning electron microscopy. The micrographs for CNTs grown using 53 μm mesh, 105 μm mesh and no mesh are shown in Figure 5.1, Figure 5.2, and Figure 5.3 respectively.

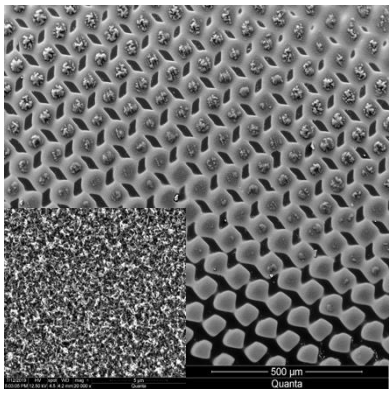

Figure 5.1 Islands of CNTs grown after nickel catalyst was sputtered through 53 µm mesh. Inset figure shows uniform CNTs constituting these islands.

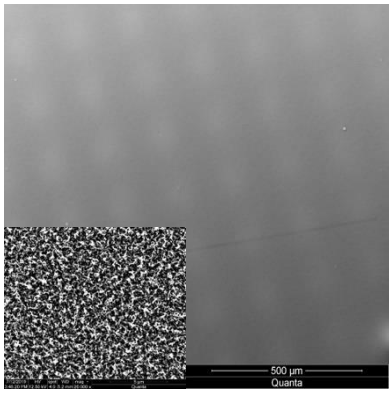

Figure 5.2 Islands of CNTs grown after nickel catalyst was sputtered through 105 µm mesh. Inset figure shows uniform CNTs constituting these islands.

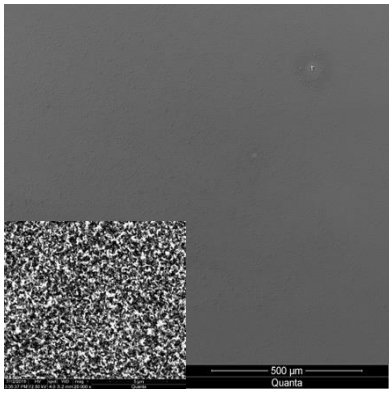

Figure 5.3 CNTs grown after nickel catalyst was sputtered with no mesh. Inset figure shows uniform CNTs constituting this layer of CNTs.

Each composite in this experiment comprised a two-ply adhered by an epoxy

matrix; Aeropoxy™ (PTM&W Industries, Inc.; Santa Fe Springs, CA, USA). This epoxy is a mixture of PR2032, a Bisphenol-based resin, and PH3660, a hardener. This resin is specially designed for structural production applications with a medium viscosity of 1650 cPs at room temperature. It aids the lamination process and easily wets out carbon, aramid fibers and fiberglass. The hardener has a lower viscosity of 190-200 cPs at room temperature. When both the resin and hardener are mixed in the ratio of 100:27 by weight, a viscosity of 800-875cPs and a glass transition temperature of 91 °C are reported by the manufacturer. Hand-layup method was used for lamination. Following the lay-up of the two plies impregnated with epoxy, it was sealed in a vacuum bag. The four composite configurations laminates were processed using a composite autoclave (Econoclave, ASC Process Systems). A pressure of 70 psi and a vacuum of 25 torr were maintained in the chamber throughout the curing process. The autoclave cycle had multiple steps: Isothermal state for 1 h at 30 °C; heating to 93 °C; isothermal state for 2 h at 93 °C; then cooling down to room temperature.

5.2. Mechanical Testing

5.2.1. Stiffness and Strength

In this work, tensile tests were carried out according to the ASTM D3039 standard (1995). The tensile coupons were cut into 12.7 cm x 1.27 cm and sandwiched between G-10 glass fiber tabs using the same epoxy blend. Tensile testing was performed using MTS Criterion™ Model 43 machine. Strain was measured using a 25.4 mm gauge length extensometer, connected to the MTS controller for real-time data acquisition. These coupons were then mounted in-

between the crosshead grips to be pulled until failure, at the rate of 1.0 mm/min. Each configuration had a minimum of eight tensile coupons. The test data was then averaged for final results.

5.2.2. Damping Properties

A separate batch of specimens was prepared for DMTA. A Discovery Hybrid Rheometer (DHR) with DMTA capabilities (TA Instruments®, Co.) was utilized. The DMTA tests were carried out following the ASTM D7028-07 and ASTM D5023-15 standards (2015; 2015). To ensure that the applied loads/strains are within the elastic range, the linear viscoelastic range of the different composite configurations was determined initially. Composite coupons of size (50.00 mm × 6.25 mm) were cut. Three-point bending fixture with span of 40 mm was used to mount each of the composite samples. In the temperature sweep mode of the DMA, constant frequencies of 0.1, 1.0, 5.0 and 10.0 Hz were applied, while varying the temperature from 22 to 140 °C at a constant strain of 0.05 %. The frequency sweep test was performed with a frequency range from 1 to 80 Hz scanning at room temperature using the same strain applied in the temperature sweep test.

The DHR system was also utilized to conduct flexural load relaxation tests. Based on the linear range of viscoelastic response, a constant stress level of 15, 30, 45 and 60 MPa were applied to all the FRP samples for creep test and relative strain to relaxation tests. Flexural load relaxation tests entail loading the sample till reaching the desired stress level then maintaining the corresponding strain constant for 30 minutes. The sample then was allowed to recover for 15 minutes

before loading it to the next stress level. For each composite configuration, load relaxation tests were performed under 25 °C, 50 °C and finally 75 °C thermal environments. The relaxation tests were carried out up to 75 °C where it is still below the neat epoxy's reported glass transition (~93 °C) so that unexpected rheological behavior can be evaded.

5.2.3. Fracture Analysis

The morphologies of the carbon fibers with different surface treatments were characterized using scanning electron microscopy (SEM, FEI Quanta 650, Thermo Fisher Scientific Co.).

5.3. Results and Discussion

5.3.1. Tensile Test Results

Figure 5.4 shows representative stress-strain curves for the different composites configurations based on the desized (reference) carbon fiber, fibers with uniform growth of MWCNTs and fibers based on the two patterned growths: 53-Pattern and 105-Pattern. All the samples exhibited linear-elastic behavior up to the point of failure. The strength and modulus for the different composites were averaged for a minimum of 5 samples for each configuration, the results are shown in Figure 5.5 and Figure 5.6. A noticeable observation is that growing CNTs uniformly yielded a minute increase in the strength ~3 % compared to the composites based on de-sized fibers. The dense growth of the MWCNTs could have limited the impregnation (wetting) of the epoxy into this dense CNT layer to reach the base carbon fiber which is crucial for improving the mechanical properties.

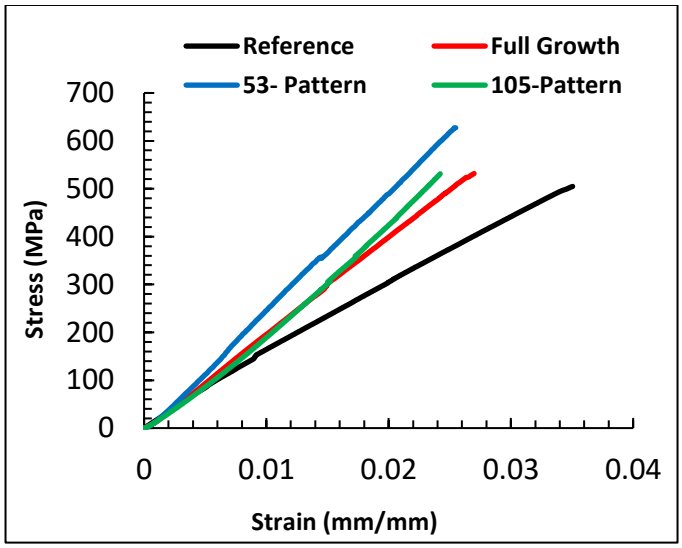

Figure 5.4 Representative tensile tests of the different configurations.

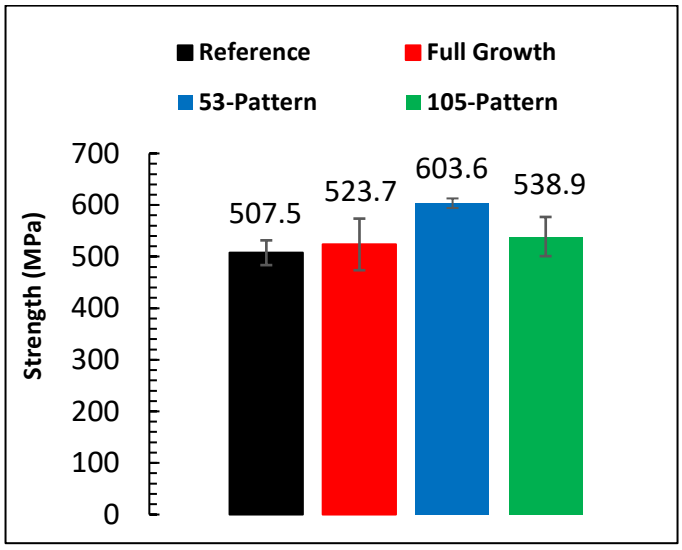

Figure 5.5 The averaged tensile strength of the different configurations.

On the other hand, utilizing coarse (105 μm) and fine (53 μm) patterns assisted in resolving the issue of epoxy impregnation. The spacing in-between the MWCNTs patches- depicted by Figure 5.1 and Figure 5.2 allowed for forming an interlocking mechanism between the MWCNTs, carbon fiber and epoxy. Such mechanism assisted in improving the strength by 19 % for the fine, and by 6 % for the coarse patterns, respectively. It is worth pointing out that,

composites based on T650 carbon fibers with surface grown CNTs using CVD were attempted by another group (Zhang et al., 2009). However, it was reported that for the unsized T650 with uniform growth of CNT (grown at 750 °C), the tensile strength and modulus were identical to the composite based on desized fibers, i.e., the growth of CNTs did not induce neither improvements nor deterioration on the composite's strength.

These results agree with the current findings, for the case of composite with uniform growth of CNTs. Also, the 3 % improvement on the strength can be attributed in part for utilizing relatively lower temperature in the GSD (550 °C compared to 750 °C in CVD). Thus, one can conclude that the significant improvements encountered are mainly attributed to the patterned growth, especially for the case of fine pattern of 53 μm.

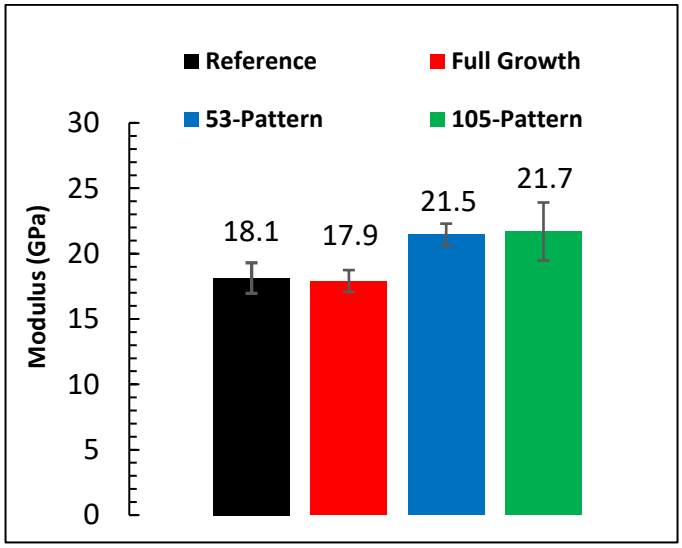

Figure 5.6 The average axial modulus of the different configurations.

The improvements achieved by the patterned growth were also accompanied by enhancement on the modulus; roughly by 18.7 % for both patterned growths.

In other words, stronger and stiffer bonding at the matrix/fiber interface leads to a higher elastic modulus. Finally, Figure 5.4 suggests that the improvements of the strength and modulus gained by the patterned growth of CNTs come at the expense of reduced ductility evident by the reduced strain to failure.

5.3.2. Dynamic Mechanical Analysis (DMA) Results

The viscoelastic properties (storage modulus and tan (δ)) of the four different composites configurations from the temperature sweep at a frequency range of 0.1-10 Hz are plotted in Figure 5.7 to Figure 5.10. The glass transition temperature, T_g, can be found from either the first inflection point of the storage modulus curve or the peak of tan (δ) curve. The estimate for the glass transition temperature using the two methods is tabulated in Table 5.1.

As seen from Table 5.1, there are noticeable differences between the T_g values calculated from tan (δ) peaks vis-a-vis those calculated from the storage modulus inflection. It was reported that a difference margin of around 25 °C can be expected between these two methods (Goertzen & Kessler, 2007). Another observation is that higher frequency yielded higher glass transition. The slight shift of the storage modulus curves to the right as the frequency increases suggests that the glass transition depends on the frequency (Chartoff et al., 2009). Glassy to rubbery transitions shift to higher temperatures at higher frequencies. The shift to higher temperatures is a direct consequence of time-temperature equivalence. As the frequency is increased, the time allowed for molecular motion is decreased, increasing the possibility of shorter timescale motions. Hence, the polymer responds more as if it were at a lower temperature than a

sample run at a lower frequency but the same temperature. Consequently, higher temperatures are required for a sample to achieve an equivalent mechanical state at higher frequencies, and the transitions shift to higher temperatures.

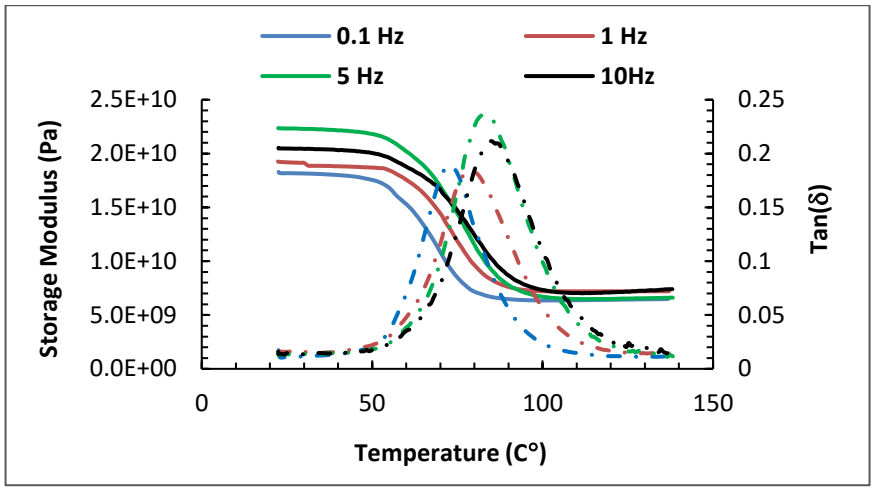

Figure 5.7 DMA temperature sweep for composites based on Reference fibers.

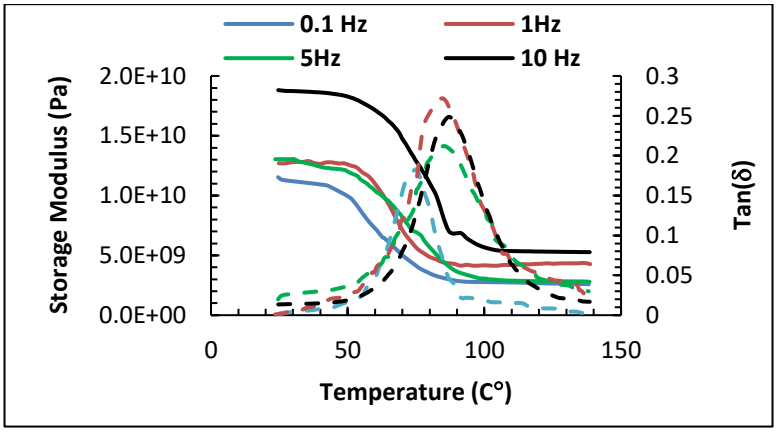

Figure 5.8 DMA temperature sweep for composites based on uniform growth fibers.

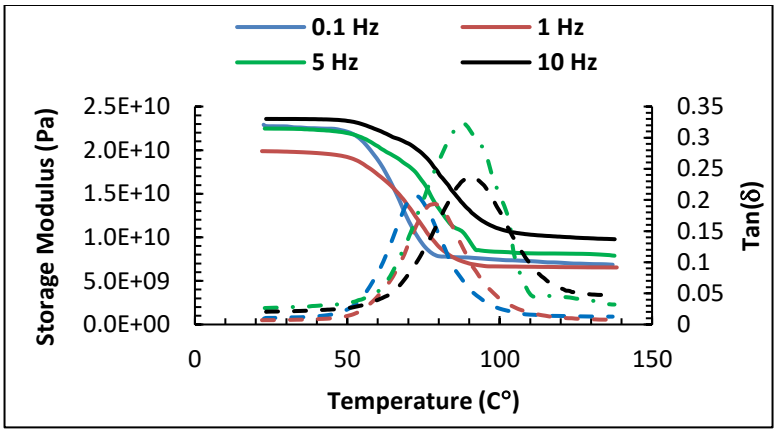

Figure 5.9 DMA temperature sweep for composites based on 53 μm patterned growth fibers.

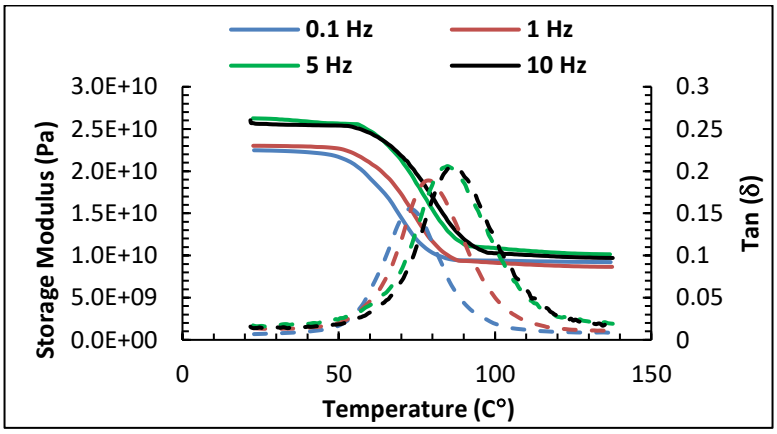

Figure 5.10 DMA temperature sweep for composites based on 105 μm patterned growth fibers.

Regardless of the method of calculation, among the different composite configurations, the 53 μm patterned composite achieved the highest value for T_g; the change was as high as 13.15 % compared to the reference composite at 10 Hz. Similar trend, but to lesser extent was observed for the 105 μm patterned composite. During glass transition, the polymer molecular segments absorb heating energy and begin to move. However, the entrapment of the epoxy in between the CNTs patches diminishes some of the otherwise available space that would allow the molecular movement, thus, more energy (and higher

temperature) is needed to go around these hurdles. Interestingly, the full growth composite showed mixed results; increase of T_g using the tan (δ) analysis and a decrease was observed from the storage modulus curves.

Table 5.1

Comparison of glass transition temperature for different composites' configurations.

Configuration	Frequency (Hz)	**T_g from storage modulus** (°C)	**% Difference compared to reference**	**T_g from tan (δ)** (°C)	**% Difference compared to reference**
Reference	0.1	71	0.00	73	0.00
	1.0	74	0.00	79	0.00
	5.0	75	0.00	82	0.00
	10.0	76	0.00	85	0.00
Full Growth	0.1	66	-7.00	77	5.47
	1.0	72	-2.70	84	6.33
	5.0	74	-1.30	85	3.65
	10.0	76	0.00	87	2.35
105-micron Pattern	0.1	72	1.40	73	0.00
	1.0	73	1.35	84	6.33
	5.0	81	8.00	85	3.66
	10.0	84	10.50	88	3.53
53-micron Pattern	0.1	72	1.40	75	2.73
	1.0	75	1.35	83	1.21
	5.0	82	9.33	88	7.31
	10.0	86	13.15	92	8.23

Based on the loss tangent and the storage modulus measurements, Figure 5.11, the growth of MWCNTs on the surface of the carbon fiber fabric promoted the mechanisms by which the composite dissipates energy leading to higher values of tan (δ) over the frequency spectra. In particular, the 53 μm patterned composite exhibited an increase in the loss tangent over the reference composite of about 46 % at 20 Hz and 26 % at 40 Hz, respectively. While the loss tangent values are low, they agree with reported room temperature loss tangent values for

carbon fiber composites; less than 0.1 in flexure mode DMA (Goertzen & Kessler, 2007). Although, the loss tangent exhibits nonlinear frequency dependent behavior, same frequency dependent pattern is observed for all composite's configurations.

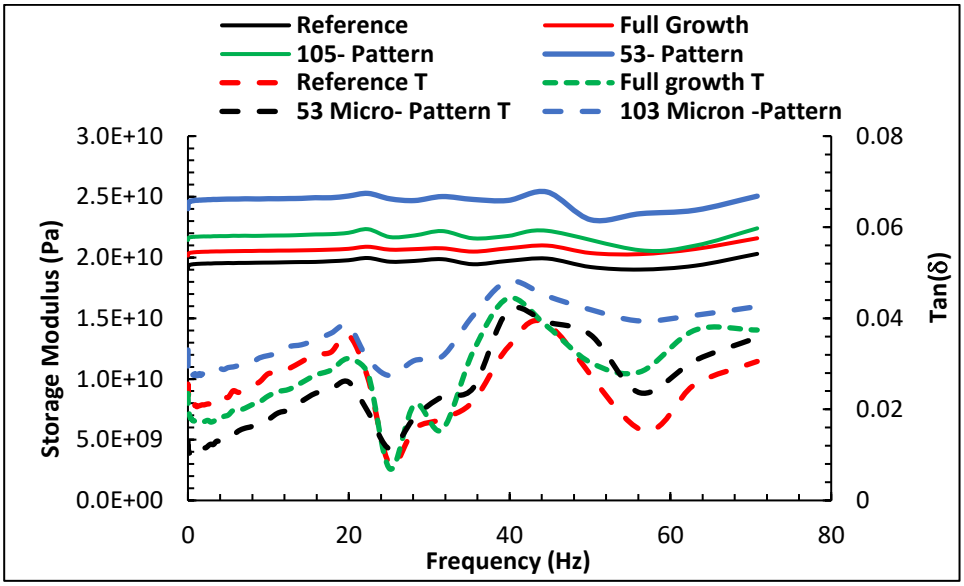

Figure 5.11 The DMA measurements of the storage modulus and tan (δ) for the different composite's configurations via frequency sweep at 30 °C.

The applied strain level (0.05 %) is too small to activate all the mechanisms of energy dissipation via viscoplastic deformation at the CNT/epoxy interface (Koratkar et al., 2005; Suhr et al., 2005), yet the loss tangent of the hybrid composite has noticeably increased. Inducing a patterned growth promoted further increase in tan (δ). Hence, that partial activation of frictional sliding of CNTs/polymer along with the interlocking effect on the interface region are the two possible leading mechanisms responsible for the higher loss modulus of the hybrid composites. The interface is the sole source of difference in energy dissipation in the reference composite configuration.

Figure 5.11 also indicates that the measured storage modulus for all composite samples exhibited a frequency-independent behavior for most of the frequency spectra. In theory the storage moduli should be frequency-dependent for a viscous fluid or a viscoelastic material (Menard, 2008). As the composite becomes more elastic (when adding elastic fillers such as on carbon fibers CNTs), the viscoelastic (time-dependent) behavior diminishes, and the frequency- dependence of the storage modulus is vanished. Such observation was reported for carbon fiber composites with different fibers orientation (Melo & Radford, 2005) within a range of frequencies. The results for the storage moduli of different specimens, Figure 5.11 are qualitatively on agreement with those obtained for the modulus from the tensile tests.

Figures 5.12 to 5.14 show the stress relaxation at each stress level for the composites' configurations. Stress relaxation tests were carried out at four different (strain levels) levels at each temperature. The values of the strain were chosen to correspond to the stress values 15, 30, 45 and 60 MPa, under 25, 50 and 75 °C, respectively. The amount of the stress reduction can be considered, in lieu of the creep strain rate, as a measure of the viscoelasticity; the larger the stress reduction the least resistant is the composite to unwanted viscoelastic behavior. It can be inferred that at the combination of elevated temperatures and higher stress levels, the amount of relaxation in stress increases significantly. The results suggest that having CNTs at the interface play a positive role in reducing the stress relaxation level. This again can be attributed to the mechanisms opposing the viscoelastic behavior such as enhanced stiffness and improved

adhesion and interlocking at the epoxy/reinforcement interfaces. Among the different configurations, the fine patterned growth exhibited the least stress relaxation, this was particularly the case at the most severe case of 60 MPa and 75 °C where the 53-micron patterned composite exhibited a 5 MPa relaxation in stress compared to 11 MPa for the reference composite.

Overall, one can conclude that viscoelastic behavior of FRPs is responsive to fiber/matrix interface in more than one way. The epoxy impregnation through the CNTs and its adhesion to both CNTs and carbon fiber control the strength of the interface and hence the viscoelastic behavior of the composite. Growing CNTs uniformly on the carbon fibers, promotes larger CNTs/matrix interface while hindering the impregnation of the carbon fibers with the matrix. The patterned growth offers a path to resolve these conflicting factors, by allowing significant interface area between the grown CNTs and the epoxy and providing other areas at which the fibers are fully immersed in the epoxy matrix during the fabrication process.

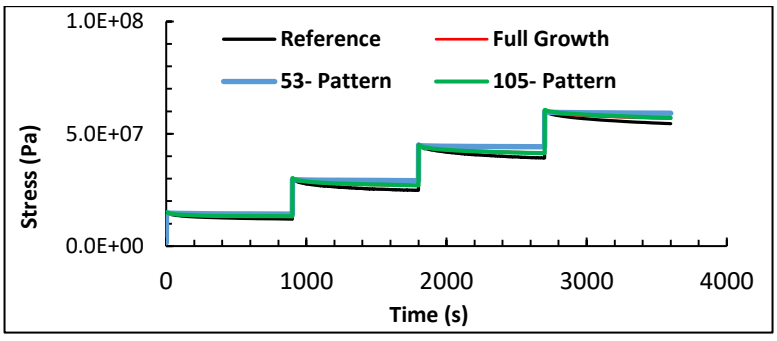

Figure 5.12 Stress relaxation curves for the different composite configurations under 25 °C at stress levels 15-60 MPa.

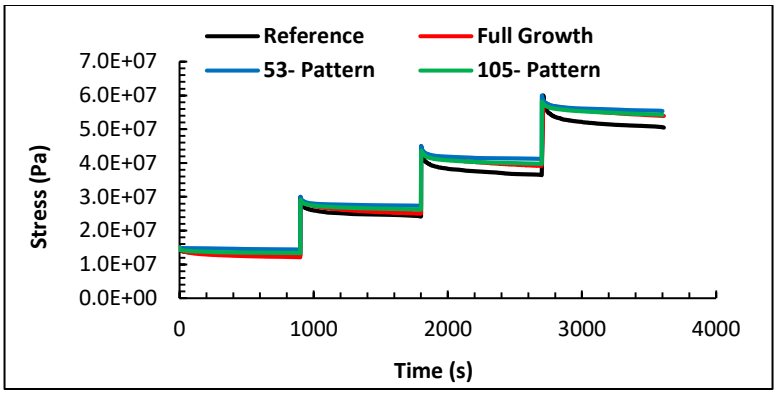

Figure 5.13 Stress relaxation curves for the different composite configurations under 50 °C at stress levels 15-60 MPa.

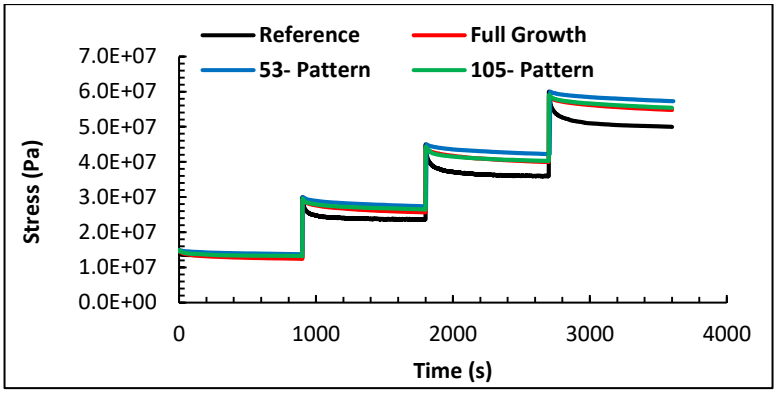

Figure 5.14 Stress relaxation curves for the different composite configurations under 75 °C at stress levels 15-60 MPa.

5.3.3. Fracture Analysis

To probe the effects of the growth patterns further, the fracture surface of the tensile samples was analyzed, as shown in Figure 5.15. Figure 5.15.a) clearly shows the fracture was dominated by excessive fiber breakage, the lack of strong CNTs interface between the fiber and matrix lead to unstoppable crack propagating. Upon growing CNTs, they act as crack stopper/deflector as shown in Figure 5.15.b). The crack initiated within the matrix and upon loading it gets deflected along the direction of the fibers as shown in Figure 5.15.b), indicating that the presence of CNTs assisted the matrix in transferring the load to the fiber.

The matrix failure was also observed for the 105 μm patterned growth shown in Figure 5.15.c), however the cracks were one-sided at the interface between the fiber and matrix. The relatively long distance between the grown CNT patches (105 μm) in the coarse patterned CNTs provide more spacing on the fibers that can be impregnated with the epoxy without interacting with the CNTs leading to relatively weaker interfaces that have no obstacles to hinder the crack propagation. This suggests that the interspacing between the CNTs patch should be optimized.

This hypothesis is supported by the fractography of the finer patterned growth, Figure 5.15.d). The composite exhibited no cracks in between the fiber indicating that the patterned growth induced interlocking mechanism created strong obstacles that suppressed crack imitation which led to attaining the highest strength among all the composites configurations. The inset figure in Figure 5.15.d), the role of the surface grown MWCNTs in matrix crack blocking can be seen.

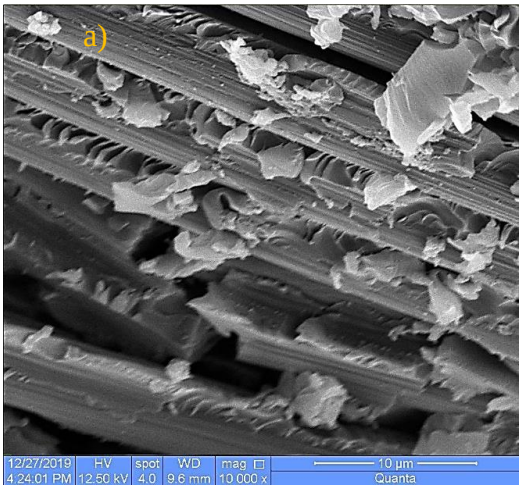

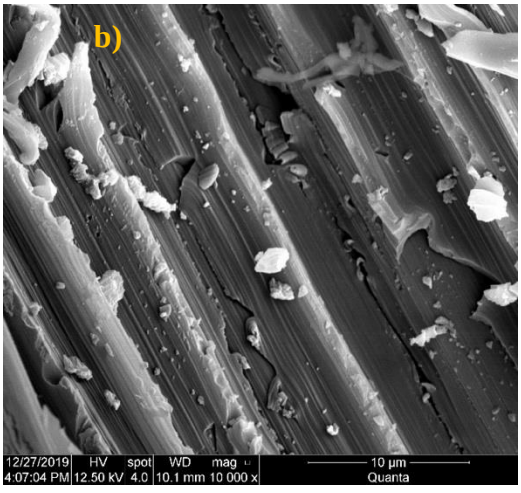

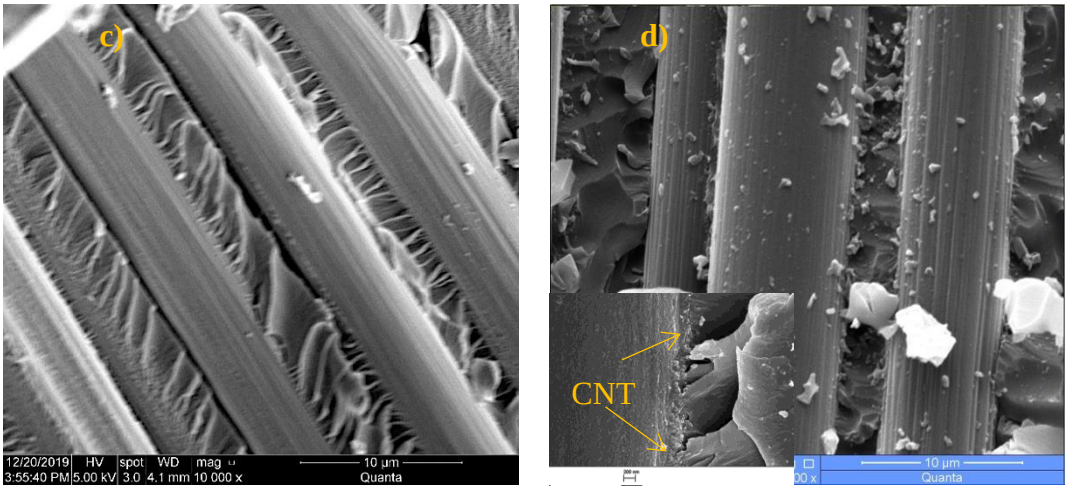

Figure 5.15 a) SEM fractography of the composites based on desized fibers. b) SEM fractography of the composites based on uniform growth fibers. c) SEM fractography of the composites based on 105 µm patterned growth fibers. d) SEM fractography of the composites based on 53 µm patterned growth fibers.

6. Viscoplasticity in Composites

In this chapter, all the experiments and results pertaining to viscoplasticity in hybrid composites fabricated by modifying carbon fiber surface using CNTs are discussed. Experimental and analytical procedures to predict creep were discussed in detail.

6.1. Viscoplastic Properties

Composites based on polymeric matrices experience irreversible time dependent deformation when subjected to high temperatures, constant or dynamic loads, and high strain rates, over long periods of time. This is referred to as viscoplastic behavior. To predict material stability over long time periods under given loading conditions, and investigate unanticipated failure in composite structures, understanding this behavior is necessary. This phenomenon can be experimentally monitored using stress relaxation and creep tests.

6.1.1. Stress Relaxation

A simple example of this process is when an elastic band is wrapped around to hold certain amount of cash paid by a bank. If this cash is saved for a long time inside a locker, it can be noticed that the band loses its integrity the next time one returns to use this money. Similarly, when composite reinforcements are used inside concrete beams, over time, they relax, resulting in loss of compressive strength in the beams. In humans, doctors recommend muscle relaxation techniques to ease the muscle tension when experiencing anxiety. Hence, stress relaxation is the reduction in stress in a sample when subjected to a constant strain to reach an initial elongated length. This length is held constant

through time during experiments. So, any changes can occur only at molecular level, due to microscopic relaxation of polymeric chains or their viscous flow.

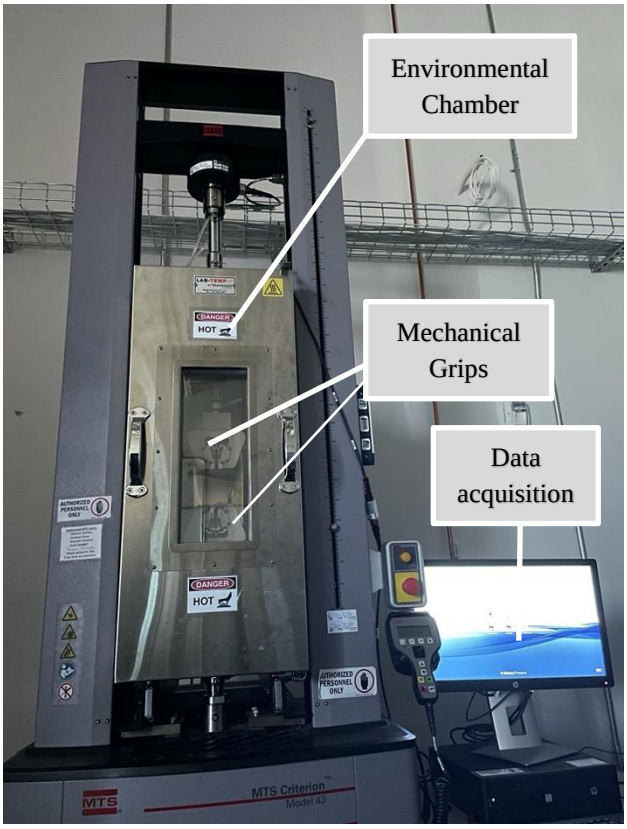

Figure 6.1 Environmental chamber and sample mount description

Figure 6.2 Chiller and temperature controller

In this dissertation, stress relaxation tests were performed by holding composite coupons, cut like the ones used for tensile tests in the grips of the

MTS machine, at multiple constant strains, and different temperatures. Four different configurations of composites with CNTs surface treatments were tested: Desized, full growth, 53 μm, and 105 μm. Each configuration was subjected to four different temperatures: 25 ºC, 45 ºC, 55 ºC and 75 ºC.

The temperature was maintained by an environmental chamber compatible with the MTS grips. The sample was gripped inside this chamber, while the temperature was controlled by a controller linked to this chamber. A chiller was run simultaneously to protect the load cell of the MTS machine from overheating.

The experimental setup is shown in the Figure 6.1and Figure 6.2. Tensile tests at these temperatures were performed to calculate strength and modulus at these temperatures for all configurations. This was followed by the relaxation tests. At each temperature, they were held at four constant strain levels, corresponding to 15 %, 30 %, 45 % and 60 % of the strength of that configuration, at the particular temperature. Each constant strain segment lasted for 30 min. The decay in stress (i.e., relaxation) with time was plotted.

6.1.2. Creep

Failure in aircraft or automobile components at loads much lower than their yield strengths is a common phenomenon. This is partly because of their design. They are designed to withstand sudden impact loads, and low static loads at low temperatures. When the material experiences prolonged loading at low levels at higher temperatures, significant deformation can accumulate which can result in structural instability and failure. This phenomenon of a material experiencing

increasing strain under a constant load is called creep. This can be experimentally monitored by subjecting a sample to a constant load for long periods of time under a constant temperature. Creep is extremely sensitive to temperature. Hence, it is recommended that variations should not exceed 0.2 ºC (Hart & Solomon, 1973). Also, while measuring the strain during this time, care should be taken to offset any strain in the experimental chamber due to its compliance. The setup usually has metal grips and chamber, which can add thermal strains at higher temperatures. An extensometer on the sample gauge length to measure strain can eliminate this error by an acceptable range.

In this dissertation, the same experimental setup, composite configurations, and procedure used for stress relaxation test were used for creep. The major difference was that the sample was held at constant loads corresponding to 15 %, 30 %, 45 % and 60 % of the strength of that composite configuration. Extensometer of 25.4 mm gauge length was used for strain measurements. Each constant load segment lasted for 30 min. The variation in strain with time was plotted.

6.2. Analytical Model for Creep Prediction

CFRPs majorly are composed of two separate constituents: Fiber, and matrix. While fibers are linear elastic in nature, the polymer matrix is viscoplastic in nature. Hence, the effects of plasticity and rheology need to be taken into consideration while studying the behavior of CFRPs. The time-dependent behavior of a polymer changes drastically with temperature, and there is a structural shift at the glass transition temperature, T_g. This is the temperature

where the relatively solid and brittle polymer transforms to a glassy state which acts like a viscous fluid. The plasticity behavior in solids is usually seen during the transition stage, while viscous fluid rheology behavior is seen after the transition to the glassy state. However, most analytical models are exclusively built either based on plasticity or rheology. There are multiple analytical models built to understand the elastic-viscoplastic behavior of such composite materials. Some of them include Perzyna's model, Krempl's model, and Sun and Gates model (M. S. Al-Haik, 2002).

In this dissertation, Sun and Gates analytical model was implemented to predict creep over long periods of time utilizing data from shorter load relaxation tests (Gates et al., 1994; Gates & Sun, 1990). Experimental methods to predict creep are expensive and time consuming due to the prolonged exposure of sample to a constant load at a particular temperature. Ideally, the sample should be left at a constant load for a time ranging from a week to a month for proper data accumulation. In these cases, analytical models can save time and resources, if they could predict the long-time creep behavior within an acceptable error margin.

The current model uses the data from stress relaxation and tensile tests at various temperatures to calculate the constants required to predict creep over time. From experience, this model is usually accurate at low to moderate temperatures. However, it deviates noticeably from the experimental creep behavior at higher temperatures. Nevertheless, due to the lack of a better phenomenological model in literature, this model was used to compare the creep

behavior in various hybrid composite configurations.

6.2.1. Model Description

This section outlines the Sun and Gates model briefly. This model assumes uniaxial loading and that the CFRPs are orthotropic in nature. Due to the nature of loading, the total strain can be written as the sum of elastic and plastic terms for the time-dependent elastoplastic constitutive equation. This can be expressed as:

$$\varepsilon^t = \varepsilon^e + \varepsilon^p \quad (6.1)$$

The relation for elastic strain can be expressed using Hooke's law as:

$$\varepsilon^e = \frac{\sigma}{E} \quad (6.2)$$

The relation for plastic strain can be expressing using the power law as:

$$\varepsilon^p = A\sigma^n \quad (6.3)$$

where A and n are material constants collected from experimental stress relaxation data. Differentiating Equation 6.1 with respect to time gives the rate dependent strain equation as shown below:

$$\dot{\varepsilon} = \dot{\varepsilon}^e + \dot{\varepsilon}^{vp} \quad (6.4)$$

where the elastic strain rate is given by:

$$\dot{\varepsilon}^e = \frac{\dot{\sigma}}{E} \quad (6.5)$$

The second term in Equation 6.4, indicating the viscoplastic strain rate, can be split into two components:

$$\dot{\varepsilon}^{vp} = \dot{\varepsilon}^{(i)vp} + \dot{\varepsilon}^{(ii)vp} \quad (6.6)$$

Differentiating Equation 6.3 with respect to time gives the first term in viscoplastic strain rate:

$$\dot{\varepsilon}^{(i)vp} = \begin{cases} An(\sigma)^{n-1}\dot{\sigma} & for\ \dot{\sigma} > 0 \\ 0 & for\ \dot{\sigma} < 0 \end{cases} \quad (6.7)$$

To obtain the second component in Equation 6.6, overstress concept developed by Malvern (1949) and coined by Perzyana (1966) was used. Overstress is the difference between instantaneous stress from the stress relaxation test and the stress at the same strain noted in a static tensile test. Using this concept, the second component is given by:

$$\dot{\varepsilon}^{(ii)vp} = \left\{\frac{\langle H \rangle}{K}\right\}^{1/m} \quad (6.8)$$

Where H is the overstress, < > are Macaulay brackets, K and m are material constants to be collected from experimental relaxation data.

$H = \sigma - \sigma^*$, where H is a scalar quantity, σ denotes the instantaneous stress from the tensile data, σ^* denotes the quasistatic stress from relaxation data. Hence, Equation 6.8 can be re-written as:

$$\dot{\varepsilon}^{(ii)vp} = \begin{cases} \left[\frac{\langle \sigma - \sigma^* \rangle}{K}\right]^{1/m} & if \quad \sigma > \sigma^* \\ 0 & if \quad \sigma \leq \sigma^* \end{cases} \quad (6.9)$$

The quasistatic stress, σ^* can be calculated by solving the quasistatic stress-strain equation shown below:

$$\varepsilon = \frac{\sigma^*}{E} + A(\sigma^*)^n \quad (6.10)$$

The dynamic or instantaneous stress, σ can be calculated from the tensile data by locating the value of stress at that particular strain using recorded stress Vs strain curves.

6.2.2. Material Constants Calculation

In the section 6.2.1, four temperature dependent material constants K, m, A, and n are defined, which are to be obtained from the experimental stress

relaxation test data. During these tests, the quasistatic stress is constant, stress rate is negative, and the total viscoplastic strain rate is zero. This infers that, $\dot{\varepsilon}^{(i)vp} = 0$ from Equation 6.6. Combining Equation 6.4 and Equation 6.6,

$$\dot{\varepsilon}^{vp} = \dot{\varepsilon}^{(ii)vp} = -\dot{\varepsilon}^{e} \quad (6.11)$$

From Equation 6.9 and Equation 6.11, it can be written as:

$$\dot{\varepsilon}^{vp} = -\frac{\dot{\sigma}}{E} = \left[\frac{\langle\sigma-\sigma^{*}\rangle}{K}\right]^{1/m} \quad (6.12)$$

From the stress relaxation data, stress vs. time data was accumulated. Applying polynomial regression for this data results in an equation in terms of stress and time. The differential of this equation with respect to time gives the equation required for the calculation of stress rate in Equation 6.12. The curves for the evolution of stress vs. strain rate for different configurations at various temperatures are shown in Appendix A. These curves are an effective method to calculate multiple strain rates, rather than experimental creep tests since each creep test outputs only one strain rate after a week-long test run. Using these logarithmic curves, multiple strain rates can be obtained from 2 h long stress relaxation tests.

Along with the strain rates, another usage of these plots is the calculation of quasistatic stress, σ^{*} in Equation 6.12. The asymptotic values of the plots are considered as the values for quasistatic stress. Since all the other variables are known in Equation 6.12, a logarithmic plot of overstress versus the plastic strain rate will reveal the m and K material constants for various composite configurations at different temperatures. These curves are shown from Figure 6.3 to Figure 6.6.

Also, both the parameters m and K are independent of the initial load applied in a load relaxation test. These tests are repeated for multiple loads, each at a constant strain level, to calculate the quasistatic loads as mentioned above. These series of tests result in a quasistatic stress-strain curve. These curves can be fit in a logarithmic fashion to Equation 6.10 for the calculation of the other two material constants, A, and n. These curves are shown from Figure 6.7 to Figure 6.10.

The material constants calculated from the logarithmic curves are tabulated from Table 6.1 to Table 6.4 for the four different CNTs based patterned composite configurations. These values were utilized as inputs to run the analytical creep models.

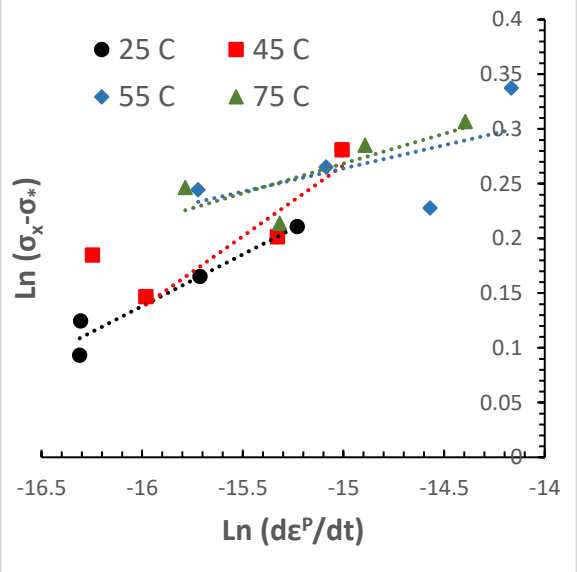

Figure 6.3 Logarithm of overstress vs. logarithm of strain rate at four temperatures for Desized composite configuration. These curves are used to determine the material constants K and m at each temperature. Overstress is in MPa.

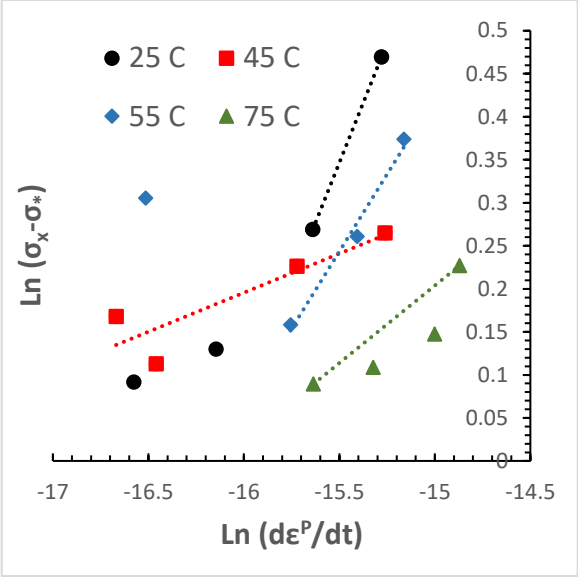

Figure 6.4 Logarithm of overstress vs. logarithm of strain rate at four temperatures for Full Growth composite configuration. These curves are used to determine the material constants K and m at each temperature. Overstress is in MPa.

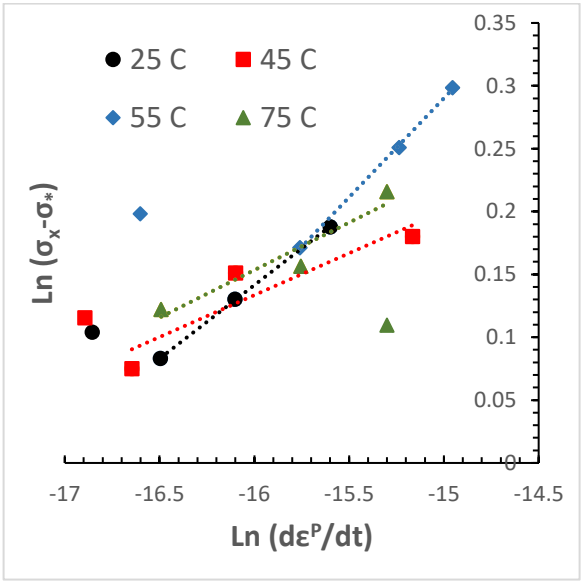

Figure 6.5 Logarithm of overstress vs. logarithm of strain rate at four temperatures for 53 μm patterned composite configuration. These curves are used to determine the material constants K and m at each temperature. Overstress is in MPa.

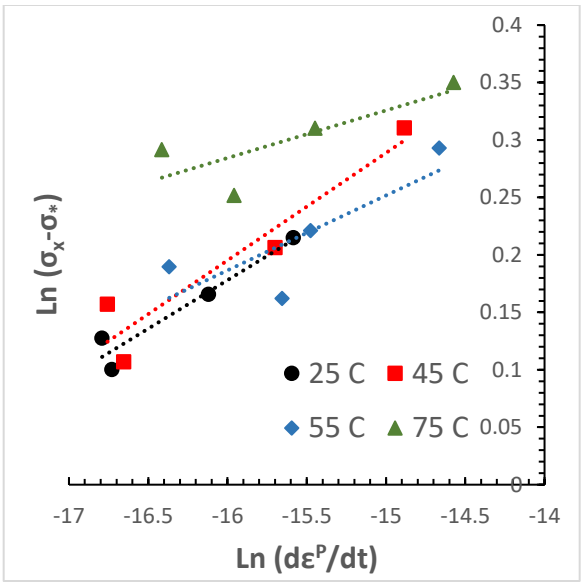

Figure 6.6 Logarithm of overstress vs. logarithm of strain rate at four temperatures for 105 μm patterned composite configuration. These curves are used to determine the material constants K and m at each temperature. Overstress is in MPa.

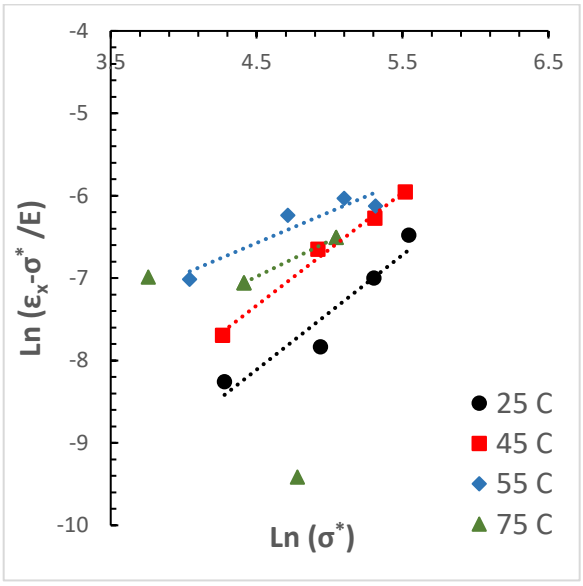

Figure 6.7 Logarithm of plastic strain vs. logarithm of quasistatic stress at four different temperatures for Desized composite configuration. These curves are used to determine the material constants A and n at each temperature. Quasistatic stress in Mpa.

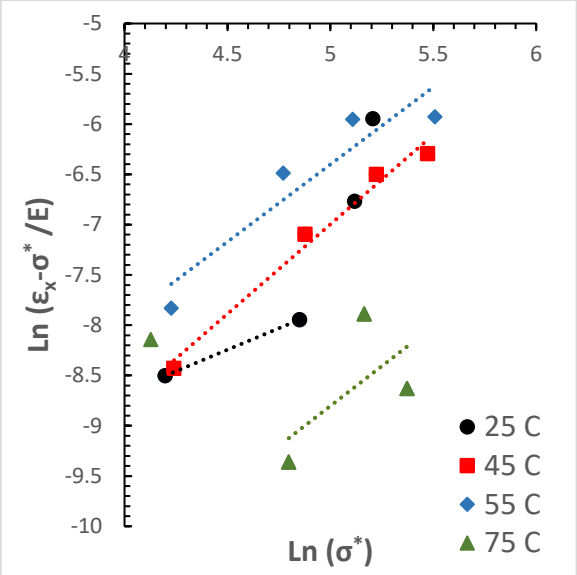

Figure 6.8 Logarithm of plastic strain vs. logarithm of quasistatic stress at four different temperatures for Full Growth composite configuration. These curves are used to determine the material constants A and n at each temperature. Quasistatic stress in Mpa.

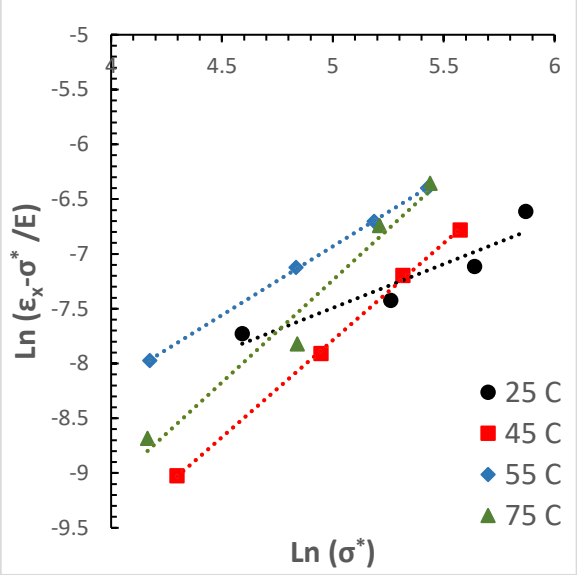

Figure 6.9 Logarithm of plastic strain vs. logarithm of quasistatic stress at four different temperatures for 53 μm patterned composite configuration. These curves are used to determine the material constants A and n at each temperature. Quasistatic stress in Mpa.

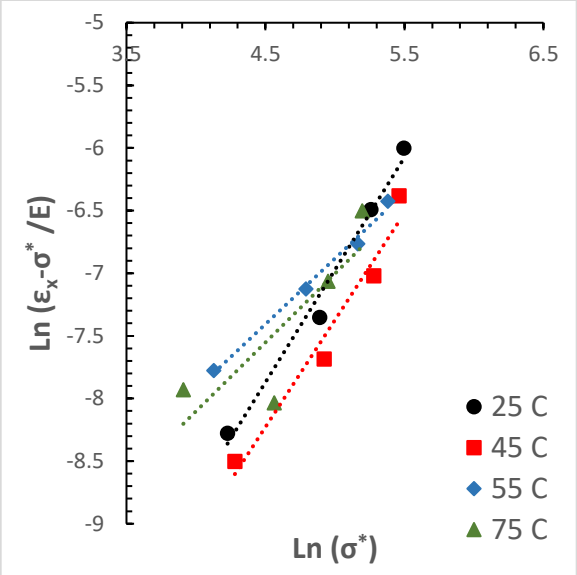

Figure 6.10 Logarithm of plastic strain vs. logarithm of quasistatic stress at four different temperatures for 105 µm patterned composite configuration. These curves are used to determine the material constants A and n at each temperature. Quasistatic stress in Mpa.

Table 6.1

Desized composite configuration properties and material constant values.

Temperature °C	Modulus GPa	Strength MPa	m	K MPa	n	A MPa
25	30	527	0.95	3.81E+07	1.17	5.70E-07
45	31	550	0.9	2.57E+07	1.1	1.39E-06
55	21	475	1.18	1.63E+09	0.5	4.71E-05
75	10	352	1.1	4.52E+08	0.75	1.87E-05

Table 6.2

Full Growth composite configuration properties and material constant values.

Temperature °C	Modulus GPa	Strength MPa	m	K MPa	n	A MPa
25	39	486	0.88	1.00E+07	0.8546	5.62E-06

45	36	517	1.15	7.71E+07	1.7802	1.25E-07
55	41	533	1.1	1.06E+07	1.5378	7.60E-07
75	20	450	1.4	1.01E+07	2.13	5.44E-08

Table 6.3

53 μm patterned composite configuration properties and material constant values.

Temperature °C	Modulus GPa	Strength MPa	m	K MPa	n	A MPa
25	49	712	0.9	2.96E+07	0.6	1.02E-05
45	47	526	1.2	6.52E+07	1.9	5.95E-08
55	37	511	1.2	2.07E+07	1.3	1.84E-06
75	29	476	1.41	6.84E+07	0.794	6.40E-08

Table 6.4

105 μm patterned composite configuration properties and material constant values.

Temperature °C	Modulus GPa	Strength MPa	m	K MPa	n	A MPa
25	46	504	1.14	7.34E+07	1.74	1.18E-07
45	42	535	1.2	7.22E+07	1.76	1.22E-07
55	31	485	1.4	1.55E+08	1.1	5.42E-06
75	23	427	1.7	8.49E+09	1.25	3.73E-06

6.3. Results and Discussion

Experimental and analytical results pertaining to viscoplasticity are presented in this section. The experimental and analytical procedures were discussed in detail in Section 6.1 and Section 6.2 respectively.

6.3.1. Stress Relaxation

Figure 6.11, Figure 6.12, Figure 6.13, and Figure 6.14 represent stress relaxation curves for desized, full growth, 53 μm, and 105 μm configurations, respectively. Each configuration was held for 30 minutes at four different strain levels. This was repeated at four different temperatures. As the strain levels and temperatures increase, the decay in stress also increases as a general trend. The decay indicates undesirable molecular movements within the composite, which leads to plastic deformation, and hence, relaxing the sample. This can also be inferred that, a lower decay of stress with time is desired for better functionality of hybrid composites. At higher temperature of 75 ℃ and the highest strain level, 53 μm and Full growth samples showed lesser decay in stress in comparison to desized configuration. At 45 ℃, all the configurations of CNTs were seen to decay lesser than the desized configuration.

These results prove that CNTs play a significant role as reinforcements between fiber and matrix, providing an interlocking effect to prevent any undesirable movements at a molecular level. Addition of reinforcements like CNTs also means less openings for the epoxy to seep into the fiber. This creates some drop in strength and stiffness, hence viscoplasticity. Ideal patterning of CNT islands could help in achieving an effect which can balance these two-opposite phenomena. In current results, 53 μm and Full growth samples showed promising results to reduce viscoplastic relaxation. Nevertheless, to establish a clear trend, more samples need to be tested at each temperature, for a longer period of time.

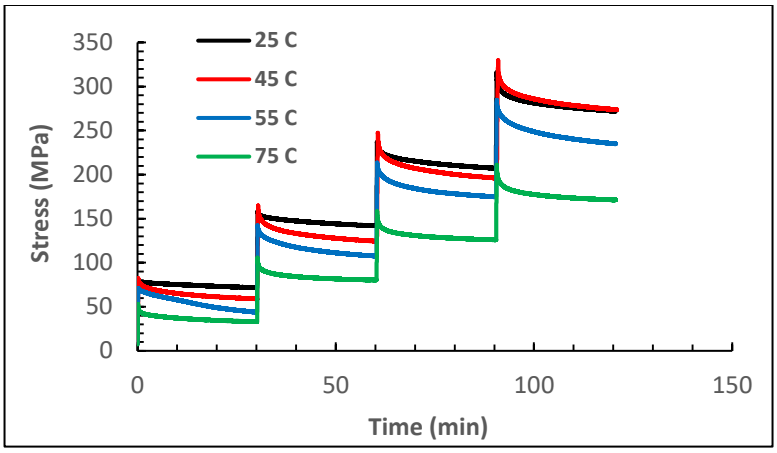

Figure 6.11 Stress relaxation tests for desized configuration

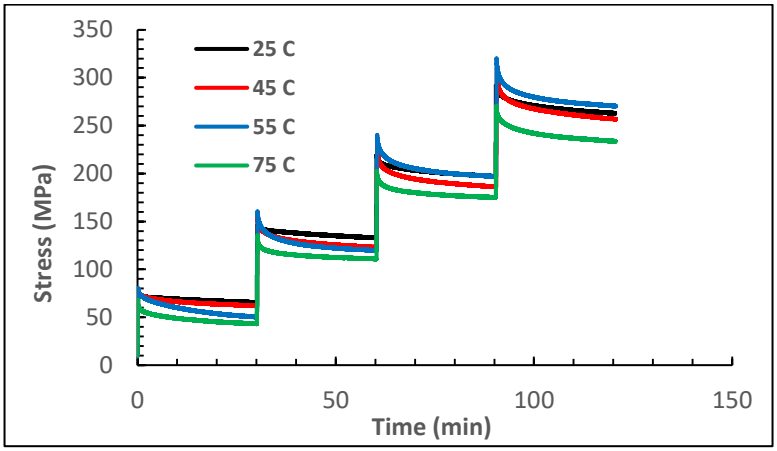

Figure 6.12 Stress relaxation tests for full growth configuration

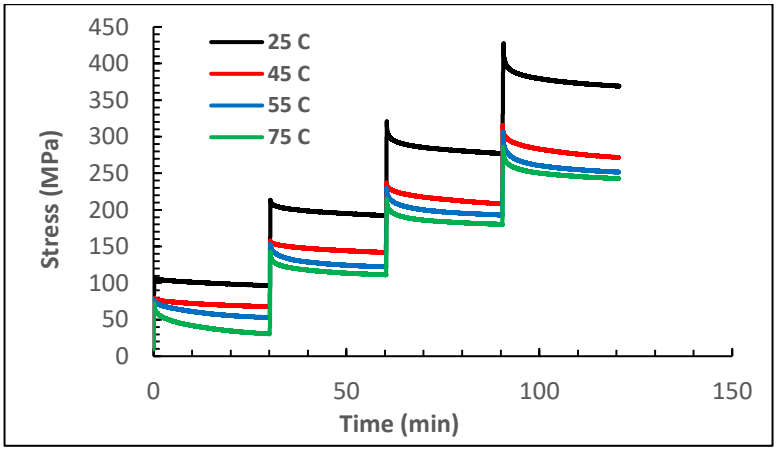

Figure 6.13 Stress relaxation tests for 53 μm configuration

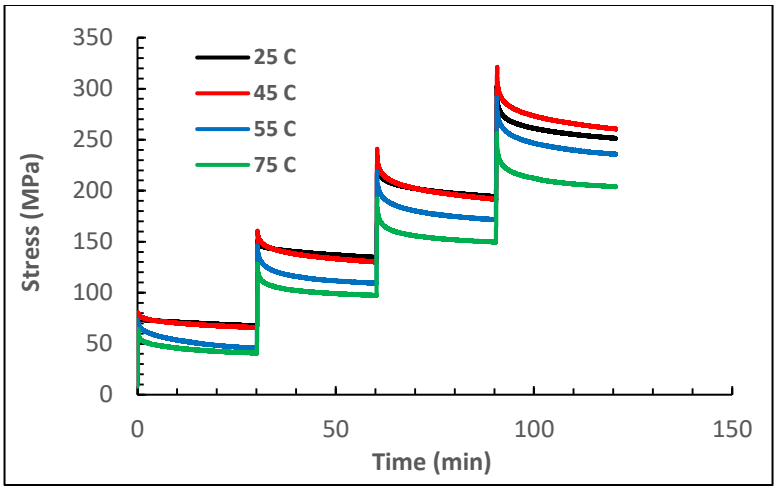

Figure 6.14 Stress relaxation tests for 105 μm configuration

6.3.2. Creep

Figure 6.15, Figure 6.16, Figure 6.17 and Figure 6.18 show the creep behavior in desized, full growth, 53 μm, and 105 μm configurations, respectively. Each configuration was held at four stress levels for 30 min each. This was repeated at four different temperatures. The change in strain in each case was recorded with the help of an extensometer. The strain increases with increase in stress and temperature as a general trend in each configuration. In Figure 6.15, the initial values of strains for each temperature are clearly different from each other. These values are based on the strength values of each configuration at that temperature. It can be clearly seen that the sample at 75 C experienced the highest creep because of an increasing slope at higher stress levels. The following three figures could be studied in a similar manner.

When comparing different configurations with each other, it can be concluded that 53 μm, and 105 μm showed much higher resistance to creep than desized and full growth configurations. This is based on comparing their rising

slopes at each stress level and temperatures. Between 53 μm and 105 μm, the former provided more resistance to creep than latter. These results indicate that patterning of CNTs play a major role in contributing to rid the composites from unwanted effects of viscoplasticity.

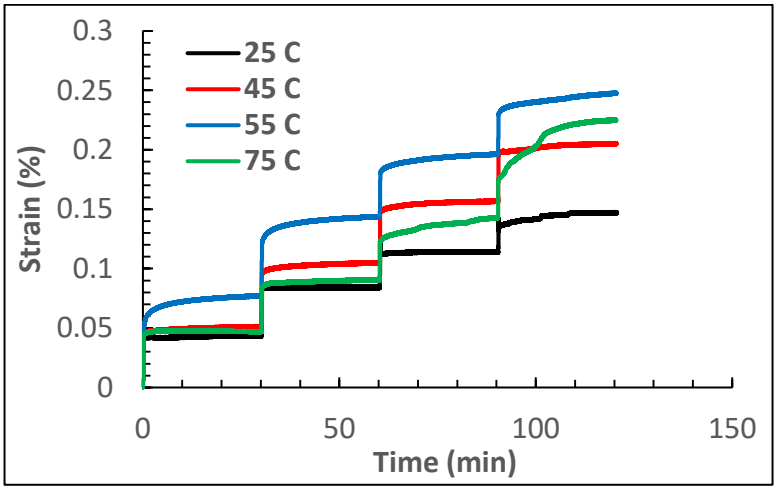

Figure 6.15 Creep tests for desized configuration

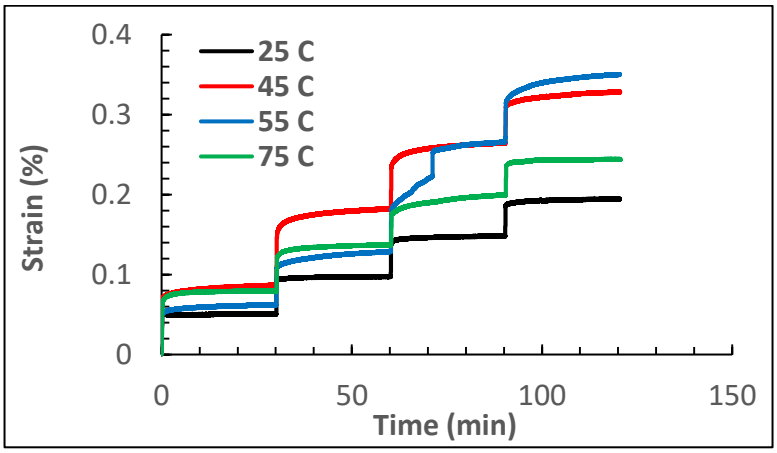

Figure 6.16 Creep tests for full growth configuration

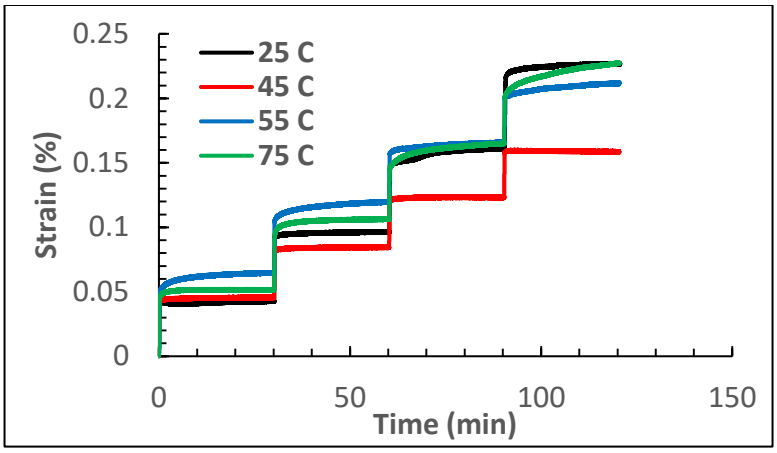

Figure 6.17 Creep tests for 53 µm configuration

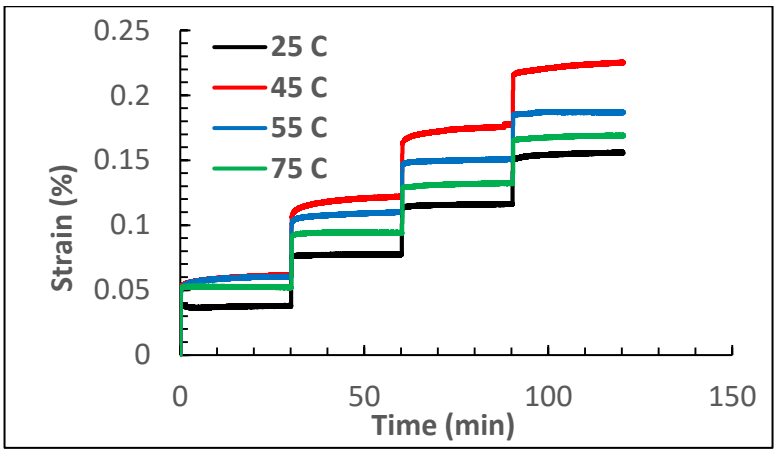

Figure 6.18 Creep tests for 105 µm configuration

6.3.3. Creep Model Results

Figure 6.19, Figure 6.20, Figure 6.21, and Figure 6.22 show the analytical model creep results for desized, full growth, 53 µm, and 105 µm configurations respectively. Each configuration had four material constants at each temperature. Since the model is independent of the initial stress levels, the model is run four times, one for each stress level, at a given temperature. The time of the run was kept constant at 30 min at each stress level to compare against experimental data. The change in strain with time was the output of this analytical model. The strain

increases with increase in stress and temperature as a general trend in each configuration.

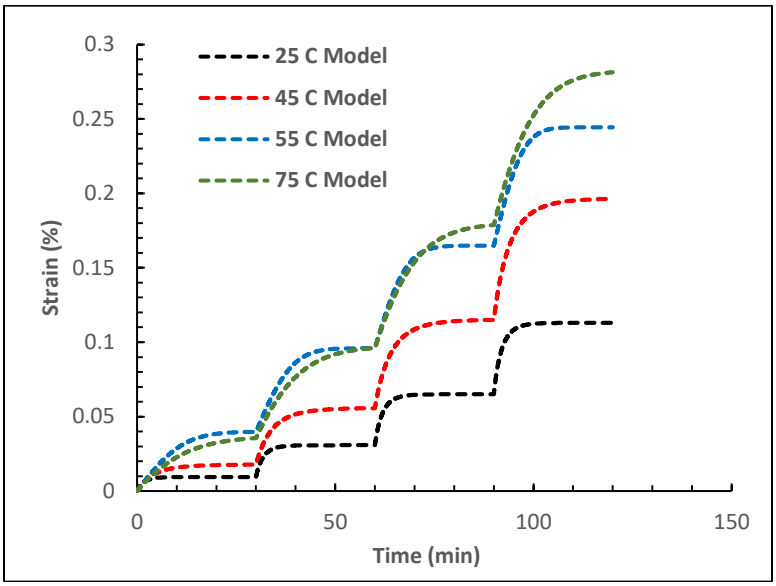

Figure 6.19 Creep tests for Desized composite configuration using analytical model.

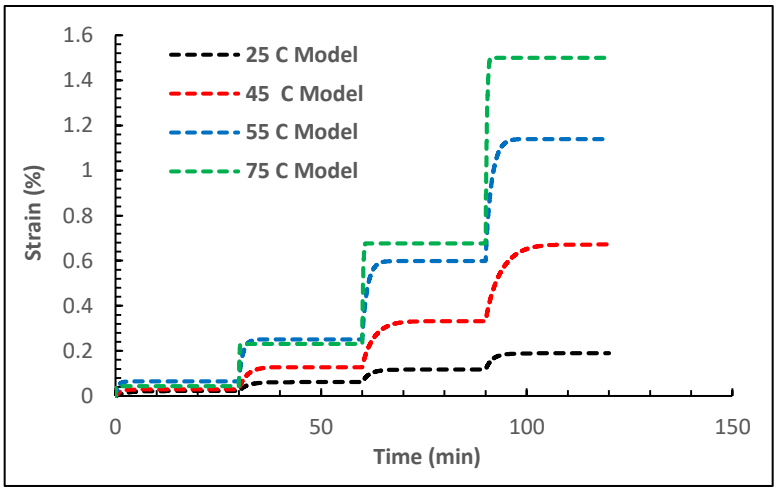

Figure 6.20 Creep tests for Full Growth composite configuration using analytical model.

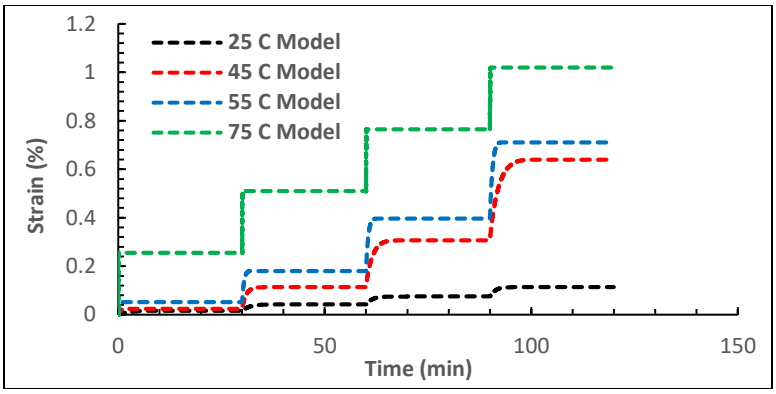

Figure 6.21 Creep tests for 53 µm composite configuration using analytical model.

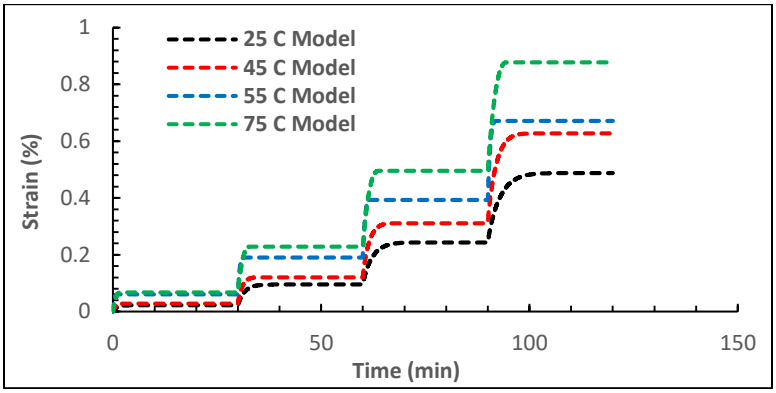

Figure 6.22 Creep tests for 105 µm composite configuration using analytical model

6.3.4. Comparison of Experimental And Model Creep Results

Figure 6.23 to Figure 6.26 plot both experimental and analytical model creep results are together for comparison. In both cases, creep increased with increase in temperature and load. Also, as seen in Figure 6.23, the slope of the strain curve increased at higher stress levels at 55 C and 75 C. This is evident both in the case of experiments and simulations. However, the values of the strain calculated through the analytical model are much higher than the experimental values. This trend can also be observed for the other three composite configurations. Though the analytical and experimental results show some convergence with each other at lower loads and temperatures of 25 C, and 45 C,

the prediction of analytical creep values at higher loads and temperatures are seen to be higher than the experimental results.

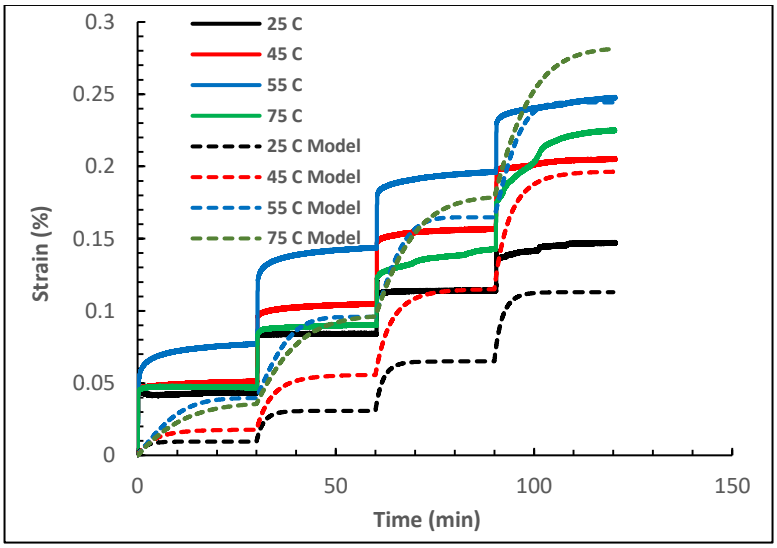

Figure 6.23 Comparison of experimental and analytical creep model results for desized composite configuration.

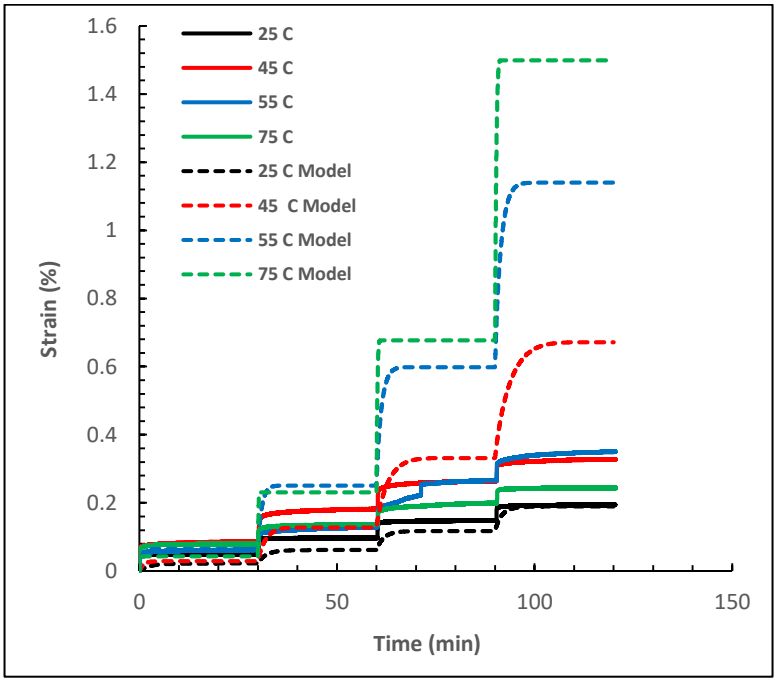

Figure 6.24 Comparison of experimental and analytical creep model results for full growth composite configuration.

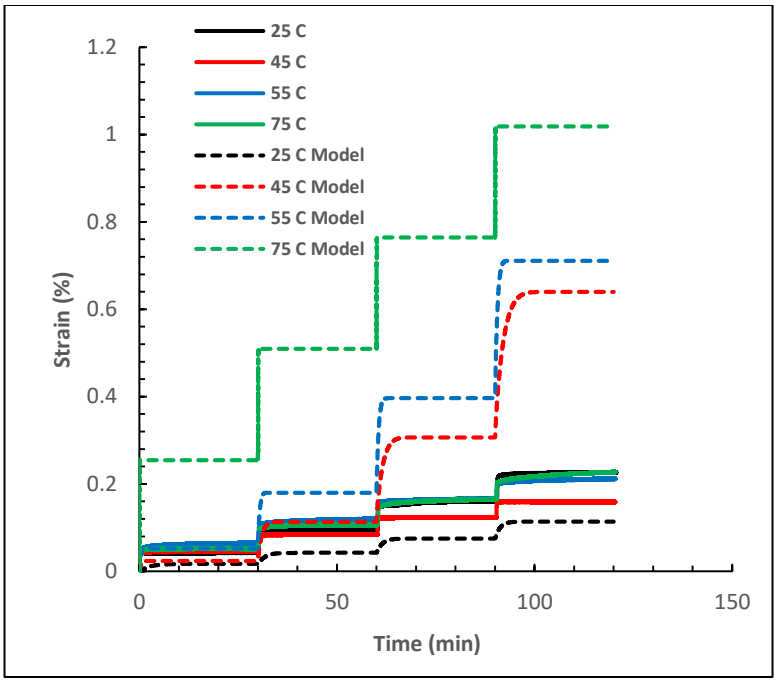

Figure 6.25 Comparison of experimental and analytical creep model results for 53 µm composite configuration.

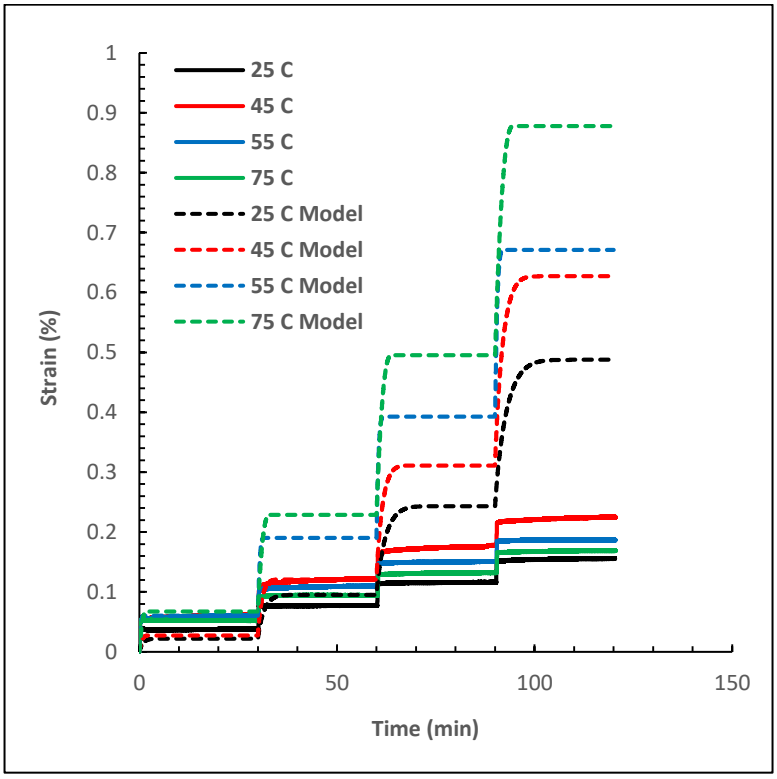

Figure 6.26 Comparison of experimental and analytical creep model results for 105 µm composite configuration.

7. Crack Propagation in Hybrid Composites

In this chapter, all the experiments and simulation results pertaining to crack propagation in hybrid composites fabricated by modifying carbon fiber surface using CNTs are discussed. Experimental and modeling procedures to study crack propagation were discussed in detail.

7.1. Fracture Toughness

This is the measure of a material's ability to resist fracture. It is quantified in terms of a parameter called stress-intensity factor (K). This is the maximum value of stress that can be applied to a sample containing a crack of certain length. There are three different types of stress-intensity factors, based on the loading direction on the sample with respect to the crack direction, and its thickness. Among them, K_{IC} is widely used for composite materials design. This is the case where the loading direction is perpendicular to the crack plane, also known as Mode I loading. While K_{IC} describes the stress at the edges of the crack, the energy required for the crack initiation is described by G_{IC}. This is called the critical strain energy release rate (Roberts et al., 1978). Double cantilever beam (DCB) tests, illustrated in this chapter, are usually utilized to identify this parameter.

In this dissertation, the samples used for testing comprised 10 layers of carbon fiber, a combination of PR2032 resin and hardener PH3665, fabricated in an autoclave, as described in Section 5.1. The top 4, and bottom 4 laminae were based on the reference carbon fibers with no surface modifications. The middle two layers were hybrid, with various patterns of CNTs, with which they are

labeled for comparison. The crack was introduced with the help of a PTFE insert of 51 μm thickness in between the two middle layers. During fabrication, half of the PTFE is left overhanging, while the other extended inside the layers to create an initial crack opening. The tip to the edge where the PTFE layer ends is around 25 mm in length. After fabrication, these composite laminates were cut into coupons of dimensions detailed in Figure 7.1. To grip the opposite ends for allowing crack propagation while loading these coupons, aluminum piano hinges on top of G-10 tabs were glued on the edges, as shown in the Figure 7.1.

To track the crack propagation, a digital image correlation (DIC) technique by (Correlated Solutions, Inc.) was used. Two cameras were used to capture the phenomenon of the crack propagating through the sample during Mode I loading. The sample was marked with lines spacing 0.5 mm to capture the crack movement. Effort was made to synchronize the loading using MTS and the image capturing using DIC. A frequency of 10 Hz was used in both cases. The loading rate of MTS was set to 3 mm/min. The DCB test procedure was followed according to the ASTM D5528-13 standard (2013).

The critical strain energy release rate, $G_{IC,}$ also known as interlaminar fracture toughness was calculated using the following equation (Boroujeni & Al-Haik, 2019):

$$G_{IC} = {}^{3P\delta}/_{2b(a+|\Delta|)} \quad (7.1)$$

where P is the load applied in Newtons (N), δ is the deflection due to applied load or crosshead movement due to the load in meters (m), b is the width of the DCB sample in meters (m), a is the crack length in meters (m), and Δ is the

correction factor to account for the extension resulting from rotation of the DCB arms at the crack front. This was quantified by plotting cubic root of compliance values, $(\delta/_P)^{(1/3)}$,vs. crack length, a. The point of intersection of this curve fit with the X-axis was taken as the value of Δ. To accommodate for large displacements, another correction factor was multiplied by the final calculated fracture toughness values. This is denoted by F, given by the following equation:

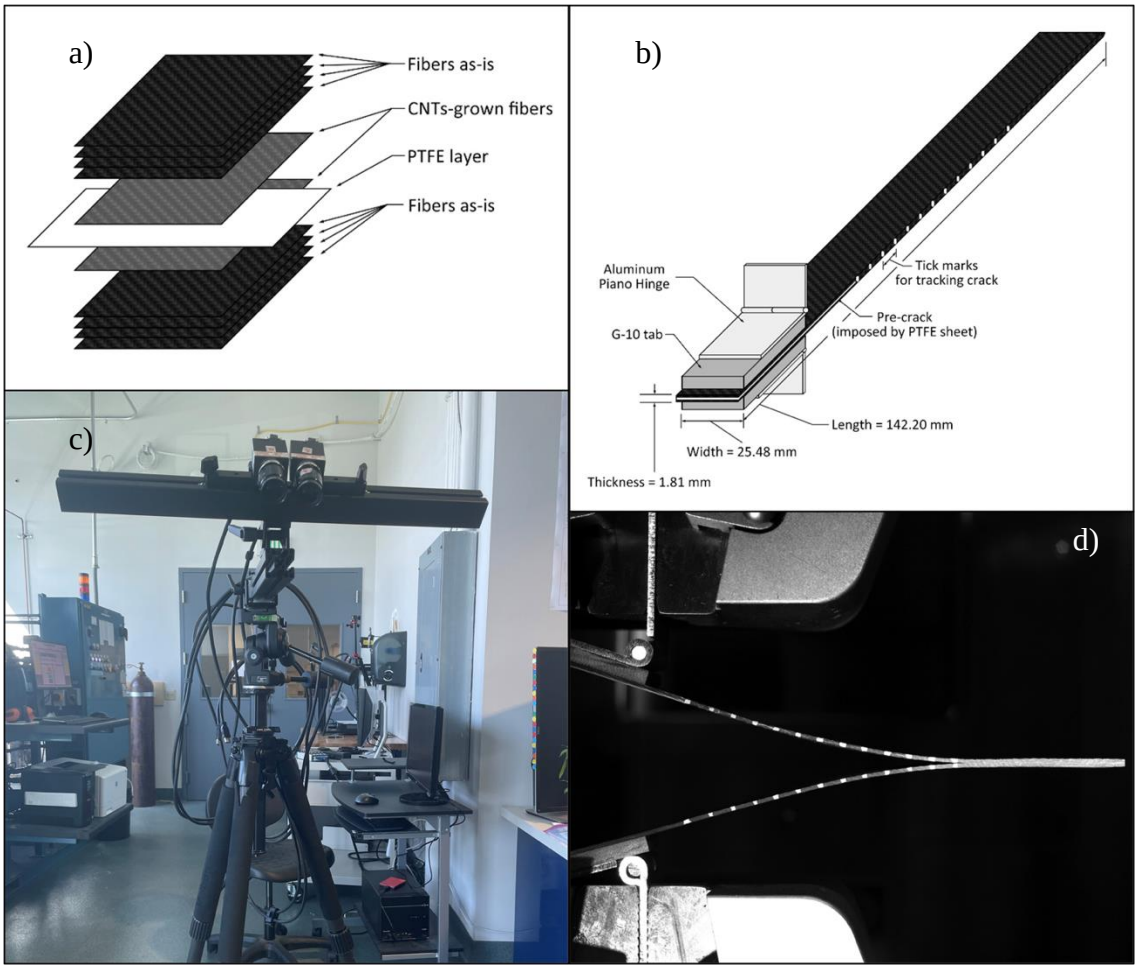

Figure 7.1 a) Stacking of carbon fiber layers with PTFE in the mid-surface during fabrication; b) Crack sample design; c) DIC equipment used for tracking the crack; d) Sample during crack propagation while mounted in the MTS grips.

$$F = 1 - \frac{3}{10}(\delta/_a)^2 - \frac{3}{2}\left(\delta t/_{a^2}\right) \quad (7.2)$$

In the above equation, t is the perpendicular distance between the center of the piano hinge and the top surface of the sample mounted, added to quarter thickness of the sample. For plotting G_{IC} through the crack growth, visual inspection was carried out to select the crack initiation points while it was propagating through each tick mark. A series of data points were collected to plot G_{IC} Vs Crack length. These are also called R-Curves. This procedure was followed for four different configurations with CNTs used for surface modifications: Desized, full growth, 53 μm, and 105 μm. Two samples were tested for each configuration.

7.2. Delamination Using ANSYS

Mechanical APDL 19.1 module in ANSYS was used to model delamination in composite materials. Two different simulations were implemented: cohesive zone modeling (CZM) based model; virtual crack closure technique (VCCT) based model. CZM method is built on the theory that the stress transfer capacity between two surfaces adhered to each other cannot be hindered immediately after damage initiation. This is rather governed by a progressive degradation of the interface stiffness. VCCT is an approach based on linear elastic fracture mechanics (LEFM). It assumes that the energy required to separate a surface is the same as the energy required to close the same surface. It was initially theorized to calculate the energy release rate of a cracked surface (H S & N, 2014).

Each simulation was run for four different configurations of hybrid composites: Desized, 53μm CNTs, 105μm CNTs, Full growth CNTs. The

material model was assumed orthotropic. The material properties of each configuration were supplied from the experimental data.

A simple geometrical model imitating experimental samples in dimensions and initial crack insert length was constructed ANSYS design modeler (DM). This can be seen in Figure 7.2. This model was common for both VCCT and CZM.

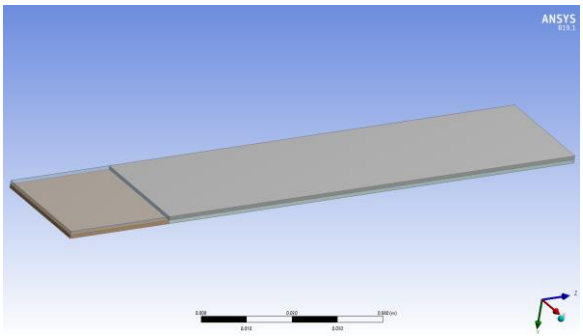

Figure 7.2 Model built in ANSYS for delamination

7.2.1. CZM Model Setup

Initially, material properties were supplemented to the model based on the experimental results of the different configurations of composite. This was followed by applying an appropriate mesh. Analysis was checked for mesh convergence. Various mesh sizes were tried before choosing an appropriate one to avoid any compromise in the accuracy of results. An element size of 3.0 mm sufficed after this exercise. After meshing, fracture module was added to the model tree. Pre-Meshed crack with an appropriate coordinate system at the crack front was introduced. This was followed by the addition of interface delamination subset in fracture model tree. A pre-defined cohesive zone material was assigned as an adhesive contact between the two separating surfaces. Among

various methods available in ANSYS to define this cohesive zone, exponential form was used in this dissertation (Gliszczynski et al., 2019). This form is based on surface potential requiring two relevant input parameters in Mode I loading: Maximum normal traction of the fiber/epoxy system, σ ; Normal separation across the interface, given by $\frac{G_{IC}}{e\sigma}$ where G_{IC} is the critical energy release rate for each configuration from experimental crack propagation experiments, and e is exponential constant (Bahei-El-din, 1996).

This was followed by defining the geometrical constraints: displacement in global y axis mimicking the crosshead loading, fixed at the bottom edge mimicking the grips. The required results like crack propagation length, total deformation, force reaction and energy release rates were chosen in the solution model tree. This completed the model, after which it was run four times for all the composite configurations. The results were then plotted for comparison.

7.2.2. VCCT Model Setup

Like CZM, material assignment, mesh, fracture, constraints, and solution tree were set up in VCCT. The major difference was that, under interface delamination subset, VCCT method assigned to an adhesive material was selected. Linear fracture criterion was used for defining the adhesive. This required three parameters: Critical Energy-Release Rate in mode I, mode II, and mode III. Since this model was built for delamination using mode I type loading, Critical Energy-Release Rate in mode I is the most relevant parameter. This was gathered from the experimental crack propagation results for each configuration. After the model completion, the results were plotted for comparison among

various configurations.

7.3. Results and Discussion

7.3.1. Experimental Results

As formulated in Equation 7.1, the three main parameters on which the fracture toughness depend are load, crack length delamination, and load point displacement. Load and load point displacement were collected using DAQ system from the MTS machine. DIC was used to track the crack length delamination. All three parameters are plotted against each other, as shown in Figure 7.3, Figure 7.4, and Figure 7.5. The crosshead displacement with the load applied is shown in Figure 7.3. This graph is initially seen to be linear elastic in nature, imitating a tensile curve. After the load reaches certain value, there is a huge dip in the curve, indicating crack initiation. There are zigzag patterns following this dip, indicating an unstable crack propagation. This is usually the type of crack growth expected to be seen in composites (Boroujeni & Al-Haik, 2019). On the contrary, a stable crack propagation exhibits smooth load decay with the crosshead movement.

While comparing the load-displacement curves of various configurations in Figure 7.3, the 105 μm showed a delayed load dip at 4.5 mm crosshead displacement, compared to 2.4 mm crosshead displacement of the Desized sample. The load dip of 53 μm also shifted slightly right. This shows that, patterning could delay crack initiation. The load where the crack initiates can be seen to be very low at 45 N for Full CNTs, compared to 86 N for the Desized samples. This can be attributed to the lesser seepage of epoxy into the fiber due

to a uniformly thick CNTs layer between them, leading to less interlaminar strength, resulting in less resistance to crack initiation.

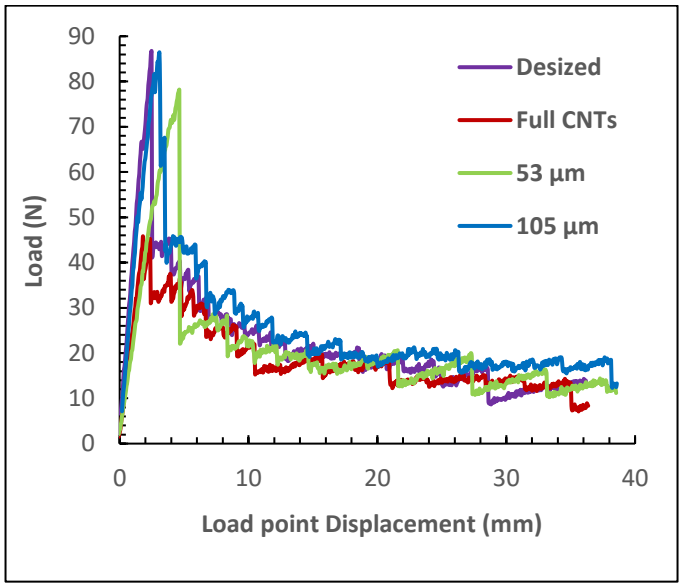

Figure 7.3 Load vs. Load point displacement for the different composite configurations.

The crack growth behavior is compared against load and load point displacement in Figure 7.4 and Figure 7.5 respectively. The load initially increases with the crack length, till it reaches the end of PTFE insert, then slowly drops with increasing crack length as the crack propagates, as a general trend seen in Figure 7.4. Although the graph might give a wrong impression of all the points converging, the points for 53 µm, and 105 µm are shifted rightward at higher crack length values when inspected closely. This shows evidence of fiber bridging energy dissipation. The patches of CNTs act as bridge reinforcements, offering a zigzag path, instead of a straight path for during crack propagation. This provides more resistance, and hence requires higher loads for the crack to propagate.

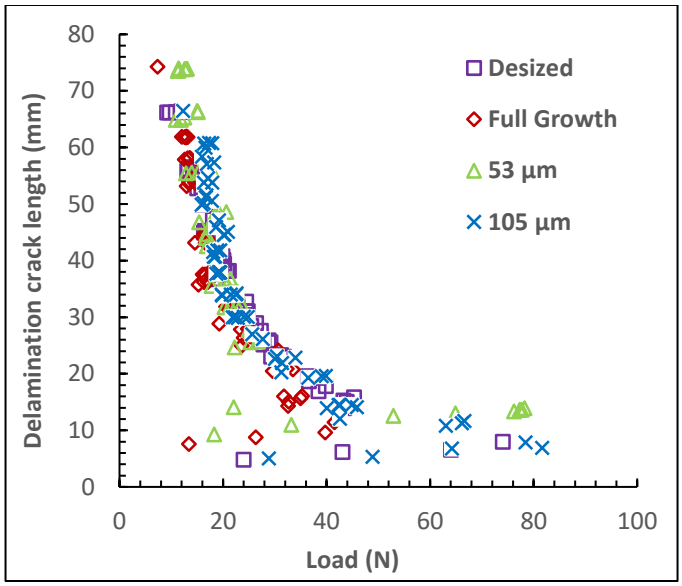

Figure 7.4 Delamination crack length vs. load for the different composite configurations.

From Figure 7.5, it can be inferred that at identical load point displacements, the crack length in the 105 µm configuration is much lower than the rest of the configurations. This is evident by its lower slope values. This means that the rate of crack growth in 105 µm hybrid configuration is much lower than the others. The highest rate is seen in 53 µm, and Desized configurations. This shows 105 µm patterning is more efficient for crack propagation providing both resistance to crack growth and slowing the rate of crack growth.

The calculated values for fracture toughness of each configuration are shown from Figure 7.6 to Figure 7.9. These are also called representative crack resistance curves (R-curves). In unidirectional composites, these plots start at a much lower value, and then slowly increases to form a plateau. The initial value is considered G_{IC} for crack initiation, and the other values are the G_{IC} for crack growth. During crack growth, it encounters various types of regions like matrix-

rich regions, CNTs patches, fiber/matrix regions, among others. Each region has a different energy dissipation mechanism during the crack growth. These different mechanisms result in an R-curve in the form of a plateau, as seen in figures below. The average of two samples in each configuration was calculated to plot the curves in Figure 7.10.

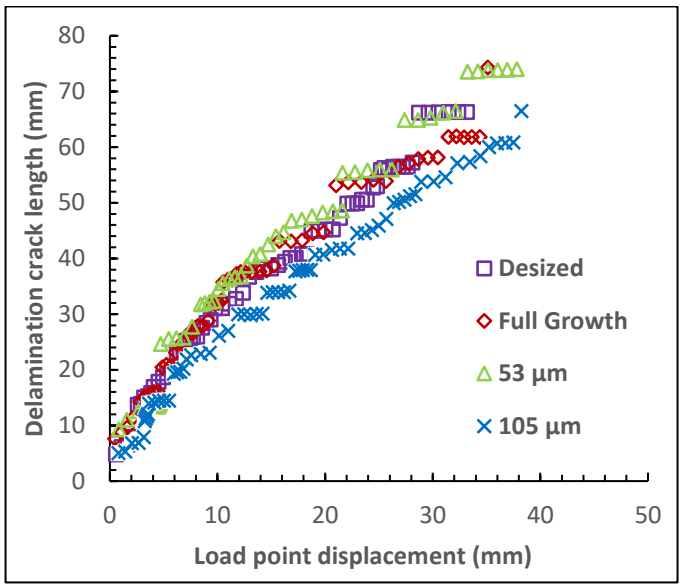

Figure 7.5 Delamination crack length vs. load point displacement for the different composite configurations.

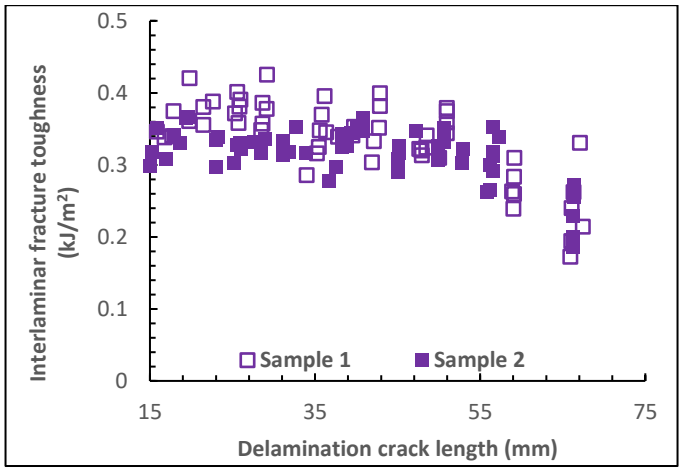

Figure 7.6 Fracture toughness vs. delamination crack length for Desized composite configuration.

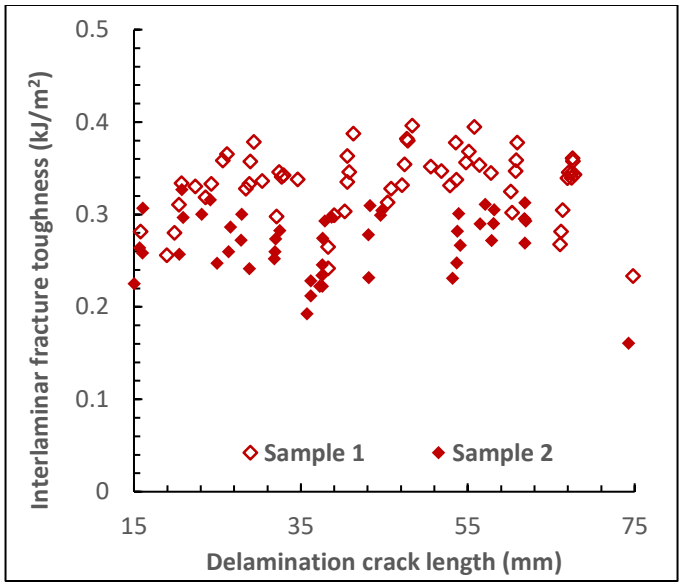

Figure 7.7 Fracture toughness vs. delamination crack length for Full Growth composite configuration.

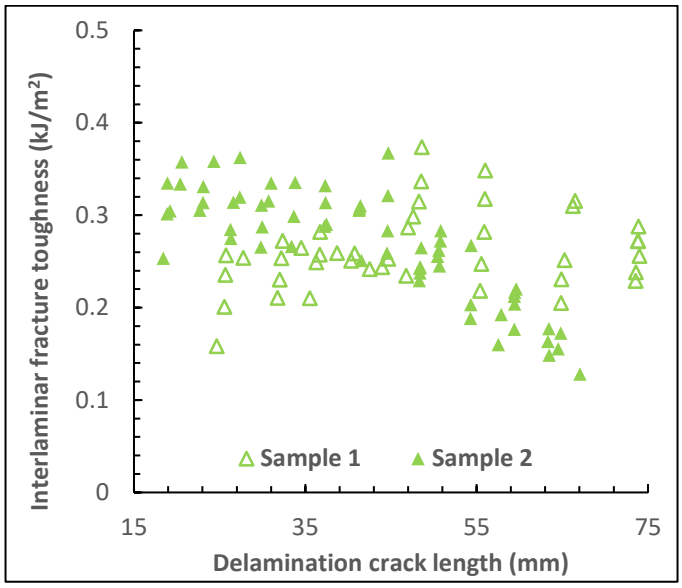

Figure 7.8 Fracture toughness vs. delamination crack length for 53 µm composite configuration.

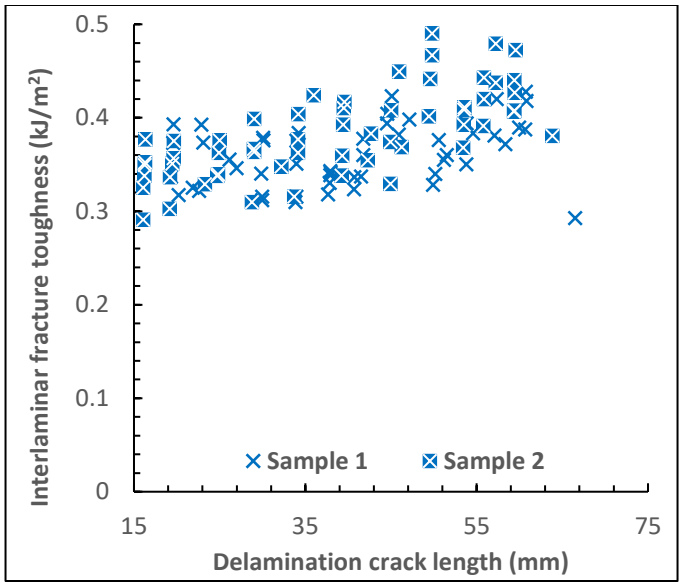

Figure 7.9 Fracture toughness vs. delamination crack length for 105 µm composite configuration.

From Figure 7.10, the G_{IC} at crack initiation in the increasing order is: Full Growth, Desized, 105 µm, and 53 µm. This result follows the behavior seen in the load vs. displacement curves in Figure 7.3, as anticipated. In conclusion, it can be inferred that, while 105 µm patterned CNTs aided in delayed crack initiation, and propagation, 53 µm patterned CNTs aided only in delayed crack initiation. Full Growth of CNTs resulted in worse crack initiation and propagation properties when compared to the Desized samples. Hence, patterning played a significant role in improving fracture toughness of these hybrid composites.

7.3.2. Simulation Results

Delamination using ANSYS was performed using CZM and VCCT procedures. These results are comparable to the experimental crack propagation results discussed in Section 7.3.1. So, similar parameters were calculated and

plotted for comparison.

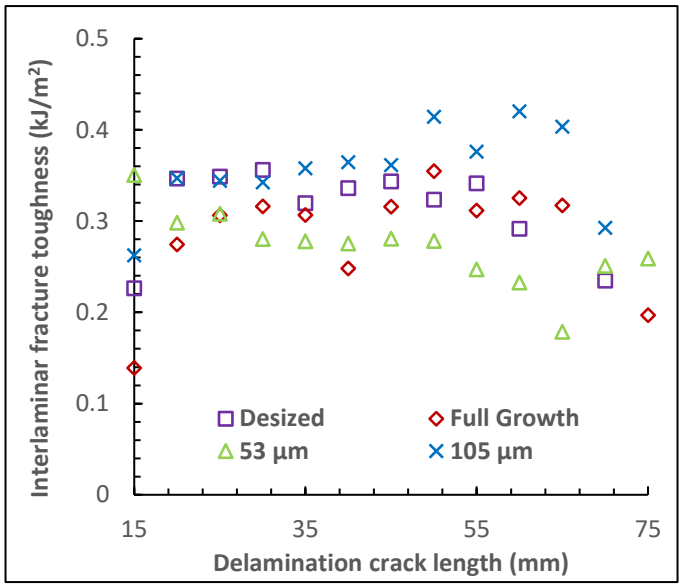

Figure 7.10 Average fracture toughness comparison for all configurations.

7.3.2.1. CZM Simulation Results

Load, crack length delamination, and load point displacement are plotted against each other from Figure 7.11 to Figure 7.13, similar to the experimental plots. Figure 7.11 decays smoothly, compared to the experimental plot showed in Figure 7.3. This shows that the CZM simulation does not capture the unstable crack propagation, while using an orthotropic model. This plot indicates that a stable crack propagation since the load rises to a certain value, and decays slowly to reach an asymptotic value. This is due to the introduction of a cohesive layer at the mid-layer in the model (equivalent to PTFE layer between top 5 layers and bottom 5 layers in the experiment), seen in Figure 7.2. The crack propagates as the stiffness of this cohesive layer drops in CZM analysis. This drop in stiffness is gradual and uniform, hence resulting in stable crack propagation.

However, both Figure 7.11 and Figure 7.12 show that 105 µm performs

better both during crack initiation, and propagation. This can be inferred by its high crack initiation load in Figure 7.11 and the rightward shift of the plot in Figure 7.12. The Full Growth and 53 µm samples are seen to perform worse than the Desized samples.

Figure 7.13 shows a linear relationship between delamination crack length and load point displacement. This behavior is anticipated due to the setup of the CZM simulation. Since the crack propagation is assumed to be stable, the relation between these two parameters is linear and irrelevant of the input material properties.

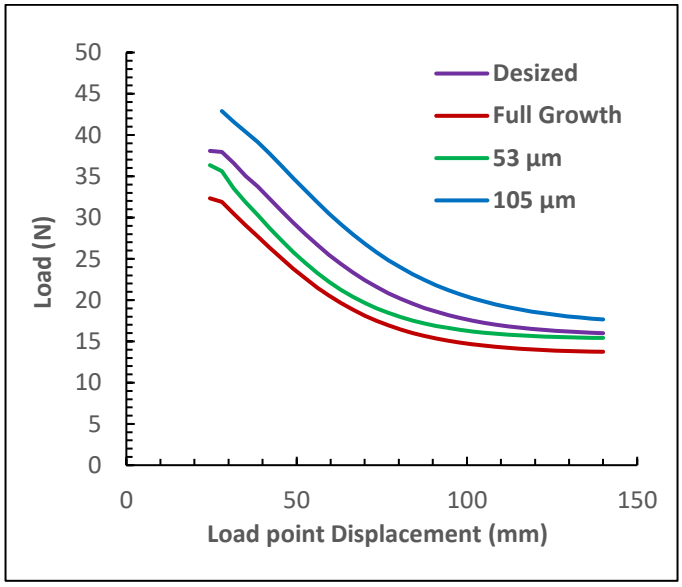

Figure 7.11 ANSYS model prediction of the load vs. load point Displacement using CZM for the different composite configurations.

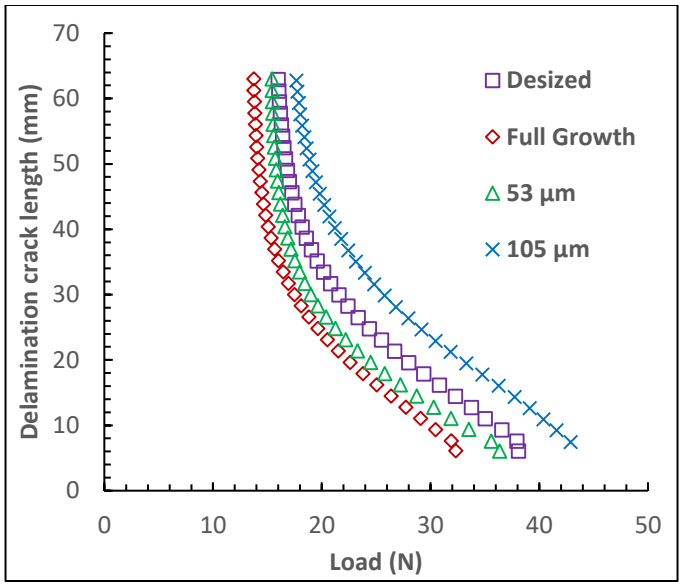

Figure 7.12 ANSYS model prediction of the delamination crack length vs. load using CZM for the different composite configurations.

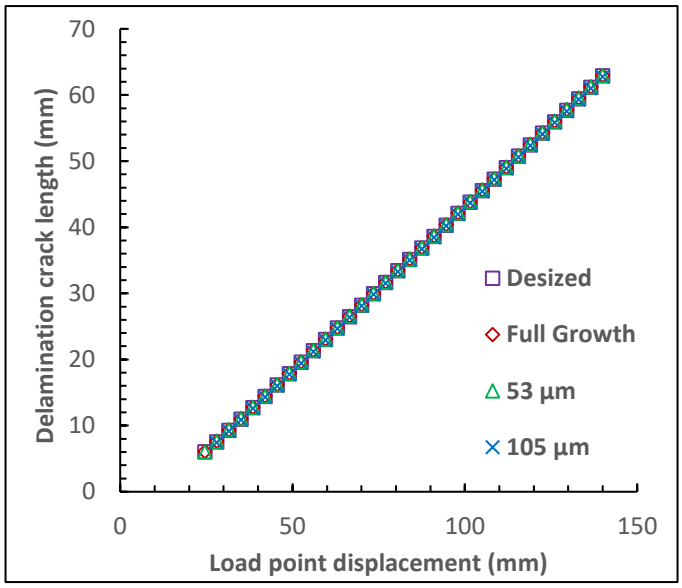

Figure 7.13 Delamination crack length vs. load point displacement using CZM for the different composite configurations.

Figure 7.14 plots the representative crack resistance curves (R-curves) for all the configurations calculated using the results from CZM simulations. These plot results agree with the results inferred before from the previous three figures, as

they are showing better crack initiation and propagation in 105 µm composite configuration, and degraded performance in Full Growth, and 53 µm samples, in comparison to the Desized sample. Though 105 µm and Full Growth sample behavior agrees with the experimental results, 53 µm is an anomaly in the CZM experiment. This might be due to the low average of the resulting G_{IC} values from the plot Figure 7.10, which was the input into the CZM simulation. Though this configuration showed significant improvement in G_{IC} required for crack initiation, the patterned patches of CNTs could not assist as much in the crack propagation, hence reducing the average G_{IC} values. Since this effect cannot be captured in an orthotropic model with no individual components for fiber, epoxy or CNTs, this result is expected.

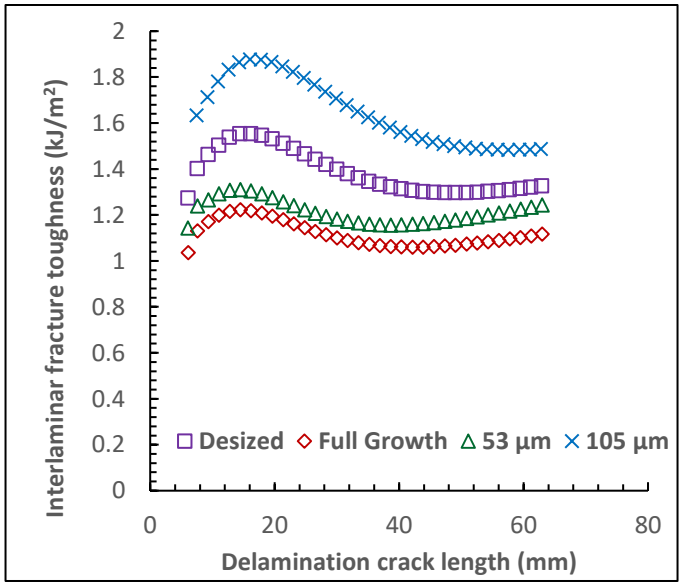

Figure 7.14 Fracture toughness comparison for all composite configurations using cohesive zone modeling (CZM).

7.3.2.2. VCCT Simulation Results

Load, crack length delamination, and load point displacement are plotted

against in each other from Figure 7.15 to Figure 7.17, like the experimental plots. Unlike CZM plots seen in Figure 7.11, the plots seen in Figure 7.15 show an unstable crack propagation. This agrees with the behavior seen in the experimental plots in Figure 7.3. The load is initially seen to rise and then fall, after crack initiation. This is followed by load oscillations during crack propagation. Crack propagation in VCCT analysis occurs when the energy at the crack tip reaches the critical energy release rate value given as an input parameter. Since this is the theory behind experimental crack propagation, the two curves are expected to correlate with each other.

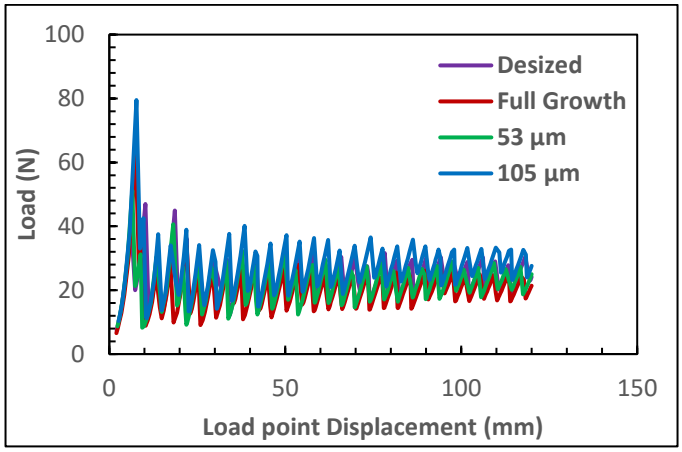

Figure 7.15 ANSYS model prediction of the load vs. load point displacement using VCCT for the different composite configurations.

When comparing the different composite configurations, both Figure 7.15 and Figure 7.16 show an identical trend to that seen in CZM simulations: 105 µm, Desized, 53 µm and Full Growth, arranged in a decreasing order of desirable crack initiation and propagation properties. Figure 7.17 shows a linear relationship between delamination crack length and load point displacement, similar to the CZM behavior. However, due to the unstable crack behavior in

VCCT, the plots show a zigzag behavior.

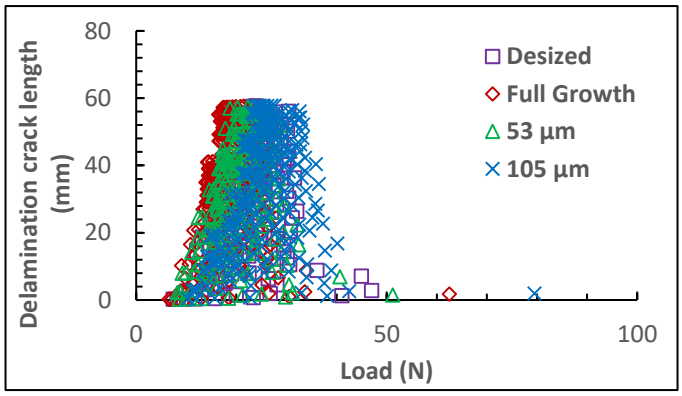

Figure 7.16 ANSYS model prediction of the delamination crack length vs. load using VCCT for the different composite configurations.

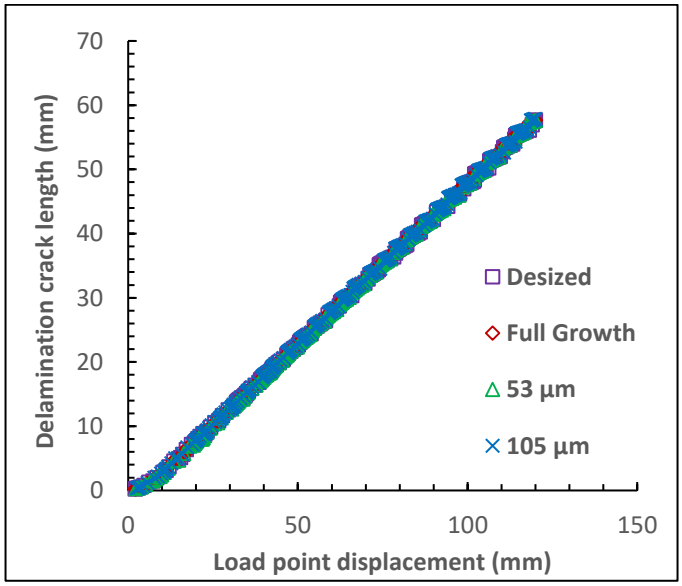

Figure 7.17 ANSYS model prediction of the delamination crack length vs. load point displacement using VCCT for the different composite configurations.

Figure 7.18 shows the representative crack resistance curves (R-curves) for all the configurations calculated using the results from VCCT simulations. The G_{IC} starts at a low value, and seen to increase with the crack length, during propagation. This behavior was also observed in the experimental results. The comparison among various configurations agrees with the previously inferred

behavior. 105 µm sample provides good resistance during crack initiation and propagation. Though majority of the 53 µm sample G_{IC} values lie below the Desized values, some values overlapped/ better between 0- and 45-mm crack length. This is due to the overlapping regions seen in the load-displacement curves of Desized and 53 µm samples in Figure 7.15. This shows that VCCT is better at capturing crack initiation parameters, compared to CZM, since this behavior correlates to the behavior seen in the experimental results.

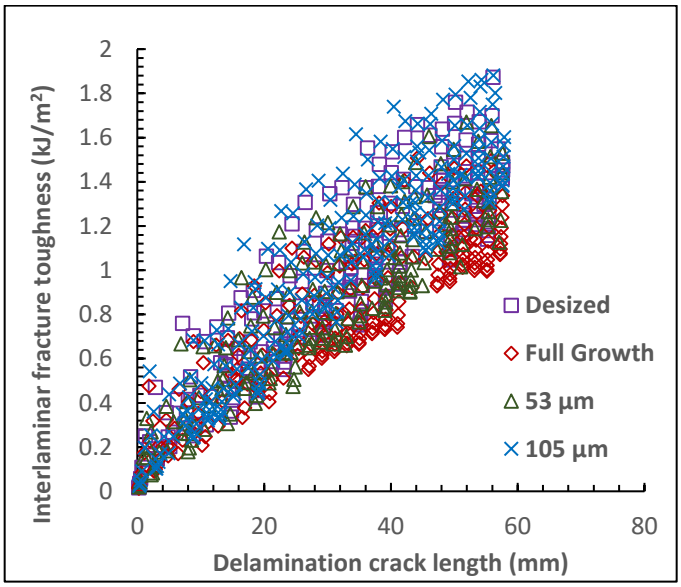

Figure 7.18 Comparison of the ANSYS model prediction of the fracture toughness for all composite configurations using VCCT.

7.3.3. Comparison of Experiments and Models

This section provides a numerical comparison of G_{IC} values calculated from experiment, CZM and VCCT. These three curves from Desized, Full Growth, 53 µm, and 105 µm are shown in Figure 7.19, Figure 7.20, Figure 7.21, and Figure 7.22 respectively. In Figure 7.19, CZM prediction and the experimental results follow an identical trend; the G_{IC} values initially increased, and then decay with

the increase in crack length. This is not the case with VCCT values. The G_{IC} values are increasing with crack length, imitating a unidirectional composite behavior. The absolute values in simulations are higher than the ones calculated using experiments. This is anticipated due to the simplifications made during modeling. The following figures could be understood in a similar manner.

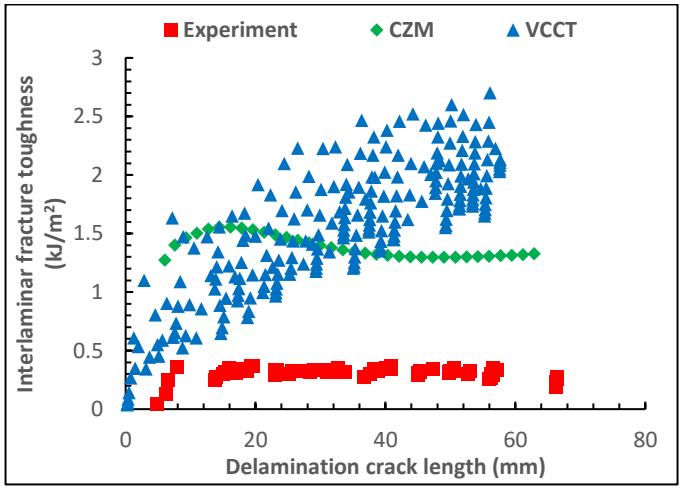

Figure 7.19 Simulation and experimental R curve comparison for Desized composite configuration.

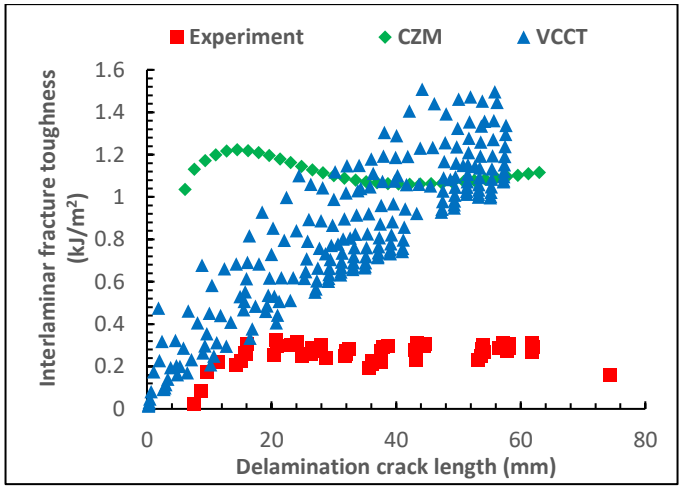

Figure 7.20 Simulation and experimental R curve comparison for Full Growth composite configuration.

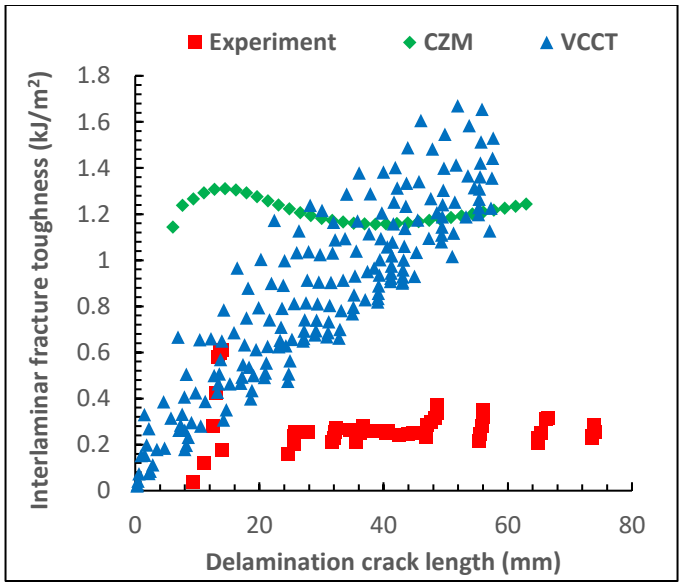

Figure 7.21 Simulation and experimental R curve comparison for 53 μm patterned composite configuration.

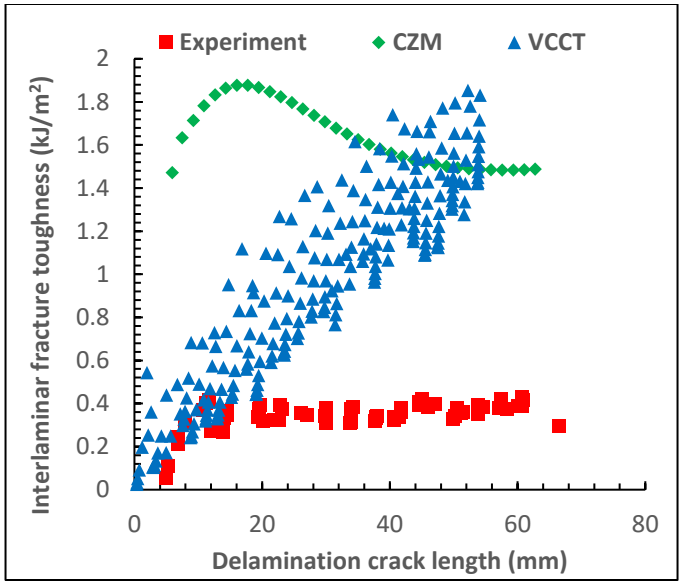

Figure 7.22 Simulation and experimental R curve comparison for 105 μm patterned composite configuration.

8. Experiment with MOFs Based Surface Modifications

In this chapter, all the experiments and results pertaining to hybrid composites fabricated by modifying carbon fiber surface using MOFs are discussed. Various composite configurations, fabrication techniques and testing procedures involved were discussed in detail.

8.1. Composite Configurations and Fabrication

Four different composites were fabricated based on the (i) reference fibers, (ii) acid-treated fibers, (iii) metal organic frameworks (MOFs) modified fibers and (iv) fibers with surface-grown CNTs. In this investigation, MOFs were utilized to modify the surface of structural carbon fibers toward amplifying the interfacial properties of CFRPs. Also, the possibility of utilizing the nickel-based MOFs as a catalyst to grow CNTs on the carbon fibers was explored. Different mechanical and microstructural techniques were implemented to reveal the microstructure and the performance of these surface treatments.

The carbon fibers utilized were desized plain-woven structural polyacrylonitrile (PAN) grade, Thornel-650 (Cytec, Inc.), with 3k bundles. The fibers were desized by placing them in a quartz tube furnace at 550 °C for 30 mins under a nitrogen inert environment. To allow the formation of active sites (-COOH), the fibers were cut into 6″ ×6″ squares and were treated in a diluted mix of DI water/HNO_3 acid. The fibers were washed thoroughly with DI water till a pH of 7.0 was achieved, then they were placed in a drying oven of 80 °C for 24 hours.

To prepare the MOFs mixture, one solution was made by dissolving the

metal ion source; nickel nitrate hexahydrates ($Ni(NO_3)_2 \cdot 6H_2O$, Sigma Aldrich Co.) in methanol. The ligands solution was made by dissolving 2-methylimidazole ($C_4H_6N_2$, Sigma Aldrich Co,) in methanol. Each solution was magnetically stirred, separately, at 400 rpm for 6 hours, then the two solutions were magnetically stirred together for 10 minutes. A single carbon fiber cloth was immersed in the solution for 24 hours while suspended to allow MOFs deposition on both surfaces. The carbon fiber cloth was removed from the solution and washed repeatedly with ethanol then left to dry in an oven at 100 °C for 24 hours.

All the four configurations of carbon fiber were visually inspected using scanning electron microscopy. Energy-dispersive X-ray spectroscopy (EDS) was also used to study the material composition. De-sizing the T650 fibers under inert thermal environment was a success as evidenced by the peel off on the fiber surface shown in Figure 8.1. Treating the fibers with the diluted HNO_3 solution dissolved these desized peels as seen in Figure 8.2; nitric acid is well known for introducing the carboxylic group (-COOH) to the fibers surface (Rahmani et al., 2016). The acid treatment also plays an etching effect revealing several fibrils at the surface of the carbon fiber.

Very organized MOFs porous structures emerged upon utilizing high concentration solution of the metal source as can be seen in Figure 8.3. The pores are separated by very thin sheet walls of the MOFs as can be seen in the inset in Figure 8.3. Dense concentration of microscale spherical MOFs cages were observed to precipitate on the carbon fibers. These cages were a result of

insufficient stirring of the metal initial salt where large crystals of the metal salts if not dissolved become a substrate on their own leading to an array growth of MOFs cages which was reported by other studies as well (Zhong et al., 2020).

It is worth mentioning that, while published literature displayed the presence of these thin MOFs sheets, they lacked the ordered pattern presented herein. Some of the patterns reported are solid cubical cages (Aslam et al., 2017), nanobelts (Bao et al., 2019) and microspheres (Zhong et al., 2020). Several factors play roles in the formation of the different patterns of the MOFs such as the metal source concentration, the ligand utilized, the growth time and the nature of the substrate. For example, upon reducing the metal seeding solution concentration by 50%, and upon following the same protocol it was clear from Figure 8.4 that the well-defined thin sheet walls have vanished. As shown in Figure 8.5, the energy-dispersive X-ray spectroscopy (EDS) of the carbon fibers with MOFs revealed strong peaks of crystalline nickel.

Utilizing MOFs as catalysts to grow CNTs is one of the pillars of the current investigation. As shown in Figure 8.6, The dense MOFs lead to dense CNTs growth that enlarged the fibers diameter from 6.8 μm, as reported by the manufacturer, to almost 30.0 μm. Such dense growth can hinder the resin ability to wet the fibers and penetrate through the bundles. The fibers with MOFs grown via lower seeding solution concentration yielded more uniform and less dense growth of CNTs as shown in Figure 8.7. Such growth, from previous experience, allows for better flow of the epoxy in between the fibers.

The EDS was carried out after the CNTs growth, shown in Figure 8.8

indicates that the carbon peak became stronger because of the added CNTs atoms. Identically, the Ni spots became clearer since the reduction process prior to the CNTs growth assisted in removing oxides that might have been developed during the MOFs deposition.

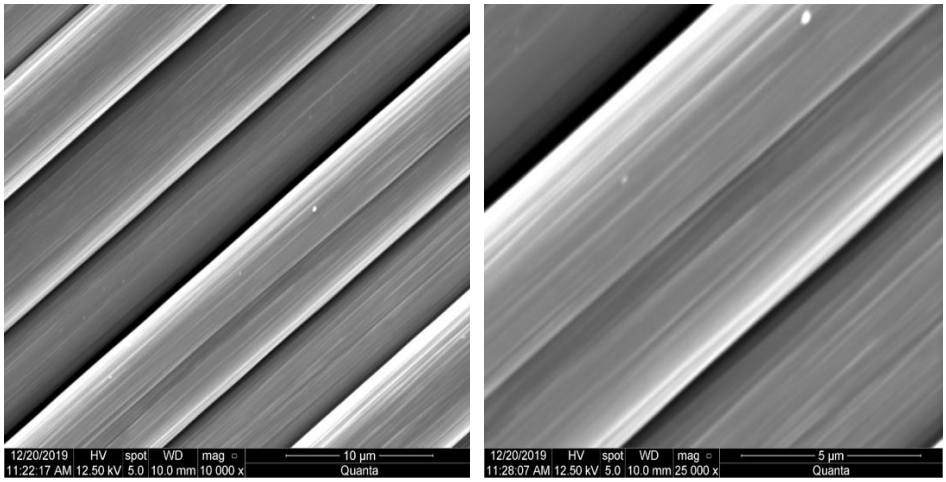

Figure 8.1 SEM micrograph of the Desized carbon fiber at different magnifications.

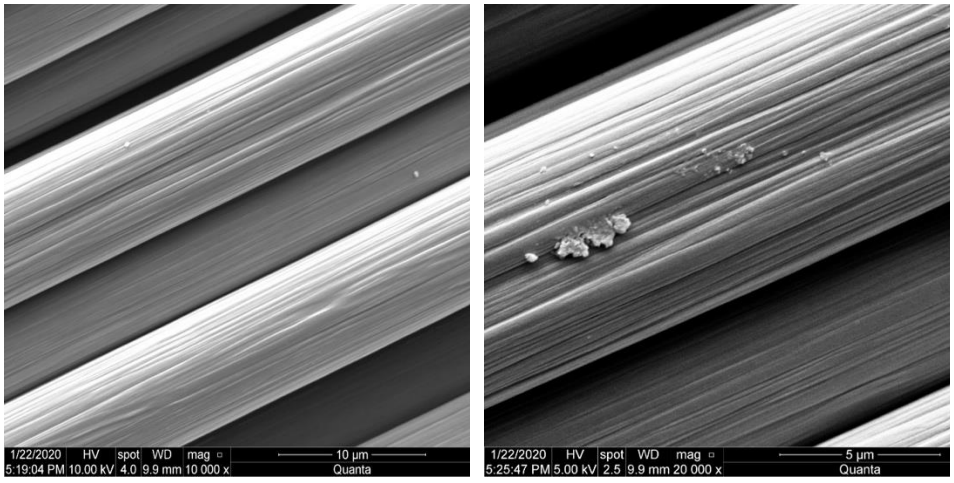

Figure 8.2 SEM micrograph of the carbon fiber seen after etching with acid.

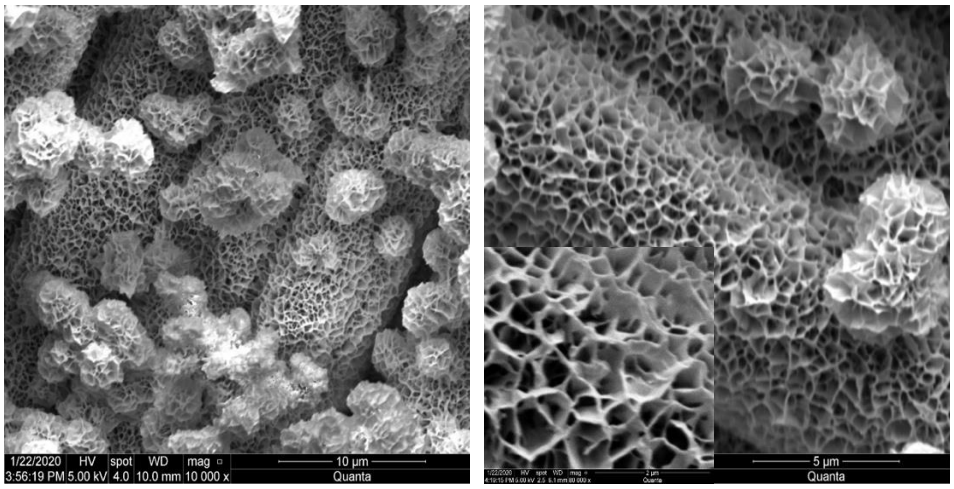

Figure 8.3 SEM micrograph of the carbon fiber showing MOF walls grown with high chemical concentrations in growth solution.

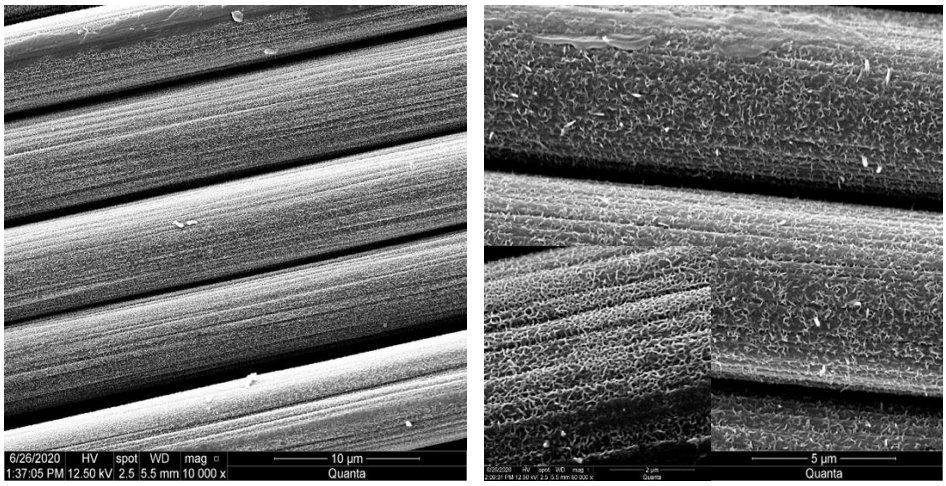

Figure 8.4 SEM micrograph of the carbon fiber showing MOF walls grown with lower chemical concentrations in growth solution.

Each composite in this experiment comprised two plies adhered by an epoxy matrix; Epon 862™; (Diglycidyl Ether of Bisphenol-F (Miller Stephenson, Co.) This resin is utilized for structural applications with a high viscosity of 2500-4500 cPs at 25 °C. The curing agent system is Epikure -W™; an aromatic amine (Miller Stephenson, Co.) with a low room temperature viscosity of 100-300 cP. When both the resin and hardener are mixed in a ratio of 100:26.4 by weight, a

viscosity of 2100-2300 cPs and a gelling temperature of 177 °C were reported by the manufacturer. The hand-layup method was employed for lamination. Then the different two-plies laminae were impregnated with epoxy, with fiber to epoxy wight ratio of 60:40, were sealed in a vacuum bag. The four composite laminate configurations were processed using a composite autoclave (Econoclave, ASC Process Systems). A vacuum of 25 torr was maintained in the chamber throughout the curing process. A pressure of 70 psi was achieved by flowing N_2 in the chamber. The autoclave cycle had multiple steps: Isothermal step for 1.0 h at 25 °C, heating to 177 °C, isothermal step for 2.5 h at 177 °C, then cooling down to room temperature.

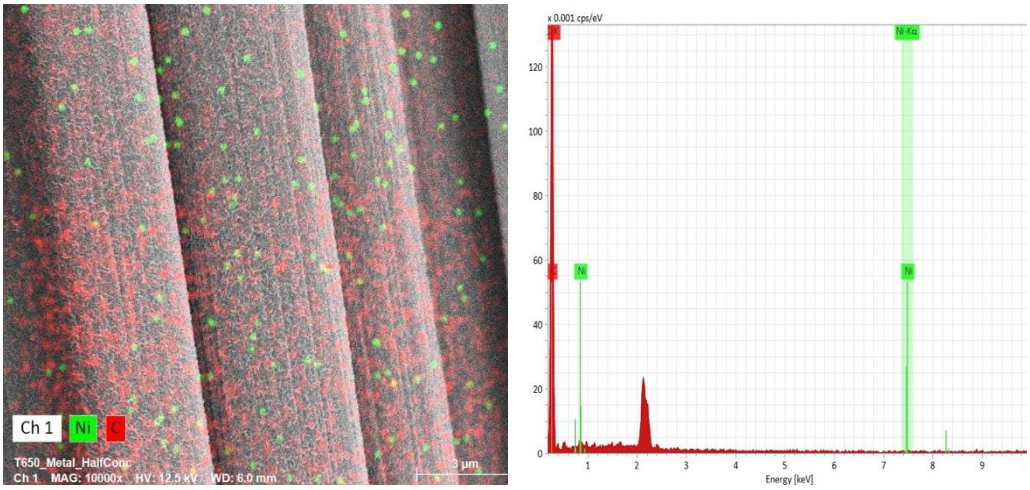

Figure 8.5 EDS analysis of MOF grown carbon fibers a) Material composition showing nickel and carbon as major constituents. b) Spectra showing strong carbon and nickel peaks.

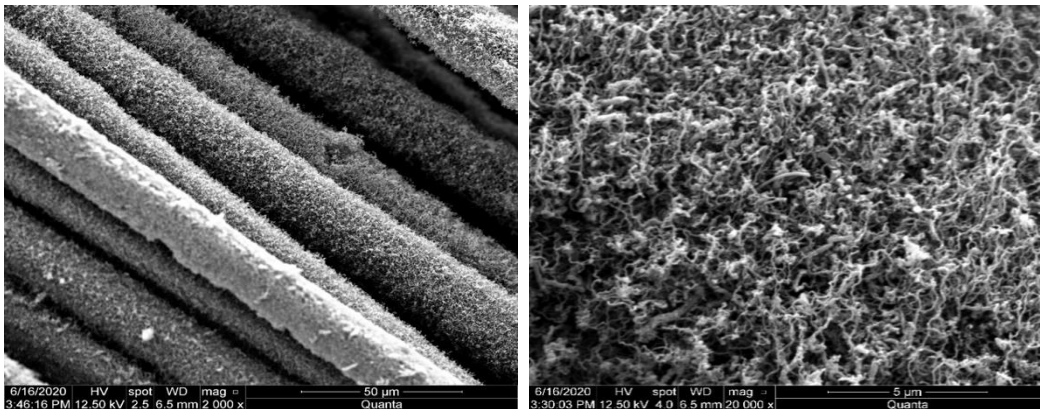

Figure 8.6 SEM micrograph of the CNTs grown using GSD technique utilizing high concentrations of MOF as a catalyst at different magnifications.

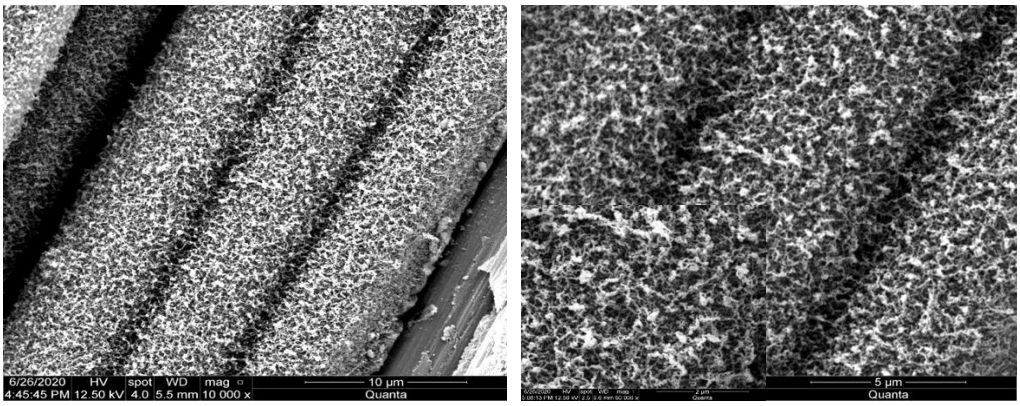

Figure 8.7 SEM micrograph of the CNTs grown using GSD technique using lower concentrations of MOF as a catalyst at different magnifications.

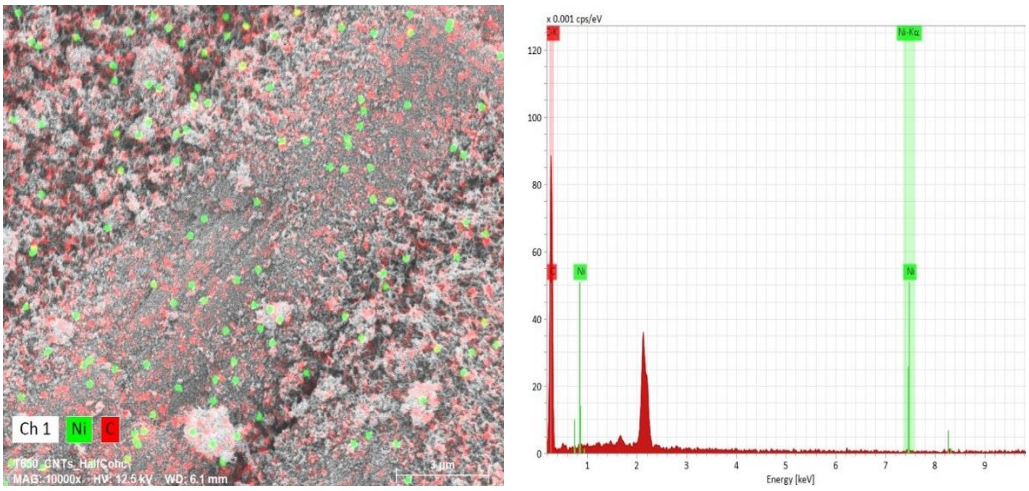

Figure 8.8 EDS analysis of CNTs grown on MOF carbon fibers a) Material composition showing nickel and carbon as major constituents. b) Spectra showing strong carbon and nickel peaks.

8.2. Mechanical Testing Procedures

Various mechanical and material characterization techniques were used in each of the experiments described above. The purpose, procedure, and the equipment involved in each of them was discussed in detail in this section.

8.2.1. Stiffness and Strength

Tensile tests were carried out following the D3039 ASTM standard (1995). The tensile coupons were cut to a dimension of 12.7 x 1.27 cm and, adhered with G-10 glass fiber based composite tabs using the same epoxy blend used for making the plates in autoclave. Tensile testing was performed using MTS Criterion^{TM} Model 43 machine. Strain was measured using a 25.4 mm gauge length extensometer, connected to the MTS controller for real-time data acquisition. These coupons were then mounted in-between the crosshead grips to be pulled until failure, at the rate of 1.0 mm/min. Each configuration had a minimum of eight tensile coupons. The test data was then averaged for results.

8.2.2. Lap Shear Test

The sample is gripped at both ends in the grips, like a tensile sample. However, it is loaded at higher rates till the adhesive fails at the joint, to mimic a shear force in a real-life situation.

In the current work, to examine the effect of the fibers' surface treatment on their adhesion to the epoxy, four different sets of composites samples were prepared following the ASTM -D5868 standard (2014) for shear lap adhesion test in FRPs. Each specimen comprised eight laminates to acquire the thickness recommended in the standard. While the outer six plies were made of reference carbon fibers with no surface treatments, the two intermediate plies at the joint

were based on fibers with different surface treatments; reference, acid treated, MOF and CNTs. For each composite configuration, the layup was such that the two intermediate plies overlap 25.4 mm. The samples were manufactured in the autoclave identical thermal cycle utilized for the preparation of the tensile samples. Upon curing and cutting the composites each sample comprised two joint each with the dimensions of 101.6 mm × 25.4 mm × 0.75 mm. The tow plies at each joint overlapped over an area of 25.4 mm × 25.4 mm. The shear lap samples, individually, were held inside the grips of the MTS testing system, allowing grip separation of 76.2 mm. Each sample was loaded in tension at a constant rate of 13 mm/min until the joint fails. Five samples were tested for each composite configuration.

8.2.3. Damping Properties

For composites fabricated using MOF surface treatments, Dynamic mechanical analysis (DMA) testing was carried out using a DMA8000 analyzer (Perkin Elmer, Inc.) following the ASTM D7028-07 and ASTM D5023-15 (2015; 2015) standard.

Composite coupons of 50.00 mm × 6.25 mm were used and a three-point bending fixture with span of 40 mm was utilized to mount each of the composite samples. In the temperature sweep mode of the DMA, constant frequency of 1.0 Hz was applied, while varying the temperature from 22 to 140 °C at a constant strain of 0.05 %. The frequency sweep test was performed with a frequency range from 1 to 100 Hz scanning at 25 °C using the same strain applied in the temperature sweep test.

8.2.4. Spectroscopy and Microscopy

Spectroscopy is widely used in material science for composition analysis. Each molecule or atom absorb/emit a specific electromagnetic radiation. This helps in the characterizing the presence of any defects or functional groups introduced due to the addition of nanofillers in hybrid CFRPs.

Raman spectroscopy analysis of the modified fibers was carried out utilizing Desktop H-PeakSeekerPro (Raman Systems, Inc) with excitation wavelength of 532 nm and laser power of 100 W. The microstructure of the carbon fibers with different surface treatments was characterized using scanning electron microscopy (SEM, FEI Quanta 650, Thermo Fisher Scientific Co.) equipped with energy-dispersive X-ray spectroscopy (EDS) detector (Bruker, Inc.).

8.3. Results for MOF Surface Treated Hybrid Composites

Various parameters from tensile, shear and DMA analysis for all configurations were plotted and compared against each other. The following sections show a detailed record of all these properties. To probe the effects of the growth patterns further, spectral analysis of fibers of all configurations, and the fracture surface analysis of the tensile samples was also performed.

8.3.1. Spectroscopic Analysis

The Raman spectra for the reference carbon fiber, shown in Figure 8.9 revealed a strong disordered graphitic (D; 1360 cm^{-1}) peak and much weaker ordered graphitic (G; 1580 cm^{-1}) peak. A lesser referred to peak is the A peak roughly at 1500 cm^{-1} which is indicative of amorphous carbon. The T650 being a PAN based fiber, is not highly graphitic and do not exhibit a G band, they

however display a D peak that corresponds to the structural disorder caused by the existence of the sp3 bonds (Fitzer, 1989).

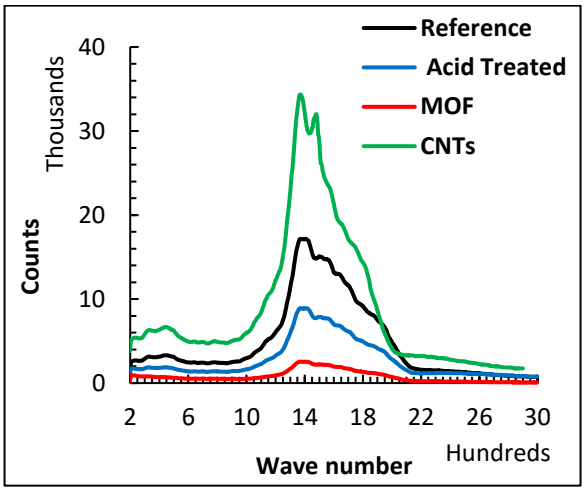

Figure 8.9 Raman spectra of the T650 carbon fibers with different surface treatments.

Upon acid treatment, the intensities of both the D and G band was reduced, also the G band was broadened and shifted to a higher frequency. This shift is attributed to the presence of the -COOH and NH_2 functional groups on the surface (Woodhead et al., 2017). Also, the reduction in the G band intensity is indicative of reduced number of graphitic layers. The change in the ratio of the peak's intensities (I_D/I_G) is indicative of the number of defects sites; the functional groups can be thought of as defects. The deposition of MOFs on the surface of the fiber basically masked the D and G peaks due to the higher coverage of metal crystals and the spectra is just a measure of the absorption of the MOFs.

Indeed, one of the few references on the use of Raman spectroscopy with Ni-based MOF was limited only to analyses of the normal modes of the MOF lattice

vibrations at terahertz (THz) region that corresponds to low wave number region in Raman spectra (Krylov et al., 2017). The suitability of the Raman analysis to carbon fibers coated with MOFs is yet to be determined. Upon growing the CNTs, The CNTs grown on the surfaces of the T650 carbon fiber a strong D-band at 1350 cm^{-1} and G-band at 1595 cm^{-1}, are apparent. The intensity ratio (I_D/I_G) is more noticeable for the carbon fibers with CNTs, revealing a high degree of crystallinity of the CNTs.

8.3.2. Tensile Test Results

Figure 8.10 shows representative tensile test of the different composite configurations, while Figure 8.11 summarizes the axial stiffness and the strengths for the different composites. From both figures it can be observed that all the composite materials exhibited linear elastic behavior and the stiffness for all configurations remained almost unaltered. This is mainly because the stiffness is more of a volumetric property that depends on the core of the fiber rather than its surface. The only configuration to show a slight improvement on the stiffness was that for composites where the fiber is sheathed with CNTs on the surface and that was the only composite where the fibers have been annealed at elevated temperatures which would have sintered the MOF under the CNTs leading to a stiffer phase.

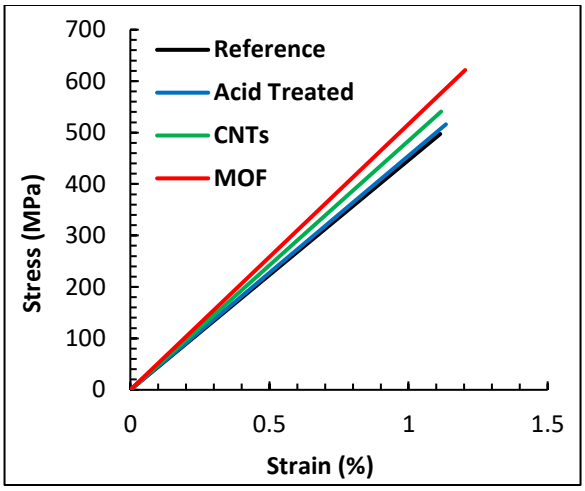

Figure 8.10 Representative tensile tests of the composites based on different fiber surface treatments.

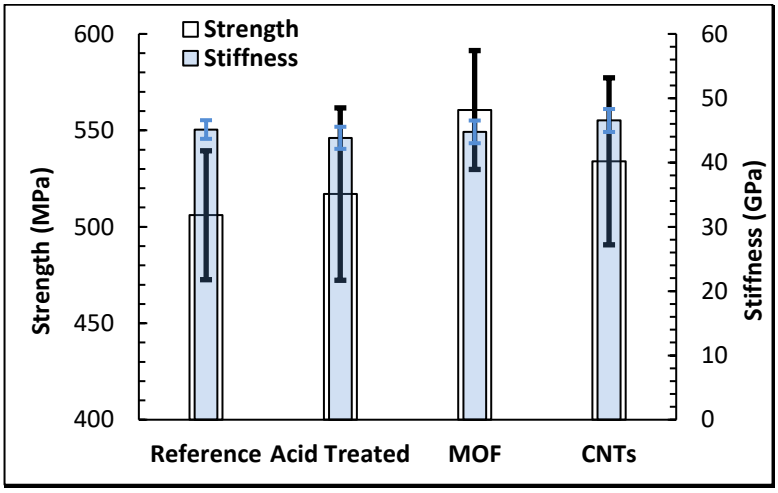

Figure 8.11 The averaged tensile strength and axial stiffness of the composites. Error bars represent the standard deviation.

The strength of the composite increased slightly by 2.1% because of acid treatment. The acid treatment in general increases the surface area of the fiber and enhances the surface functionality. The minute increase here is mostly because of relatively low concentration of acid (30%) used when compared to the 60-100% typically utilized to induce significant surface oxidation and noticeable increase in the surface area (Shim et al., 2001; Wu et al., 2004). The

choice of the low concentration was mostly to control the density of MOFs growth in the next steps. It is worth mentioning that some of the previous work of MOFs nanosheets with carbon fiber also indicated a reduction of the strength of the carbon fiber itself due to the acid etching (Y. Li et al., 2020; X. Yang et al., 2017), attributing the damage to the fiber induced by etching as the main cause for strength reduction. This damage was manifested by the decay of the intensity and the broadening in the Raman spectra compared to the reference fiber in Figure 8.9. Growing the MOFs on the surface of the fiber improved the strength by 11.0 %. The MOFs play significant role in increasing the surface area and providing anchoring between the fiber and the matrix.

It was hypothesized that the defects induced by the acid etching are now filled with MOFs, as the -COOH group induced by the acid etching and the ligand in the MOFs play a role in anchoring the Ni-MOF structure to the activated sites on the surface of the carbon fiber. These MOFs assist in better load transition from the matrix to the fiber and better load distribution on the fiber surface, increasing the load bearing capacity and thus enhanced strength. Earlier literature suggested that the fiber themselves become stronger when coated with Zirconia-based or Zinc-based MOFs after functionalizing the fibers with -COOH or NH_2 groups through acid treatment (Y. Li et al., 2020; X. Yang et al., 2017).

Growing CNTs utilizing the Ni-MOFs as catalyst improved the strength of the composite by 5.5%. The increase is less than that for the MOFs because the elevated temperature of the CNTs growth induce some damage to the carbon

fiber on top of the damage it has encountered due to acid treatment. Growing CNTs uniformly on the carbon fiber typically leads to moderate increase in the strength as the dense growth of the CNTs limits the impregnation (wetting) of the epoxy into this dense CNTs layer to reach the base carbon fiber which is crucial for improving the mechanical properties.

A possible theory is that having the MOFs layer beneath the CNTs film still contributes to the improvement on the strength. In Chapter 5, CNTs were grown on identical T-650 carbon fiber. However, the Ni catalyst was deposited as uniform smooth film via magnetron sputtering rather than porous honeycomb film obtained by the MOFs chemistry. In that investigation it was observed that only 3.0% improvement on the strength. Hence, the morphology of the MOFs could have attributed to the better improvement of the composite based on fibers with CNTs when the MOFs is deposited as the catalyst.

For both the composites based on MOFs and CNTs, the composite exhibited little or no cracks in between the fiber, suggesting that the patterned deposition of the MOFs, and the consequent CNTs growth, promoted mechanical interlocking mechanism between the growth species and the epoxy matrix constituting a strong impediment that suppressed crack propagation and thus, resulting in enhanced strength.

8.3.3. Dynamic Mechanical Analysis (DMA) Results

The DMA frequency sweep results are shown in Figure 8.12 in terms of the damping parameter tan (δ). To understand these results it is crucial to consider several parameters that affect the damping capacity of FRPs such as interfacial

bonding, stick-slip friction, and nano fillers additives (Tang & Yan, 2018). Eventually the FRPs based on the reference untreated carbon fibers achieved the lowest damping parameter. The composite based on the fibers functionalized with nitric acid showed an improvement in damping by as much as 200 % at 87 Hz since the diluted acid treatment enhanced the surface area of the carbon fiber, evident by fibril like striation on the surface, allowing for larger contact with the epoxy and hence larger energy dissipation. Furthermore, the weakened graphitic outer layers of the fiber could have also promoted the stick-slip mechanism the fiber matrix interface. The addition of the MOFs to the fiber surface increases the surface area even further and the weak epoxy-metal interfacial bonding allows for more energy dissipation and thus the damping parameter increased as much as 500 % over the composite based on the reference fiber.

The growth of CNTs on top of the surface of the carbon fibers increases the surface area tremendously due to the high aspect ratio of the CNTs. This new added interface area allows for significant friction between the CNTs and the epoxy leading to significant energy dissipation. Furthermore, from the tensile tests, it was evident that the presence of the CNTs at the interface allows for a better stiffness which is consistent with the hypothesis of sliding at the CNTs/matrix interface (Tang & Yan, 2018). The combination of all these attributes allowed the composite with CNTs to attain an improvement of the damping coefficient by 425 %.

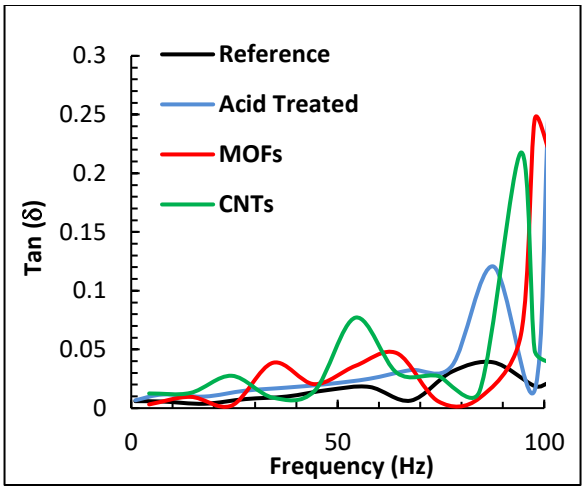

Figure 8.12 The DMA measurements of the damping parameter; tan (δ) for the different composites' configurations via frequency sweep at room temperature.

The DMA analysis can also shed some light to how the different fiber's surface treatment can affect the glass transition of the FRP as shown in Figure 8.13. One measure of the glass transition temperature, T_g, is the peak of tan (δ) curves (Bussu & Lazzeri, 2006; Goertzen & Kessler, 2006). From Figure 8.13, the T_g for the composite based on the reference sample is about 120°C and is increasing to 140°C and 150°C with the surface treatments with MOF and CNTs, respectively. No change was observed for the composites based on acid treated fibers.

The results suggest that the interface between the fiber and matrix play crucial role in the shift of the glass transition. Both the MOF and the CNTs constitutes obstacles that could entrap the epoxy. During glass transition, the epoxy molecular chains absorb heating energy and start moving. However, having the MOF and CNTs on the surface of the fiber slow if not diminish such molecular movement, thus, more energy (and higher temperature) is needed to overcome these nanoscale hurdles. Although the glass transition is an intrinsic

property of the polymer matrix, it is clearly affected by the fiber presence and the fiber's surface treatment.

A previous investigation (Bussu & Lazzeri, 2006) suggested that the mere presence of the fibers does not affect the T_g along the fiber direction and slight reduction on the fiber's transverse directions. This indirectly correlates the T_g to the strength and stiffness, as these properties reach their maximum along the fiber direction and attain their minimum values at the transverse direction. In support of this hypothesis, another investigation found that increasing the fiber volume fraction, hence the strength and stiffness, in an epoxy could increase the glass transition by as much as 25 °C (Dong & Gauvin, 1993). Thus, the results of the current study suggest that the measurement of T_g could offer a venue to qualitatively probe the effects of fiber surface treatment on the mechanical performance of epoxy-based composites.

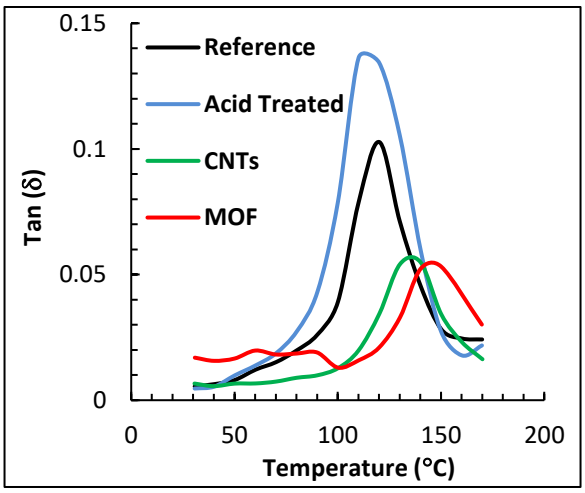

Figure 8.13 DMA temperature sweep for composites based on reference, acid treated, MOF modified and CNTs growth carbon fibers. Measurements conducted at a frequency of 1.0 Hz.

8.3.4. Shear Lap Test Results

Figure 8.14 shows representative strength-displacement curves for the four different composites single-lap bonded joints while Figure 8.15 summarizes the average joint shear strengths. The composites based on the reference fibers exhibited the lowest joint shear strength. To classify the failure mode of the joints, the joint area after failure was examined consulting the ASTM standard D5573 (2019). Figure 8.16.(a) shows that the composite based on the reference fibers exhibited a stock-break failure as the sample broke outside the joint area. The acid treatment of the fiber improved the adhesion shear strength by 10%. This increase is attributed to the enhanced surface roughness of the fiber due to the acid induced roughening of the carbon fibers.

The sample based on the acid treated fibers displayed a cohesive failure evident by Figure 8.16.(b) as the adhesive layer separated such that its residue appeared at both surfaces of the joint. It was believed that for carbon fibers oxidized via nitric acid treatments, it is the surface functionality rather than the increase in surface area that is responsible for improvements of the shear strength (Brooks et al., 1974). In particular, the number of the bonds per unit length formed between the resin molecules and the surface groups induced by acid treatment on the surface of the carbon fibers rather than the concentration of the bonds or the surface area is responsible for such improvement.

The composite based on fibers with MOF displayed a remarkable improvement in the adhesive joint shear strength; 40 %. The nanosheet structures of the MOFs are responsible for this improvement through furnishing an extended contact area and a mechanical interlocking of the epoxy between the

MOF pores. This sample displayed a fiber-tear failure as the failure resulted in the appearance of reinforcing fibers on both ruptured surfaces as shown in Figure 8.16.(c), the tearing of the fibers within the joint is indicative of significant shear bearing capability. Finally, for the composite based on carbon fiber with surface grown CNTs the shear lap strength improvement was minute and was limited to 4.4%.

By examining Figure 8.16.(d), it seems that the epoxy did not wet the CNTs well, despite the elevated pressure in the autoclave, due to the dense growth of the CNTs. This resulted in a thin-layer cohesive failure where some adhesive dusting can be seen on one of the joint surfaces and a thicker layer on the opposite surface. Previous work (Hsiao et al., 2003) suggested that for a shear lap test, the CNTs contribute better improvements to the FRPs when a surfactant is utilized to activate them prior to their dispersion in the epoxy matrix to form a better adhesive paste.

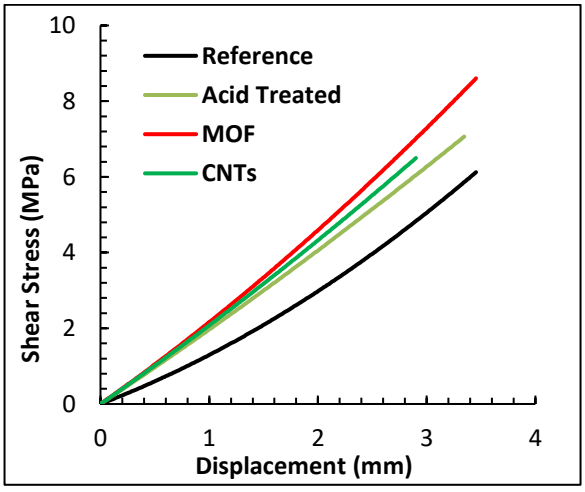

Figure 8.14 Representative shear lap joint stress vs. displacement for the different composite configurations.

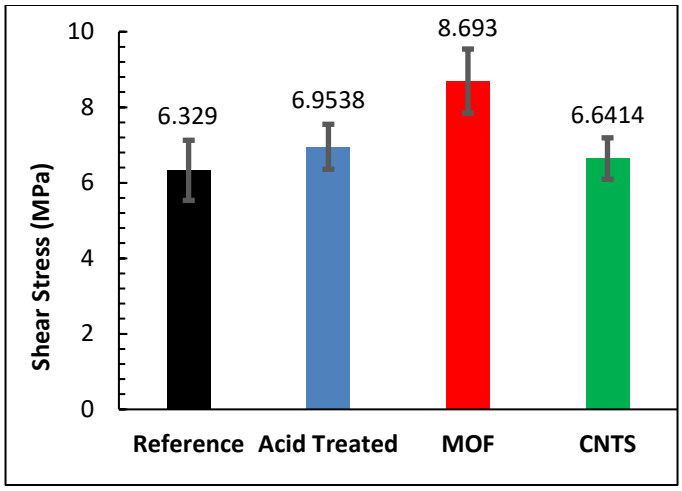

Figure 8.15 The effect of surface treatment method on bond adhesive shear strength.

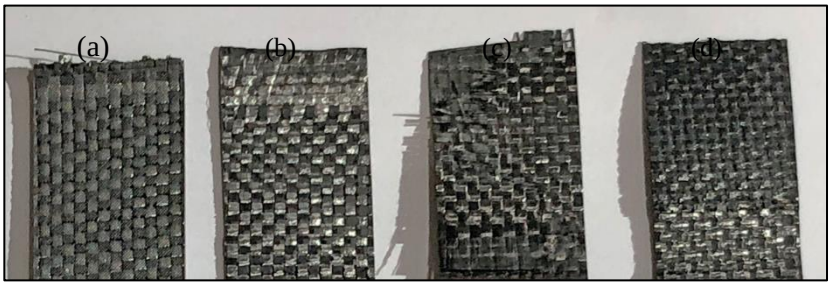

Figure 8.16 Representative images of the different joint failure modes observed for composites based on (a) reference fibers and fibers, (b) acid treated fibers, (c) fibers with MOF, and (d) fibers with surface grown CNTs.

8.3.5. Fracture Analysis

To explore the effects of the different surface treatments on the fiber's/matrix interactions, the micrographs of fractured surfaces of the different tensile samples were examined. Figure 8.17.a) clearly show that the fracture of the composite based on the reference untreated fibers was dominated by fiber breakage, the lack of strong interface between the fiber and matrix; evident by the clean fiber surface in Figure 8.17.a), which lead to unstoppable crack propagation across the fiber. Activating the fibers via acid treatment did not change the pattern of fiber failure but Figure 8.17.b) suggest there was better

adhesion evident by the residue of the epoxy on the fiber's surface.

Upon growing MOFs, they act as crack hindrances, as shown in Figure 8.17.c). While the cracks initiated in matrix zone, upon further loading get deflected along the axis of the fibers on a wavy trajectory that can be clearly seen in Figure 8.17.c). The MOFs stay intact to the fiber surface manifested by the shiny surface of the fiber; Figure 8.17.c). Figure 8.17.d) suggests that the existence of CNTs at the interface hinders crack propagation along the fiber axis and the matrix in between adjacent fibers did not undergo longitudinal crack propagation as well. Very rough fracture surfaces were observed in Figure 8.17.d), indicating good adhesion between the fibers and the matrix.

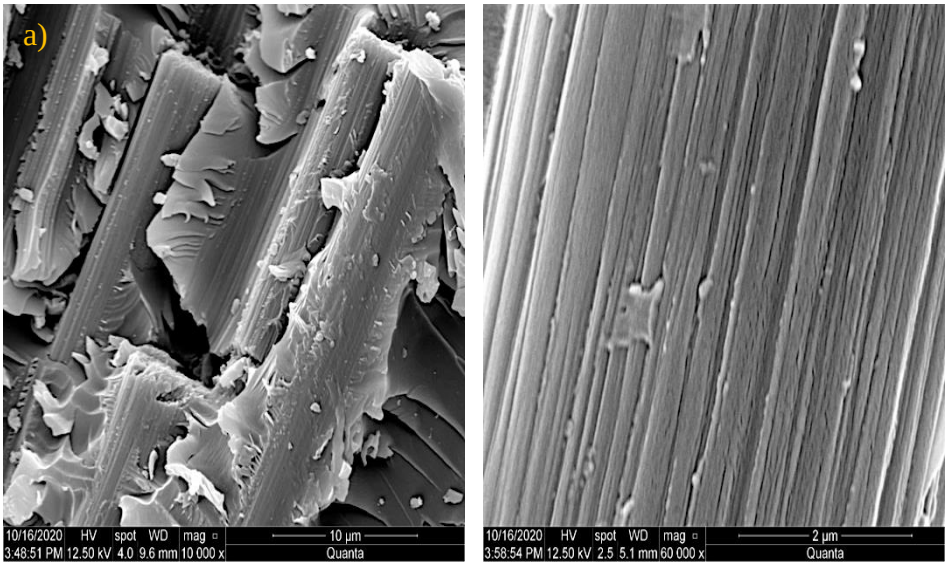

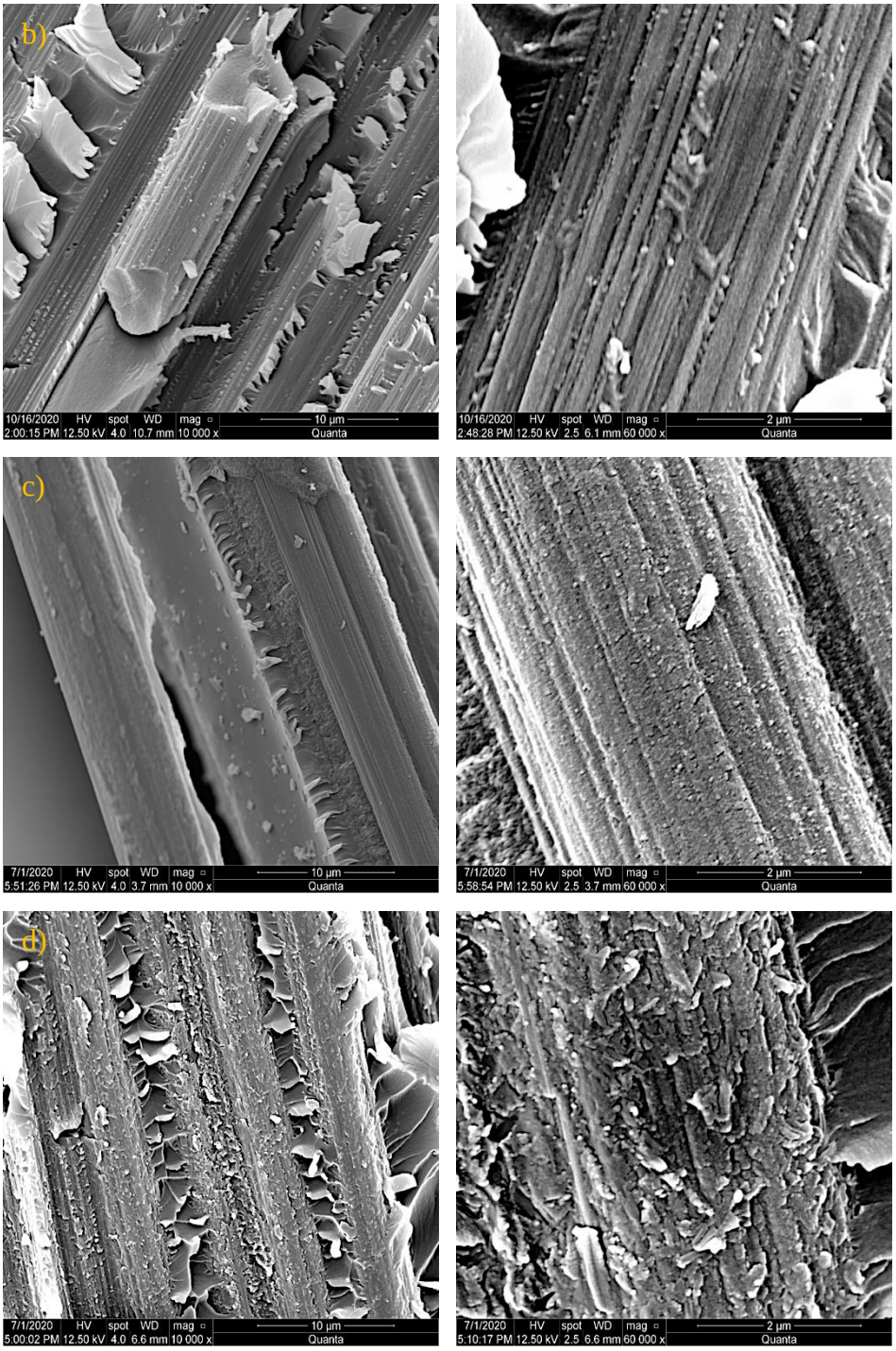

Figure 8.17 SEM micrographs of the fracture surfaces for composite based on: a) the reference untreated fibers; b) the acid treated fibers; c) the fibers with MOFs; d) the fibers with surface grown CNTs at two different magnifications.

9. Conclusions and Recommendations

A thorough investigation to understand the behavior of hybrid CFRP composites was documented in this dissertation. Numerous configurations of hybrid composites were fabricated by employing nanofillers like ZnO nanorods, CNTs, and MOFs as interface layers between fiber and the polymer matrix. This interface was created by tailoring the carbon fiber surface to adhere to various nanofillers or MOFs using different growth procedures like graphitic structures by design (GSD) method or hydrothermal methods.

Several experimental and modeling techniques were utilized to probe the effects of these carbon fiber surface modifications on various mechanical properties. Different experimental procedures performed for each nanofiller configuration, and the summary of their results are presented in this chapter.

9.1. Conclusions

To study the effect of topology of ZnO nanorods and the efficacy of functionalizing carbon fiber using dopamine, eight different configurations of three-plies composites were fabricated. Strength, stiffness, and damping properties of each configuration were compared against each other. Among the three different topologies, the 53 μm mesh-based samples attained a 14 % and 13.3 % increase in strength and stiffness respectively. Among the polydopamine functionalized samples, a 30 % and 7 % improvement in strength and stiffness respectively was recorded for the PDA_A sample. These results are in comparison with the CFRP composite configuration with fully grown ZnO nanorods. The glass transition temperature calculations from DMA analysis

showed the efficiency of dopamine in enhancing the interfacial adhesion between fiber and the matrix. This was evident by the 6 % and 5 % increase in T_g, for the PDA_B and PDA_BA samples respectively, when compared to the As Is sample with no nanorods.

A molecular dynamics study was performed to probe the effects of ZnO nanorods on the carbon fiber/epoxy interface at a molecular scale. Two models were built in Materials Studio software (Biovia-Dassault Systems): Fiber/Epoxy model; Fiber/Epoxy/ZnO hybrid model. After the canonical assemblies were optimized and equilibrated to 298 K, mechanical properties were calculated. Significant improvements were observed in the elastic stiffness constants during the presence of ZnO nanorods, the highest being 35 % for C_{xx}, the axial modulus. Also, 25 % and 23 % increase in bulk modulus and shear modulus affirmed the advantages of ZnO nanorods at the fiber/matrix interface.

In a different investigation, CNTs were grown on the surface of plain-oven carbon fibers fabrics. The growth was tailored into uniform, fine, and coarse patterned topologies. Composites were fabricated utilizing these different topologies and were tested using tensile, DMA and flexure stress relaxation experiments to reveal the effect of the CNTs topologies on the different static and dynamic properties of the composites. Improvement in strength by 19 % for the fine, by 6 % for the coarse patterns, and 3 % for the uniform patterns was recorded, respectively. These improvements achieved by the patterned growth were also accompanied by enhancement on the modulus; roughly by 18.7 % for both patterned growths. A similar trend was noticed for the fine patterned

composite during T_g comparison and stress relaxation tests. Its change in T_g was as high as 13.15 % compared to the reference composite at 10 Hz. Also, at the most severe case of 60 MPa and 75 °C, fine patterned sample exhibited a 5 MPa relaxation in stress compared to 11 MPa for the reference composite. These improvements stem from the enhanced interface stiffness, strength and the induced interlocking mechanism facilitated by the patterned growth of the CNTs.

To probe deeper into the significance of CNTs topology on the carbon fiber/epoxy interface, viscoplasticity in these hybrid composites was studied through stress relaxation and creep tests. These experimental results were used to build an analytical creep model. This model offers an undeniable advantage in predicting long term creep behavior using relatively short-term load relaxation tests. However, this model assumes a uniform material behavior at all temperature and stress levels. This results in discrepancies at higher loads and temperatures nearing T_g. The experimental results showed a significant resistance by the patterned samples to both stress relaxation and creep, when compared to the reference sample. The analytical creep model results showed a better behavior of all the CNTs based configuration, when compared to the reference sample. However, the values for the strain predicted by these models are much higher than the experimental results.

An undesired consequence of employing nanofillers at the carbon fiber/ polymer matrix interface is delamination. Due to the introduction of this third interface, insufficient seepage of epoxy into the fibers, resulting in increased possibilities of delamination in hybrid CFRPs. To mitigate this, different

topologies of CNTs at the fiber/matrix interface were grown and tested for crack propagation. Experimental and modeling techniques were utilized to study fracture in hybrid composites. The experimental results concluded that 105 μm patterned CNTs aided in delayed crack initiation, and propagation. The ANSYS simulation results using both CZM and VCCT methods agreed with this conclusion. These results show that coarser patterns of CNTs perform better in offering resistance during crack propagation in hybrid composites.

The results of these studies emphasize that the mere growth of CNTs/ZnO nanorods on carbon fibers fabric prior to composite fabrication might not yield the best performance possible. Rather, to realize the full benefits of hybrid composites based on multiscale reinforcements, such as CNTs, ZnO nanorods and carbon fibers, the growth of nano fillers should be planned into an optimal topology that enhances the required FRPs properties.

The synthesis of CNTs/ZnO nanorods discussed in the prior experiments limit the size of the carbon fabric utilized later to make a composite. This is because of the size limitations of the enclosed vacuum chamber in magnetron sputtering machine, required for PVD. Hence, another investigation which provides a practical route for enhancing the interfacial, mechanical, and dynamic properties of FRPs by utilizing scalable, yet tailorable synthesis of MOFs on carbon fiber, as reinforcements prior to composite fabrications was performed. The MOFs furnish the fibers with significant increase in the interfacial area to ensure better adhesion to the epoxy matrix. The synthesis technique yields crystalline Ni based MOFs that are also fitting as catalysts for growing CNTs to

add more functionalities to the composite. The growth can be tailored to control both the amount and the porosity of the MOFs; significant MOF growth leads to dense CNTs growth as it substantiates a continuous source of Ni catalyst needed for the CNTs growth.

Tensile testing suggested that the MOFs outperform other surface treatments such as acid functionalizing of the carbon fibers in improving the strength by furnishing new surface area and by acting as mechanical anchors in the epoxy matrix. Adding this metallic phase also assisted in a significant shift of the T_g of the composite by 20 °C compared to composites based on the pristine fibers. The damping performance of the fiber/MOFs hybrid composite outperformed all other configurations, including those incorporating CNTs, yielding a damping parameter improvement of 500%.

The crucial improvement induced by the MOFs is that for the shear lap joint strength, as the MOFs based hybrid composite yielded 40% improvements in the shear strength of the joint. These preliminary results lay the foundation for next generation of hybrid composites that can contribute to several functionalities in FRPs while offering remedies to the root cause of failure in composites; poor interfacial adhesion between the fibers and the matrix.

9.2. Recommendations

The role of moisture on the carbon fiber strength degradation during hydrothermal growth procedures is significant. This is evident by the lower strength and stiffness values of CFRP composites after the growth of ZnO nanorods, when compared to CFRP composites with no nanorods. An

investigation aiming to document effective moisture removal techniques in a carbon fiber surface could help resolve this issue.

A study of ZnO nanorods size vs. strength of CFRPs could help in establishing the nominal size of ZnO nanorods required to be grown on the carbon fiber/matrix interface. This allows for better polymer matrix flow into the fiber strands, without ZnO nanorods acting as a hindrance.

Higher computational resources could assist in building a more comprehensive molecular dynamics model. Effects of temperature in changing the density and mechanical properties of the assembly can be studied. Also, dynamic methods to calculate mechanical properties, taking into effect the influence of entropy, could result in more accurate data.

Due to the large number of configurations in this work, and limited amount of time, the accumulation of experimental data for the viscoplastic properties was not optimal. Larger times and more samples in stress relaxation tests could result in more accurate analytical creep model.

The creep model used in this dissertation does not take the effects of temperature and initial stresses into consideration. This results in significant deviations from experimental data at higher loads and temperatures. Hence, other creep models using neural networks could yield better predictions.

Higher computational resources could accommodate lower mesh sizes in ANSYS software. This could facilitate the capture of intricate details at crack tips during crack propagation.

Investigations involving MOFs in structural applications is very limited in

literature. To develop and utilize these surface modifications in CFRPs efficiently, extensive experimental testing and analysis is required.

REFERENCES

Abdelal, N. R., Al-Saleh, M. H., & Irshidat, M. R. (2018). Utilizing Vacuum Bagging Process to Prepare Carbon Fiber/CNT-Modified-epoxy Composites with Improved Mechanical Properties. *Polymer-Plastics Technology and Engineering*, *57*(3), (pp.175–184). doi:10.1080/03602559.2017.1315644

Akgun, M. C., Kalay, Y. E., & Unalan, H. E. (2012). Hydrothermal zinc oxide nanowire growth using zinc acetate dihydrate salt. *Journal of Materials Research*, *27*(11), (pp.1445–1451). doi:10.1557/jmr.2012.92

Al-Haik, M. (2014). Molecular dynamics simulations of thermally induced damage on asphaltene and resins aggregates. *Journal of Computational and Theoretical Nanoscience*, *11*(3),(pp. 685–692). doi:10.1166/jctn.2014.3412

Al-Haik, M. S. (2002). Durability of a polymer matrix composite: Neural networks approach. In *Ph.D. Thesis*. Retrieved from https://ui.adsabs.harvard.edu/abs/2002PhDT.....24A

Alfieri, M. L., Panzella, L., Oscurato, S. L., Salvatore, M., Avolio, R., Errico, M. E., Maddalena, P., Napolitano, A., & d'Ischia, M. (2018). The chemistry of polydopamine film formation: The amine-quinone interplay. *Biomimetics*, *3*(3). doi:10.3390/biomimetics3030026

An, F., Lu, C., Li, Y., Guo, J., Lu, X., Lu, H., He, S., & Yang, Y. (2012). Preparation and characterization of carbon nanotube-hybridized carbon fiber to reinforce epoxy composite. *Materials & Design*, *33*, (pp.197–202). doi:10.1016/J.MATDES.2011.07.027

Anon. (1989). Thin film deposition. *Ericsson Review (English Edition)*, *66*(3), (pp. 90–99). doi:10.1017/cbo9780511777691.003

Arab, B., Shokuhfar, A., & Ebrahimi-Nejad, S. (2012). *Glass Transition Temperature of Cross-Linked Epoxy Polymers: a Molecular Dynamics Study* (Vol. 1, Issue 1).

Aslam, S., Subhan, F., Yan, Z., Etim, U. J., & Zeng, J. (2017). Dispersion of nickel nanoparticles in the cages of metal-organic framework: An efficient sorbent for adsorptive removal of thiophene. *Chemical Engineering Journal*, *315*, (pp. 469–480).

ASTM, D3039. (1995). Standard Test Method for Tensile Properties of Polymer Matrix Composite Materials. *ASTM Standard*.

ASTM, D4065. (2011). Standard Practice for Plastics : Dynamic Mechanical Properties : Determination and Report of Procedures. *Annual Book of ASTM Standards*, *i*, (pp. 1–7). doi:10.1520/D4065-12.1.8

ASTM, D5023. (2015). Standard Test Method for Plastics: Dynamic Mechanical Properties: In Flexure (Three-Point Bending). *ASTM Standard*.

ASTM, D5528. (2013). Standard Test Method for Mode I Interlaminar Fracture Toughness of Unidirectional Fiber-Reinforced Polymer Matrix Composites 1. *ASTM Standard*. doi:10.1520/D5528-13

ASTM, D5573. (2019). Standard Practice for Classifying Failure Modes in Fiber-Reinforced-Plastic (FRP)Joints. *ASTM Standard*.

ASTM, D5687. (2007). Standard guide for preparation of flat composite panals with processing guidelines for specimen preparation[1]. *ASTM Standard*.

ASTM, D5868. (2014). Standard Test Method for Lap Shear Adhesion for Fiber Reinforced Plastic (FRP) Bonding. In *ASTM Standard*.

ASTM, D7028. (2015). Standard Test Method for Glass Transition Temperature (DMA Tg) of Polymer Matrix Composites by Dynamic Mechanical Analysis (DMA). In *ASTM Standard* (Vol. 388, pp. 539–547).

Ayyagari, S., & Al-Haik, M. (2019). Enhancing the viscoelastic performance of carbon fiber composites by incorporating CNTs and ZnO nanofillers. *Applied Sciences (Switzerland)*, *9*(11). doi:10.3390/app9112281

Ayyagari, S., Al-Haik, M., Ren, Y., & Nepal, D. (2020). Effect of Nano-Reinforcement Topologies on the Viscoelastic Performance of Carbon Nanotube/Carbon Fiber Hybrid Composites. *Nanomaterials*, *10*(6), 1213. doi:10.3390/nano10061213

Ayyagari, S., Al-Haik, M., & Rollin, V. (2018). Mechanical and Electrical Characterization of Carbon Fiber/Bucky Paper/Zinc Oxide Hybrid Composites. *C*. doi:10.3390/c4010006

Bahei-El-din, Y. A. (1996). Finite element analysis of viscoplastic composite materials and structures. In *Mechanics of Composite Materials and Structures* (Vol. 3, Issue 1). doi:10.1080/10759419608945852

Bao, C., Niu, Q., Chen, Z.-A., Cao, X., Wang, H., & Lu, W. (2019). Ultrathin nickel-metal–organic framework nanobelt based electrochemical sensor for the determination of urea in human body fluids. *RSC Advances*, *9*(50), (pp. 29474–29481). doi:10.1039/C9RA05716A

Boroujeni, A. Y., & Al-Haik, M. S. (2019). Interlaminar fracture toughness of hybrid carbon fiber-carbon nanotubes-reinforced polymer composites. *Polymer Composites*, *40*(S2), (pp. E1470–E1478). doi:10.1002/pc.25054

Borowski, E., Soliman, E., Kandil, U. F., & Taha, M. R. (2015). Interlaminar fracture toughness of CFRP laminates incorporating multi-walled carbon nanotubes. *Polymers*, *7*(6), (pp. 1020–1045). doi:10.3390/polym7061020

Brooks, C. S., Golden, G. S., & Scola, D. A. (1974). Characterization of surface reactivity of graphite fiber by solute adsorption. *Carbon*, *12*(6), (pp. 609–617). doi:10.1016/0008-6223(74)90085-2

Bussu, G., & Lazzeri, A. (2006). On the use of dynamic mechanical thermal analysis (DMTA) for measuring glass transition temperature of polymer matrix fibre reinforced composites. *Journal of Materials Science*, *41*(18), (pp. 6072–6076). doi:10.1007/s10853-006-0694-3

Byrne, D., McGlynn, E., Cullen, J., & Henry, M. O. (2011). A catalyst-free and facile route to periodically ordered and c-axis aligned ZnO nanorod arrays on diverse substrates. *Nanoscale*, *3*(4), (pp. 1675–1682). doi:10.1039/c0nr00919a

Case, F. (2011). Nanotechnology and molecular simulation. *Molecular Simulation*, *37*(8), 647. doi:10.1080/08927022.2011.593318

Chalykh, A. E., Petrova, T. F., Antipov, Y. V., Aliev, A. D., Matveev, V. V., & Telitsyna, M. Y. (2020). Water Sorption by Carbon Fibers. *Protection of Metals and Physical Chemistry of Surfaces*, *56*(1), (pp. 20–29). doi:10.1134/S2070205120010049

Chartoff, R. P., Menczel, J. D., & Dillman, S. H. (2009). Dynamic Mechanical Analysis (DMA). In *Thermal Analysis of Polymers* (pp. 387–495). doi:10.1002/9780470423837.ch5

De Cicco, D., Asaee, Z., & Taheri, F. (2017). Use of nanoparticles for enhancing the interlaminar properties of fiber-reinforced composites and adhesively bonded joints—a review. In *Nanomaterials* (Vol. 7, Issue 11). MDPI AG. doi:10.3390/nano7110360

Deriabina, O., Lebovka, N., Bulavin, L., & Goncharuk, A. (2013). Regulation of dispersion of carbon nanotubes in a mixture of good and bad solvents. *ArXiv*. Retrieved from https://arxiv.org/ftp/arxiv/papers/1304/1304.5679.pdf

Dong, S., & Gauvin, R. (1993). Application of dynamic mechanical analysis for the study of the interfacial region in carbon fiber/epoxy composite materials. *Polymer Composites*, *14*(5), (pp. 414–420). doi:10.1002/pc.750140508

Du, L., Xing, L., Zhang, G., & Sun, S. (2020). Metal-organic framework derived carbon materials for electrocatalytic oxygen reactions: Recent progress and future perspectives. In *Carbon* (Vol. 156, pp. 77–92). Elsevier Ltd. doi:10.1016/j.carbon.2019.09.029

Ehlert, G. J., & Sodano, H. A. (2009). Zinc oxide nanowire interphase for enhanced interfacial strength in lightweight polymer fiber composites. *ACS Applied Materials and Interfaces*, *1*(8), (pp. 1827–1833). doi:10.1021/am900376t

Fan, H. B., & Yuen, M. M. F. (2007). Material properties of the cross-linked epoxy resin compound predicted by molecular dynamics simulation. *Polymer*, *48*(7), (pp. 2174–2178). doi:10.1016/j.polymer.2007.02.007

Fitzer, E. (1989). Pan-based carbon fibers—present state and trend of the technology from the viewpoint of possibilities and limits to influence and to control the fiber properties by the process parameters. *Carbon*, *27*(5), (pp. 621–645). doi:10.1016/0008-6223(89)90197-8

Fleker, O., Borenstein, A., Lavi, R., Benisvy, L., Ruthstein, S., & Aurbach, D. (2016). Preparation and Properties of Metal Organic Framework/Activated Carbon Composite Materials. *Langmuir*, *32*(19), (pp. 4935–4944). doi:10.1021/acs.langmuir.6b00528

Furukawa, H., Cordova, K. E., O'Keeffe, M., & Yaghi, O. M. (2013). The Chemistry and Applications of Metal-Organic Frameworks. *Science*, *341*(6149). doi:10.1126/SCIENCE.1230444

Galan, U., Lin, Y., Ehlert, G. J., & Sodano, H. A. (2011). Effect of ZnO nanowire morphology on the interfacial strength of nanowire coated carbon fibers. *Composites Science and Technology*, *71*(7), (pp. 946–954). doi:10.1016/j.compscitech.2011.02.010

Gan, Y. X., Jayatissa, A. H., Yu, Z., Chen, X., & Li, M. (2020). Hydrothermal Synthesis of Nanomaterials. *Hindawi Journal of Nanomaterials*, *2020*. doi:10.1155/2020/8917013

Gates, T. S., Chen, J. L., & Sun, C. T. (1994). Micromechanical Characterization of Nonlinear Behavior of Advanced Polymer Matrix Composites. *NASA Technical Memorandum 1*. Retrieved from https://ntrs.nasa.gov/search.jsp?R=19940029891

Gates, T. S., & Sun|, C. T. (1990). *Elastic/Viscoplastic Constitutive Model for Fiber Reinforced Thermoplastic Composites*. doi:10.2514/3.59922

Giurgiutiu, V. (2016). Structural Health Monitoring of Aerospace Composites. In V. B. T.-S. H. M. of A. C. Giurgiutiu (Ed.), *Academic Press* (pp. 1–23). Academic Press. doi:10.1016/B978-0-12-409605-9.00001-5

Gliszczynski, A., Samborski, S., Wiacek, N., & Rzeczkowski, J. (2019). Mode I interlaminar fracture of glass/epoxy unidirectional laminates. Part II: Numerical analysis. *Materials*, *12*(10), (pp. 1–18). doi:10.3390/ma12101604

Godara, A., Mezzo, L., Luizi, F., Warrier, A., Lomov, S. V., van Vuure, A. W., Gorbatikh, L., Moldenaers, P., & Verpoest, I. (2009). Influence of carbon nanotube reinforcement on the processing and the mechanical behaviour of carbon fiber/epoxy composites. *Carbon*, *47*(12), (pp. 2914–2923). doi:10.1016/j.carbon.2009.06.039

Goertzen, W. K., & Kessler, M. R. (2006). Creep behavior of carbon fiber/epoxy matrix composites. *Materials Science and Engineering: A*, *421*(1–2), (pp. 217–225). doi:10.1016/J.MSEA.2006.01.063

Goertzen, W. K., & Kessler, M. R. (2007). Dynamic mechanical analysis of carbon/epoxy composites for structural pipeline repair. *Composites Part B: Engineering*. doi:10.1016/j.compositesb.2006.06.002

H S, M. W., & N, K. K. (2014). Finite Element Modeling for Delamination Analysis of Double Cantilever Beam Specimen. *International Journal of Mechanical Engineering*, *1*(5), (pp. 6–11). doi:10.14445/23488360/ijme-v1i5p105

Hadden, C. M., Jensen, B. D., Bandyopadhyay, A., Odegard, G. M., Koo, A., & Liang, R. (2013). Molecular modeling of EPON-862/graphite composites: Interfacial characteristics for multiple crosslink densities. *Composites Science and Technology*, *76*, (pp. 92–99). doi:10.1016/j.compscitech.2013.01.002

Hart, E. W., & Solomon, H. D. (1973). Load relaxation studies of polycrystalline high purity aluminium. *Acta Metallurgica*, *21*(3), (pp. 295–307). doi:10.1016/0001-6160(73)90017-5

Hsiao, K. T., Alms, J., & Advani, S. G. (2003). Use of epoxy/multiwalled carbon nanotubes as adhesives to join graphite fibre reinforced polymer composites. *Nanotechnology*, *14*(7), (pp. 791–793). doi:10.1088/0957-4484/14/7/316

Hu, J., Wang, H., Gao, Q., & Guo, H. (2010). Porous carbons prepared by using metal-organic framework as the precursor for supercapacitors. *Carbon*, *48*(12), (pp. 3599–3606). doi:10.1016/j.carbon.2010.06.008

Jiang, J., Xu, C., Su, Y., Guo, Q., Liu, F., Deng, C., Yao, X., & Zhou, L. (2016). *Influence of Carbon Nanotube Coatings on Carbon Fiber by Ultrasonically Assisted Electrophoretic Deposition on Its Composite Interfacial Property*. doi:10.3390/polym8080302

Khan, M. F., Ansari, A. H., Hameedullah, M., Ahmad, E., Husain, F. M., Zia, Q., Baig, U., Zaheer, M. R., Alam, M. M., Khan, A. M., AlOthman, Z. A., Ahmad, I., Ashraf, G. M., & Aliev, G. (2016). Sol-gel synthesis of thorn-like ZnO nanoparticles endorsing mechanical stirring effect and their antimicrobial activities: Potential role as nano-antibiotics. *Scientific Reports*, *6*(1), 27689. doi:10.1038/srep27689

Koratkar, N. A., Suhr, J., Joshi, A., Kane, R. S., Schadler, L. S., Ajayan, P. M., & Bartolucci, S. (2005). Characterizing energy dissipation in single-walled carbon nanotube polycarbonate composites. *Applied Physics Letters*, *87*(6), 063102. doi:10.1063/1.2007867

Krylov, A., Vtyurin, A., Petkov, P., Senkovska, I., Maliuta, M., Bon, V., Heine, T., Kaskel, S., & Slyusareva, E. (2017). Raman spectroscopy studies of the terahertz vibrational modes of a DUT-8 (Ni) metal–organic framework. *Physical Chemistry Chemical Physics*, *19*(47), (pp. 32099–32104). doi:10.1039/C7CP06225G

Li, C., & Strachan, A. (2015). Molecular scale simulations on thermoset polymers: A review. In *Journal of Polymer Science, Part B: Polymer Physics* (Vol. 53, Issue 2, pp. 103–122). John Wiley and Sons Inc. doi:10.1002/polb.23489

Li, M., Zhou, H., Zhang, Y., Liao, Y., & Zhou, H. (2017). The effect of defects on the interfacial mechanical properties of graphene/epoxy composites. *RSC Advances*, *7*(73), (pp. 46101–46108). doi:10.1039/c7ra08243f

Li, X. (2011). Applications of Molecular Dynamics in Atmospheric and Solution Chemistry. In *Thesis*. Retrieved from http://www.diva-portal.org/smash/record.jsf?pid=diva2:414439

Li, Y., Jiang, B., & Huang, Y. (2020). Constructing nanosheet-like MOF on the carbon fiber surfaces for improving the interfacial properties of carbo fiber /epoxy composites. *Applied Surface Science*, *514*, 145870. doi:10.1016/j.apsusc.2020.145870

Lin, Y., Ehlert, G., & Sodano, H. A. (2009). Increased Interface Strength in Carbon Fiber Composites through a ZnO Nanowire Interphase. *Advanced Functional Materials*, *19*(16), (pp. 2654–2660). doi:10.1002/adfm.200900011

Liu, J., Chang, M.-J., & Du, H.-L. (2016). Controllable growth of highly organized ZnO nanowires using templates of electrospun nanofibers. *Journal of Materials Science: Materials in Electronics*, *27*(7), (pp. 7124–7131). doi:10.1007/s10854-016-4675-2

Liu, X. W., Sun, T. J., Hu, J. L., & Wang, S. D. (2016). Composites of metal-organic frameworks and carbon-based materials: Preparations, functionalities and applications. In *Journal of Materials Chemistry A* (Vol. 4, Issue 10, pp. 3584–3616). Royal Society of Chemistry. doi:10.1039/c5ta09924b

Lyu, S. C., Zhang, Y., Ruh, H., Lee, H.-J., Shim, H.-W., Suh, E.-K., & Lee, C. J. (2002). Low temperature growth and photoluminescence of well-aligned zinc oxide nanowires. *Chemical Physics Letters*, *363*(1–2), (pp. 134–138). doi:10.1016/S0009-2614(02)01145-4

Malvern, L. E. (1949). *The Propagation of Longitudinal Waves of Plastic Deformation in a Bar of Material Exhibiting a Strain-rate Effect*. Division of Applied Mathematics, Brown. Retrieved from https://books.google.com/books?id=wP1KtwAACAAJ

Mattox, D. M. (2002). Physical vapor deposition (PVD) processes. *Metal Finishing*, *100*, (pp. 394–408). doi:10.1016/S0026-0576(02)82043-8

May, M. (2016). Measuring the rate-dependent mode I fracture toughness of composites - A review. In *Composites Part A: Applied Science and Manufacturing* (Vol. 81, pp. 1–12). Elsevier Ltd. doi:10.1016/j.compositesa.2015.10.033

Melo, J. D. D., & Radford, D. W. (2005). Time and temperature dependence of the viscoelastic properties of CFRP by dynamic mechanical analysis. *Composite Structures*, *70*(2), (pp. 240–253). doi:10.1016/J.COMPSTRUCT.2004.08.025

Menard, K. (2008). *Dynamic Mechanical Analysis: A Practical Introduction, Second Edition*. CRC Press.

Morkoç, H., & Özgür, U. (2009). *Zinc oxide : fundamentals, materials and device technology / Hadis Morkoç and Ümit Özgür*. Wiley-VCH.

Murray, B. R., Fonteyn, S., Carrella-Payan, D., Kalteremidou, K.-A., Cernescu, A., Van Hemelrijck, D., & Pyl, L. (2018). *Crack tip monitoring of mode I and mode II delamination in CF/Epoxies under static and dynamic loading conditions using digital image correlation †* 5225. doi:10.3390/icem18-05225

Nasuha, N., Azmi, A. I., & Tan, C. L. (2017). A review on mode-I interlaminar fracture toughness of fibre reinforced composites. *Journal of Physics: Conference Series*, *908*(1). doi:10.1088/1742-6596/908/1/012024

Oterkus, E., Diyaroglu, C., De Meo, D., & Allegri, G. (2016). Fracture modes, damage tolerance and failure mitigation in marine composites. In *Marine Applications of Advanced Fibre-Reinforced Composites* (pp. 79–102). Elsevier Inc. doi:10.1016/B978-1-78242-250-1.00004-1

Pan, J., Li, M., Wang, S., Gu, Y., Li, Q., & Zhang, Z. (2017). Hybrid effect of carbon nanotube film and ultrathin carbon fiber prepreg composites. *Journal of Reinforced Plastics and Composites*, *36*(6), (pp. 452–463). doi:10.1177/0731684416684020

Pawar, V., Kumar, M., Dubey, P., Singh, M. K., Sinha, A., & Singh, P. (2019). Influence of synthesis route on structural, optical, and electrical properties of TiO2. *Applied Physics A*, *125*. doi:10.1007/s00339-019-2948-3

Peng, H., Li, Q., & Chen, T. (2016). Industrial Applications of Carbon Nanotubes. In *Industrial Applications of Carbon Nanotubes*. doi:10.1016/c2015-0-00493-2

Pérez-Pacheco, E., Cauich-Cupul, J. I., Valadez-González, A., & Herrera-Franco, P. J. (2013). Effect of moisture absorption on the mechanical behavior of carbon fiber/epoxy matrix composites. *Journal of Materials Science, 48*(5), (pp. 1873–1882). doi:10.1007/s10853-012-6947-4

Perricone, U., Gulotta, M. R., Lombino, J., Parrino, B., Cascioferro, S., Diana, P., Cirrincione, G., & Padova, A. (2018). An overview of recent molecular dynamics applications as medicinal chemistry tools for the undruggable site challenge. In *MedChemComm* (Vol. 9, Issue 6, pp. 920–936). Royal Society of Chemistry. doi:10.1039/c8md00166a

Perzyna, P. (1966). *Fundamental Problems in Viscoplasticity* (G. G. Chernyi, H. L. Dryden, P. Germain, L. Howarth, W. Olszak, W. Prager, R. F. Probstein, & H. B. T.-A. in A. M. Ziegler (eds.); Vol. 9, pp. 243–377). Elsevier. doi:10.1016/S0065-2156(08)70009-7

Rahmani, H., Ashori, A., & Varnaseri, N. (2016). Surface modification of carbon fiber for improving the interfacial adhesion between carbon fiber and polymer matrix. *Polymers for Advanced Technologies, 27*(6), (pp. 805–811). doi:10.1002/pat.3720

Rahmanian, S., Thean, K. S., Suraya, A. R., Shazed, M. A., Mohd Salleh, M. A., & Yusoff, H. M. (2013). Carbon and glass hierarchical fibers: Influence of carbon nanotubes on tensile, flexural and impact properties of short fiber reinforced composites. *Materials & Design*, *43*, (pp. 10–16). doi:10.1016/J.MATDES.2012.06.025

Rajak, D. K., Pagar, D. D., Menezes, P. L., & Linul, E. (2019). Fiber-reinforced polymer composites: Manufacturing, properties, and applications. *Polymers*, *11*(10). doi:10.3390/polym11101667

Ran, J., He, M., Li, W., Cheng, D., & Wang, X. (2018). Growing ZnO nanoparticles on polydopamine-templated cotton fabrics for durable antimicrobial activity and UV protection. *Polymers*, *10*(5). doi:10.3390/polym10050495

Ribeiro, B., Botelho, E. C., Costa, M. L., & Bandeira, C. F. (2017). Carbon nanotube buckypaper reinforced polymer composites: A review. In *Polimeros* (Vol. 27, Issue 3, pp. 247–255). Associacao Brasileira de Polimeros. doi:10.1590/0104-1428.03916

Roberts, J. C., Powers, J. M., & Craig, R. G. (1978). Fracture toughness and critical strain energy release rate of dental amalgam. *Journal of Materials Science, 13*(5), (pp. 965–971). doi:10.1007/BF00544691

Ryu, J. H., Messersmith, P. B., & Lee, H. (2018). Polydopamine Surface Chemistry: A Decade of Discovery. In *ACS Applied Materials and Interfaces* (Vol. 10, Issue 9, pp. 7523–7540). American Chemical Society. doi:10.1021/acsami.7b19865

Saadati, Y., Chatelain, J.-F., Lebrun, G., Beauchamp, Y., Bocher, P., & Vanderesse, N. (2020). A Study of the Interlaminar Fracture Toughness of Unidirectional Flax/Epoxy Composites. *Journal of Composites Science*, *4*(2), 66. doi:10.3390/jcs4020066

Sadiq, I., & Wang, X. Q. (2012). Estimation Of Interfacial Properties of Various Carbon Fiber Epoxy Composites Using Molecular Modelling And Simulations. *ECCM15 - 15th European Conference on Composite Materials*.

Safavi, M. S., Walsh, F. C., Surmeneva, M. A., Surmenev, R. A., & Khalil-Allafi, J. (2021). Electrodeposited hydroxyapatite-based biocoatings: Recent progress and future challenges. *Coatings*, *11*(1), (pp. 1–62). doi:10.3390/coatings11010110

Samborski, S., Gliszczynski, A., Rzeczkowski, J., & Wiacek, N. (2019). Mode I interlaminar fracture of glass/epoxy unidirectional laminates. Part I: Experimental studies. *Materials*, *12*(10). doi:10.3390/ma12101607

Sanli, A. (2020). Investigation of temperature effect on the electrical properties of MWCNTs/epoxy nanocomposites by electrochemical impedance spectroscopy. *Advanced Composite Materials*, *29*(1), (pp. 31–41). doi:10.1080/09243046.2019.1616409

Sharma, K., & Shukla, M. (2014). Molecular modeling of the mechanical behavior of carbon fiber-amine functionalized multiwall carbon nanotube/epoxy composites. *Xinxing Tan Cailiao/New Carbon Materials*, *29*(2), (pp. 132–142). doi:10.1016/S1872-5805(14)60131-1

Sharma, S., Chandra, R., Kumar, P., & Kumar, N. (2016). Molecular level analysis of carbon nanofiber reinforced polymer composites. *Journal of Composite Materials*, *50*(13), (pp. 1787–1804). doi:10.1177/0021998315596591

Shen, Q., Li, X., Li, R., & Wu, Y. (2020). Application of Metal-Organic Framework Materials and Derived Porous Carbon Materials in Catalytic Hydrogenation. In *ACS Sustainable Chemistry and Engineering* (Vol. 8, Issue 48). American Chemical Society. doi:10.1021/acssuschemeng.0c06849

Shim, J.-W., Park, S.-J., & Ryu, S.-K. (2001). Effect of modification with HNO3 and NaOH on metal adsorption by pitch-based activated carbon fibers. *Carbon*, *39*(11), (pp. 1635–1642). doi:10.1016/S0008-6223(00)00290-6

Singh, C., Mukhopadhyay, S., & Hod, I. (2021). Metal–organic framework derived nanomaterials for electrocatalysis: recent developments for CO2 and N2 reduction. In *Nano Convergence* (Vol. 8, Issue 1, p. 1). Korea Nano Technology Research Society. doi:10.1186/s40580-020-00251-6

Sinnott, S. B., & Andrews, R. (2001). Carbon Nanotubes: Synthesis, Properties, and Applications. *Critical Reviews in Solid State and Materials Sciences*, *26*(3), (pp. 145–249). doi:10.1080/20014091104189

Skandani, A. A., Masghouni, N., Case, S. W., Leo, D. J., & Al-Haik, M. (2012). Enhanced vibration damping of carbon fibers-ZnO nanorods hybrid composites. *Applied Physics Letters*, *101*(7), 73111. doi:10.1063/1.4746398

Sonavane, Y., Paajanen, A., Ketoja, J., Paavilainen, S., & Maloney, T. (2014). *Molecular dynamics simulation of functionalized nanofibrillar cellulose*.

Strano, V., Urso, R. G., Scuderi, M., Iwu, K. O., Simone, F., Ciliberto, E., Spinella, C., & Mirabella, S. (2014). Double Role of HMTA in ZnO Nanorods Grown by Chemical Bath Deposition. *The Journal of Physical Chemistry C*, *118*(48), (pp. 28189–28195). doi:10.1021/jp507496a

Suhr, J., Koratkar, N., Keblinski, P., & Ajayan, P. (2005). Viscoelasticity in carbon nanotube composites. *Nature Materials*, *4*(2), (pp. 134–137). doi:10.1038/nmat1293

Sule, R., & Mishra, A. K. (2020). MOFs-carbon hybrid nanocomposites in environmental protection applications. In *Environmental Science and Pollution Research* (Vol. 27, Issue 14, pp. 16004–16018). Springer. doi:10.1007/s11356-020-08299-x

Sun, L., Yuan, G., Gao, L., Yang, J., Chhowalla, M., Gharahcheshmeh, M. H., Gleason, K. K., Choi, Y. S., Hong, B. H., & Liu, Z. (2021). Chemical vapour deposition. *Nature Reviews Methods Primers*, *1*(1), 5. doi:10.1038/s43586-020-00005-y

Sun, S., Chen, S., Weng, X., Shan, F., & Hu, S. (2019). Effect of carbon nanotube addition on the interfacial adhesion between graphene and epoxy: A molecular dynamics simulation. *Polymers*, *11*(1). doi:10.3390/polym11010121

Systemes, D. (2017). *Materials Studio 2017*.

Taghavi, M., Mattoli, V., Mazzolai, B., Filippeschi, C., & Beccai, L. (2013). Synthesizing tubular and trapezoidal shaped ZnO nanowires by an aqueous solution method. *Nanoscale*, *5*(8), (pp. 3505–3513). doi:10.1039/c3nr34013a

Tak, Y., & Yong, K. J. (2005). Controlled growth of well-aligned ZnO nanorod array using a novel solution method. *Journal of Physical Chemistry B*, *109*(41), (pp. 19263–19269). doi:10.1021/jp0538767

Tang, X., & Yan, X. (2018). A review on the damping properties of fiber reinforced polymer composites. *Journal of Industrial Textiles*, *49*(6), (pp. 693–721). doi:10.1177/1528083718795914

Tehrani, M., Safdari, M., Boroujeni, A. Y., Razavi, Z., Case, S. W., Dahmen, K., Garmestani, H., & Al-Haik, M. S. (2013). Hybrid carbon fiber/carbon nanotube composites for structural damping applications. *Nanotechnology*. doi:10.1088/0957-4484/24/15/155704

Tehrani, Mehran, Boroujeni, A. Y., Hajj, R., & Al-Haik, M. (2013). Mechanical characterization of a hybrid carbon nanotube/ carbon fiber reinforced composite. *ASME International Mechanical Engineering Congress and Exposition, Proceedings (IMECE)*, *9*. doi:10.1115/IMECE2013-62251

Tian, H., Zhang, C., Su, P., Shen, Z., Liu, H., Wang, G., Liu, S., & Liu, J. (2020). Metal-organic-framework-derived formation of Co–N-doped carbon materials for efficient oxygen reduction reaction. *Journal of Energy Chemistry*, *40*, (pp. 137–143). doi:10.1016/j.jechem.2019.03.004

Turon, A., Camanho, P. P., Costa, J., & Renart, J. (2010). Accurate simulation of delamination growth under mixed-mode loading using cohesive elements: Definition of interlaminar strengths and elastic stiffness. *Composite Structures*. doi:10.1016/j.compstruct.2010.01.012

Verma, A., Parashar, A., & Packirisamy, M. (2019). Effect of grain boundaries on the interfacial behaviour of graphene-polyethylene nanocomposite. *Applied Surface Science*, *470*, (pp. 1085–1092). doi:10.1016/j.apsusc.2018.11.218

Wang, G., & Li, X. (2007). Size dependency of the elastic modulus of ZnO nanowires: Surface stress effect. *Applied Physics Letters*, *91*(23). doi:10.1063/1.2821118

Wang, H., Jin, K., Wang, C., Guo, X., Chen, Z., & Tao, J. (2019). Effect of fiber surface functionalization on shear behavior at carbon fiber/epoxy interface through molecular dynamics analysis. *Composites Part A: Applied Science and Manufacturing*, *126*. doi:10.1016/j.compositesa.2019.105611

Wang, J., Wang, Y., Hu, H., Yang, Q., & Cai, J. (2020). From metal-organic frameworks to porous carbon materials: Recent progress and prospects from energy and environmental perspectives. *Nanoscale*, *12*(7), (pp. 4238–4268). doi:10.1039/c9nr09697c

Wang, Z. L. (2004). Nanostructures of Zinc Oxide. *Materials Today: Proceedings*.

Woodhead, A. L., de Souza, M. L., & Church, J. S. (2017). An investigation into the surface heterogeneity of nitric acid oxidized carbon fiber. *Applied Surface Science*, *401*, (pp. 79–88). doi:10.1016/j.apsusc.2016.12.218

Wu, G. M., Hung, C. H., You, J. H., & Liu, S. J. (2004). Surface Modification of Reinforcement Fibers for Composites by Acid Treatments. *Journal of Polymer Research*, *11*(1), (pp. 31–36). doi:10.1023/B:JPOL.0000021734.69852.5b

Xie, D., & Biggers, S. B. (2006). Strain energy release rate calculation for a moving delamination front of arbitrary shape based on the virtual crack closure technique. Part I: Formulation and validation. *Engineering Fracture Mechanics*. doi:10.1016/j.engfracmech.2005.07.013

Xie, F., Hu, W., Ning, D., Zhuo, L., Deng, J., & Lu, Z. (2018). ZnO nanowires decoration on carbon fiber via hydrothermal synthesis for paper-based friction materials with improved friction and wear properties. *Ceramics International*, *44*(4), (pp. 4204–4210). doi:10.1016/j.ceramint.2017.11.224

Yáñez-Sedeño, P., Campuzano, S., & Pingarrón, J. M. (2020). Screen-printed electrodes: Promising paper and wearable transducers for (bio)sensing. In *Biosensors* (Vol. 10, Issue 7, p. 76). MDPI AG. doi:10.3390/BIOS10070076

Yang, G., & Park, S. J. (2019). Conventional and microwave hydrothermal synthesis and application of functional materials: A review. *Materials*, *12*(7). doi:10.3390/ma12071177

Yang, J., Wang, Y., Kong, J., Jia, H., & Wang, Z. (2015). Synthesis of ZnO nanosheets via electrodeposition method and their optical properties, growth mechanism. *Optical Materials*, *46*, (pp. 179–185). doi:10.1016/J.OPTMAT.2015.04.016

Yang, X., Jiang, X., Huang, Y., Guo, Z., & Shao, L. (2017). Building Nanoporous Metal–Organic Frameworks "Armor" on Fibers for High-Performance Composite Materials. *ACS Applied Materials & Interfaces*, *9*(6), (pp. 5590–5599). doi:10.1021/acsami.6b15098

Zakaria, M. R., Md Akil, H., Abdul Kudus, M. H., Ullah, F., Javed, F., & Nosbi, N. (2019). Hybrid carbon fiber-carbon nanotubes reinforced polymer composites: A review. In *Composites Part B: Engineering* (Vol. 176, p. 107313). Elsevier Ltd. doi:10.1016/j.compositesb.2019.107313

Zhang, Q., Liu, J., Sager, R., Dai, L., & Baur, J. (2009). Hierarchical composites of carbon nanotubes on carbon fiber: Influence of growth condition on fiber tensile properties. *Composites Science and Technology*, *69*(5), (pp. 594–601). doi:10.1016/j.compscitech.2008.12.002

Zhao, L., Zhi, J., Zhang, J., Liu, Z., & Hu, N. (2016). XFEM simulation of delamination in composite laminates. *Composites Part A: Applied Science and Manufacturing*, *80*, (pp. 61–71). doi:10.1016/J.COMPOSITESA.2015.10.007

Zhong, Y., Cao, X., Ying, L., Cui, L., Barrow, C., Yang, W., & Liu, J. (2020). Homogeneous nickel metal-organic framework microspheres on reduced graphene oxide as novel electrode material for supercapacitors with outstanding performance.

Journal of Colloid and Interface Science, 561, (pp. 265–274). doi:10.1016/j.jcis.2019.10.023

PUBLICATIONS

Ayyagari, S. and Al-Haik, M., 2019. Enhancing the Viscoelastic Performance of Carbon Fiber Composites by Incorporating CNTs and ZnO Nanofillers. *Applied Sciences*, 9(11), p.2281. doi:10.3390/app9112281

Ayyagari, S., Al-Haik, M., Ren, Y., & Nepal, D. (2020). Effect of Nano-Reinforcement Topologies on the Viscoelastic Performance of Carbon Nanotube/Carbon Fiber Hybrid Composites. *Nanomaterials*, 10(6), 1213. doi:10.3390/nano10061213

Ayyagari, S., Al-Haik, M. and Rollin, V., 2018. Mechanical and Electrical Characterization of Carbon Fiber/Bucky Paper/Zinc Oxide Hybrid Composites. *C,* 4(1), p.6. doi:10.3390/c4010006

B. Dikici, S. Motagi, P. Kantamani, S. Ayyagari, G. Villarroel, M. Al-Haik. Processing of Agricultural Biomass for Producing Reinforced Polymer Composites. *Proceedings of ASME Power Conference and Nuclear Forum* July 14-18, 2019, Salt Lake City, UT, USA.

B. Dikici, S. Motagi, P. Kantamani, S. Ayyagari, M. Al-Haik. Thermal Conductivity Study of Biomass Reinforced Polymer Composites. *Proceedings of SHTC Summer Heat Transfer Conference*, July 12-15, 2020, Rosen Shingle Creek, Orlando, FL, USA.

M. Al-Haik, Y. Ren, S . Ayyagari, A. Abbot, J. Baur, D. Nepal. Enhanced Carbon Fibers Interfaces for Additive Manufacturing of Epoxy based Composites. *MRS Spring and Fall Meeting*, November 28-December 4, 2020, Boston MA.

M. Al-Haik, S. Ayyagari, Ren and D. Nepal. Effect of the Interface Topology on the Mechanical Performance of Hybrid Carbon Fiber Carbon Nanotubes Composite. *MRS Spring and Fall Meeting*, November 28-December 4, 2020, Boston MA.

Seifans, A. M., Ayyagari, S., & Al-Haik, M. (2021). Elastic/viscoplastic characterization of additively manufactured composite based on continuous carbon fibers. *Aerospace Science and Technology,* 111, 106562. doi:10.1016/j.ast.2021.106562.

S. Ayyagari, M. Al-Haik. Damping Characterization of Hierarchical Composites. IMECE2018-89641.*ASME 2018 International Mechanical Engineering Congress and Exposition (IMECE),* November 9-15, 2018, Pittsburgh, PA, USA.

APPENDIX A – LOGARITHMIC CURVES FOR OVERSTRESS CALCULATIONS

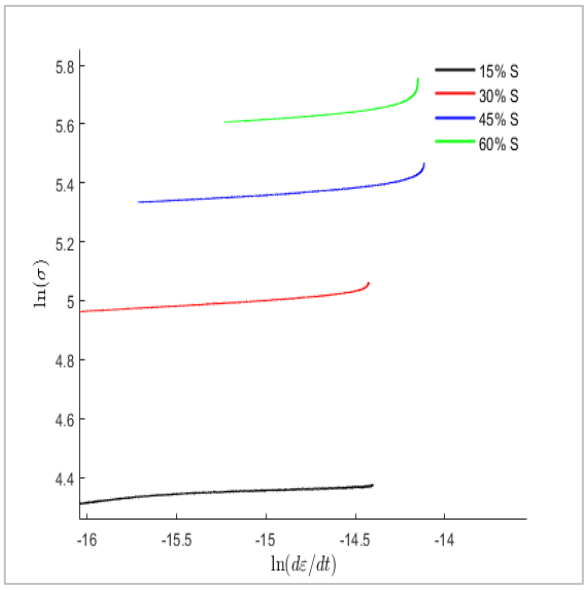

Figure 0.1 Logarithmic plot of the stress and strain rate under T=25 °C for desized composite configuration. The initial stresses were taken as 15-60 % of the ultimate tensile strength at T=25 °C for the desized composite configuration.

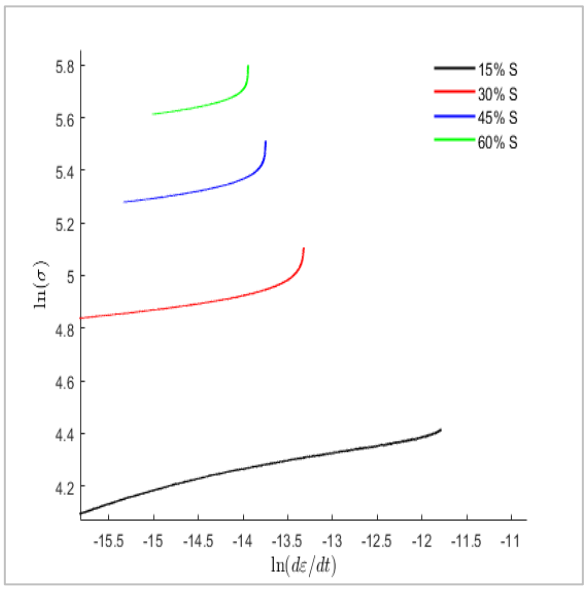

Figure 0.2 Logarithmic plot of the stress and strain rate under T=45 °C for desized composite configuration. The initial stresses were taken as 15-60 % of the ultimate tensile strength at T=45 °C for the desized composite configuration.

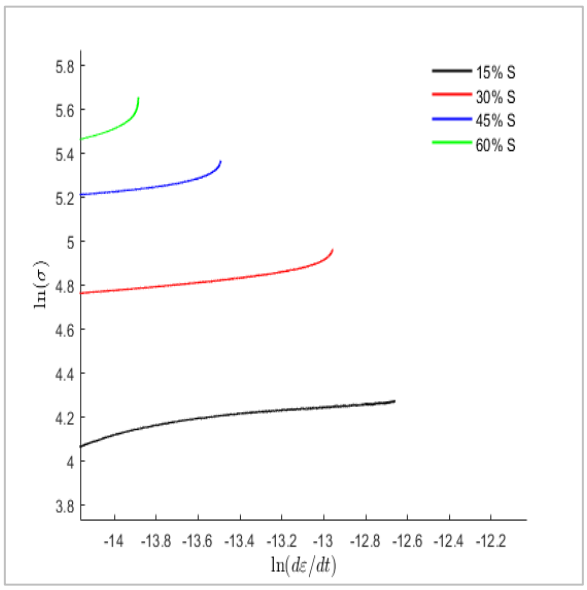

Figure 0.3 Logarithmic plot of the stress and strain rate under T=55 °C for desized composite configuration. The initial stresses were taken as 15-60 % of the ultimate tensile strength at T=55 °C for the desized composite configuration.

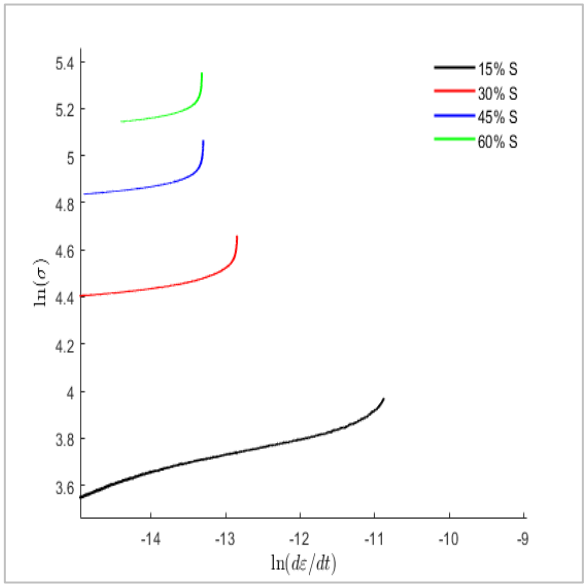

Figure 0.4 Logarithmic plot of the stress and strain rate under T=75 °C for desized composite configuration. The initial stresses were taken as 15-60 % of the ultimate tensile strength at T=75 °C for the desized composite configuration.

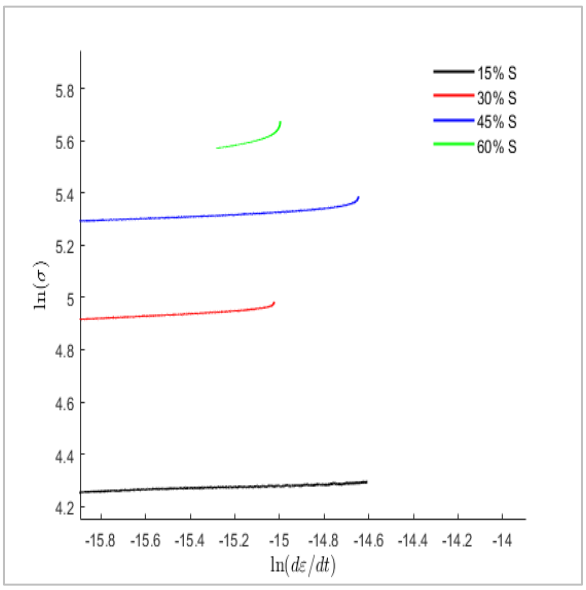

Figure 0.5 Logarithmic plot of the stress and strain rate under T=25 °C for Full Growth composite configuration. The initial stresses were taken as 15-60 % of the ultimate tensile strength at T=25 °C for the Full Growth composite configuration.

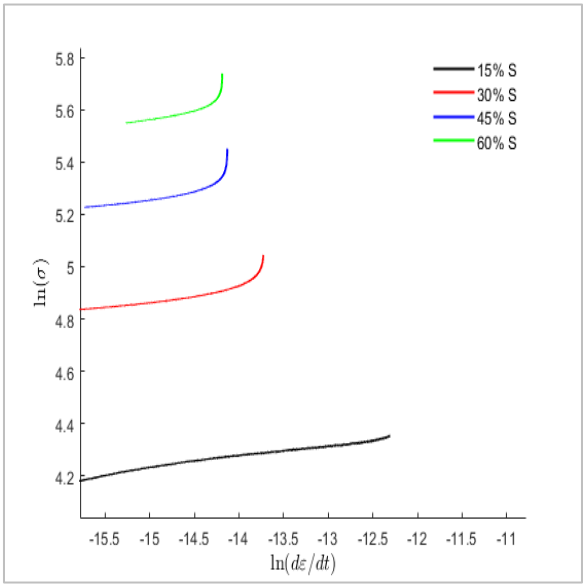

Figure 0.6 Logarithmic plot of the stress and strain rate under T=45 °C for Full Growth composite configuration. The initial stresses were taken as 15-60 % of the ultimate tensile strength at T=45 °C for the Full Growth composite configuration.

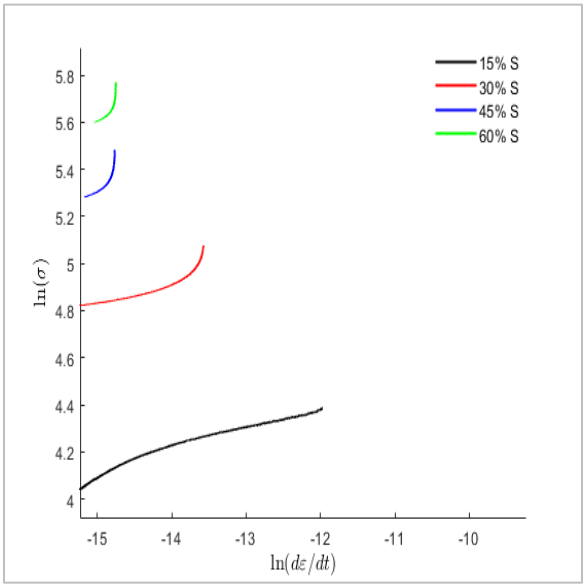

Figure 0.7 Logarithmic plot of the stress and strain rate under T=55 °C for Full Growth composite configuration. The initial stresses were taken as 15-60 % of the ultimate tensile strength at T=55 °C for the Full Growth composite configuration.

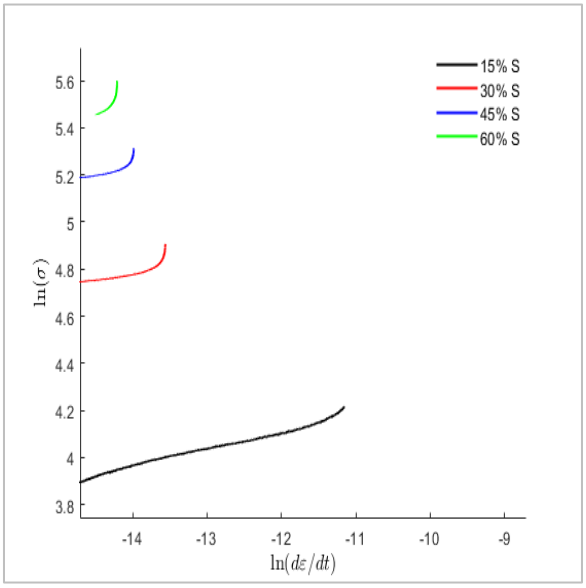

Figure 0.8 Logarithmic plot of the stress and strain rate under T=75 °C for Full Growth composite configuration. The initial stresses were taken as 15-60 % of the ultimate tensile strength at T=75 °C for the Full Growth composite configuration.

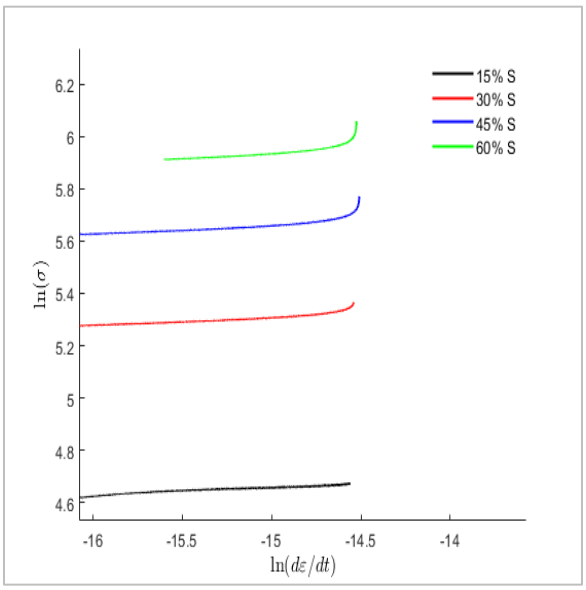

Figure 0.9 Logarithmic plot of the stress and strain rate under T=25 °C for 53 µm patterned composite configuration. The initial stresses were taken as 15-60 % of the ultimate tensile strength at T=25 °C for the 53 µm patterned composite configuration.

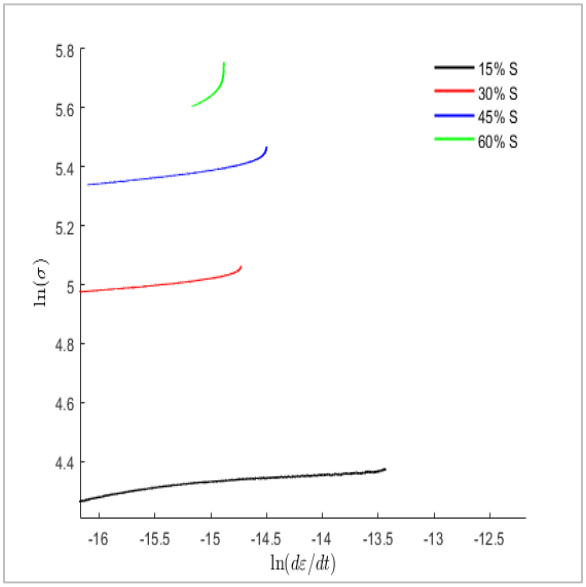

Figure 0.10 Logarithmic plot of the stress and strain rate under T=45 °C for 53 µm patterned composite configuration. The initial stresses were taken as 15-60 % of the ultimate tensile strength at T=45 °C for the 53 µm patterned composite configuration.

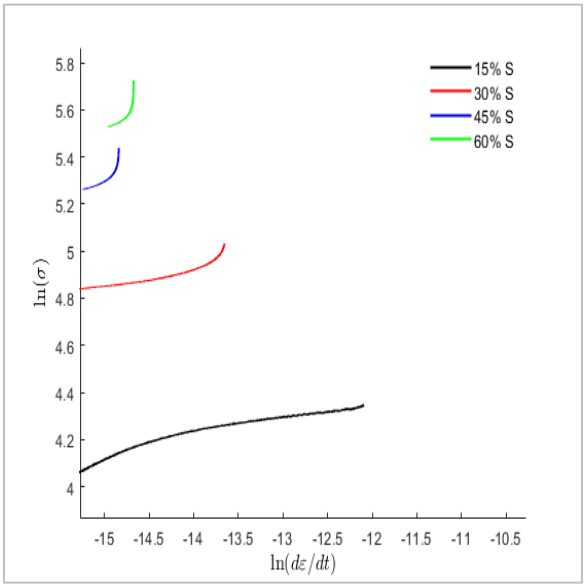

Figure 0.11 Logarithmic plot of the stress and strain rate under T=55 °C for 53 µm patterned composite configuration. The initial stresses were taken as 15-60 % of the ultimate tensile strength at T=55 °C for the 53 µm patterned composite configuration.

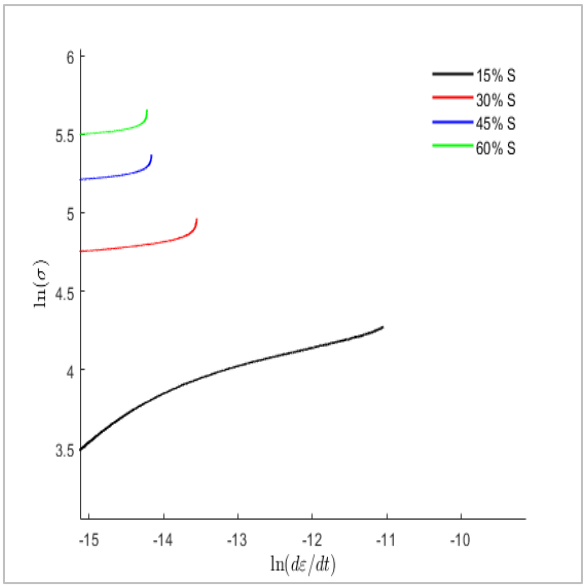

Figure 0.12 Logarithmic plot of the stress and strain rate under T=75 °C for 53 µm patterned composite configuration. The initial stresses were taken as 15-60 % of the ultimate tensile strength at T=75 °C for the 53 µm patterned composite configuration.

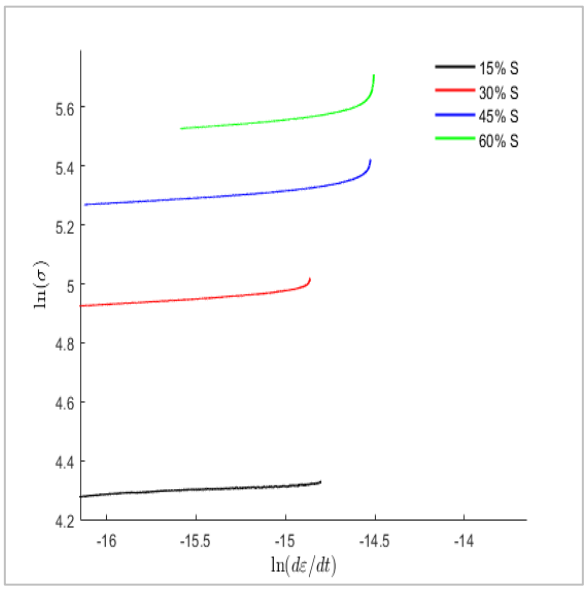

Figure 0.13 Logarithmic plot of the stress and strain rate under T=25 °C for 105 µm patterned composite configuration. The initial stresses were taken as 15-60 % of the ultimate tensile strength at T=25 °C for the 105 µm patterned composite configuration.

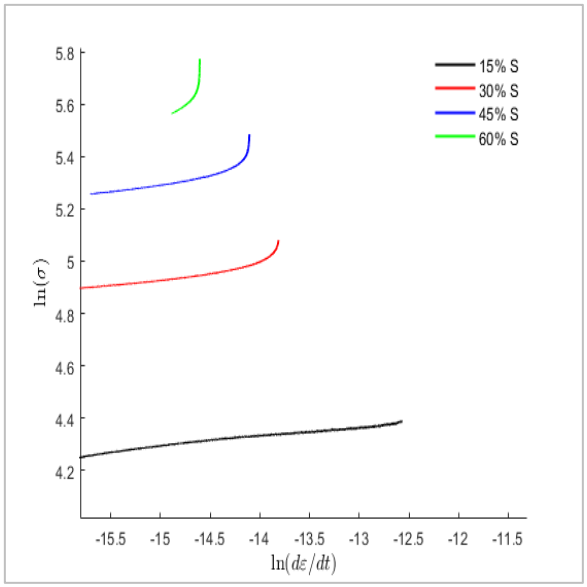

Figure 0.14 Logarithmic plot of the stress and strain rate under T=45 °C for 105 µm patterned composite configuration. The initial stresses were taken as 15-60 % of the ultimate tensile strength at T=45 °C for the 105 µm patterned composite configuration.

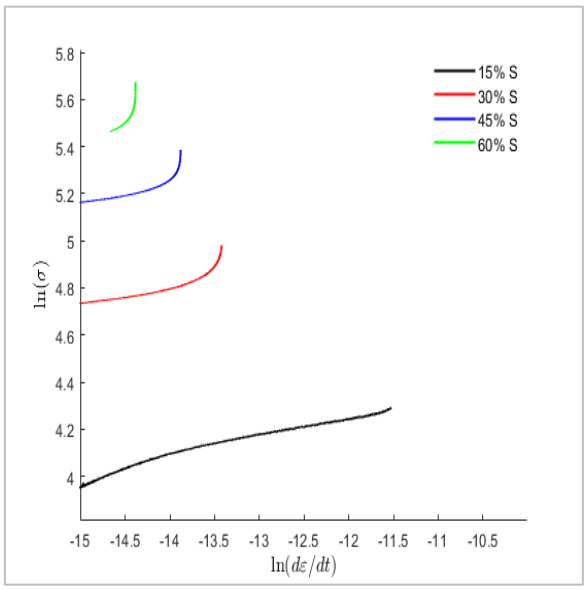

Figure 0.15 Logarithmic plot of the stress and strain rate under T=55 °C for 105 µm patterned composite configuration. The initial stresses were taken as 15-60 % of the ultimate tensile strength at T=55 °C for the 105 µm patterned composite configuration.

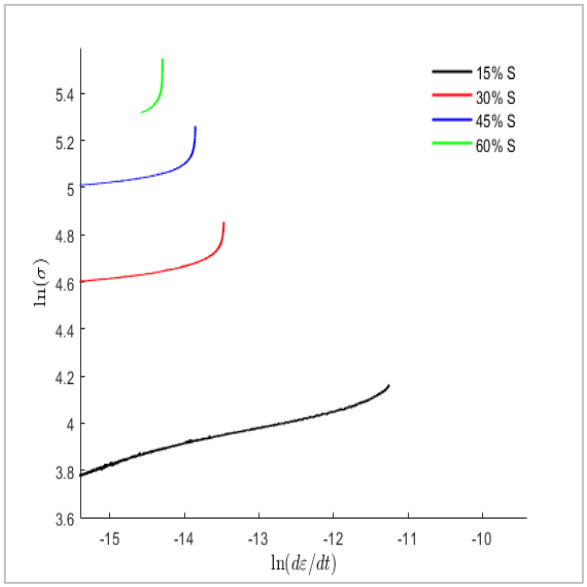

Figure 0.16 Logarithmic plot of the stress and strain rate under T=75 °C for 105 µm patterned composite configuration. The initial stresses were taken as 15-60 % of the ultimate tensile strength at T=75 °C for the 105 µm patterned composite configuration.